

**A MEGA-HERTZ MICRO CONVERTER WITH EXTENDED SOFT SWITCHING
OPERATION FOR PHOTOVOLTAIC (PV) APPLICATION**

SAMIRA AHMADIANKALATI

A THESIS SUBMITTED TO THE FACULTY OF GRADUATE STUDIES

IN PARTIAL FULFILLMENT OF THE REQUIREMENTS

FOR THE DEGREE OF

MASTERS OF APPLIED SCIENCE

GRADUATE PROGRAM IN ELECTRICAL ENGINEERING AND COMPUTER

ENGINEERING

YORK UNIVERSITY

TORONTO, ONTARIO

MAY 2020

© SAMIRA AHMADIANKALATI, 2020

ABSTRACT

The increasing greenhouse effect and relative environmental pollution, along with limited fossil fuel has made it urgent to a transition towards renewable energy sources. The combined global capacity of Photovoltaic (PV) energy has increased considerably from 6.01 gigawatts (GW) to 505 GW from 2006 to 2018. A typical power configuration of a PV energy conversion system consists of a front-end DC/DC micro converter that is used to provide maximum power point tracking (MPPT), as well as to provide some step-up voltage conversion from the output of the PV solar panel. Different DC/DC PV power converters have been reported in literature. The existing DC/DC converters either require a high number of switches and magnetic components, suffer from high voltage stress over some circuit elements, or have low circuit efficiency and restricted switching frequency due to hard switching (hence large size passive components are required).

In this thesis, a very high frequency DC/DC micro converter with inherent extended soft-switching operation is proposed for PV energy conversion systems. In the proposed topology, a boost-based MPPT circuit is integrated with a CL (capacitor-inductor) parallel resonant converter to form a single stage DC/DC PV micro converter. While the proposed converter has an auxiliary circuit to assist extended soft- switching operation, the inductor in the auxiliary circuit is coupled with the boost inductor so that the size and space of the overall circuit can be further reduced. A modified enhanced maximum power point tracking algorithm is also developed to work with the proposed step-up DC/DC micro converter. The theoretical analysis and the operating principles of the proposed converter will be discussed in this thesis. Simulation and experimental results on a MHz (Mega-Hertz) proof-of-concept hardware prototype are provided to highlight the performance of the proposed circuit.

ACKNOWLEDGEMENT

I would like to express my special thanks of gratitude and respect to my supervisor, Dr. John Lam who gave me the opportunity to pursue research studies under his guidance. His invaluable continuous support, encouragement and technical insights has greatly helped me in completion of my thesis. I appreciate all the time and ideas he contributed to assist me overcome challenges I had encountered.

I would also like to thank graduate student members of York University's advanced power electronics laboratory for sustainable energy research (PELSER) for their assistance throughout the last two years. In particular, I would like to thank Mehdi Abbasi who took time out of his busy schedules to assist with my research.

TABLE OF CONTENTS

ABSTRACT	ii
ACKNOWLEDGEMENT	iii
TABLE OF CONTENTS	iv
LIST OF TABLES	vi
LIST OF FIGURES	vii
NOMENCLATURE	xi
1. Introduction	1
1.1 PV Energy Systems	1
1.2 Power Conversion in PV Energy System.....	4
1.3 Power Loss in Converters	6
1.4 Existing Power Electronic Converters for PV Energy Systems	8
1.4.1 Standard DC/DC Converter	9
1.4.2 Resonant Converters	13
1.4.3 Step- Up Converters Reported in Literature	18
1.5 Review on Maximum Power Point Tracking Techniques for PV Applications	26
1.5.1 Perturb and Observe	27
1.5.2 Incremental Conductance	28
1.5.3 Fuzzy Logic	29
1.6 Electrolytic and Film Capacitors	31
1.7 Research Motivation	33
1.8 Thesis Contributions	33
1.9 Thesis Outline.....	34
2. Proposed Soft Switched DC/DC PV Micro Converter	36
2.1 Description of the Proposed PV Micro Converter.....	36
2.2 Operating Principles of The Proposed Micro Converter.....	39

2.3 Theoretical Analysis of the Proposed Micro Converter.....	44
2.3.1 Proposed Micro Converter Voltage Gain	46
2.3.1.1 Voltage Gain vs Frequency.....	49
2.3.2 Extended Soft- Switching Operation.....	50
2.4 Derivation of Other Types of the Proposed DC/DC Micro Converter Topologies	56
2.5 Summary	58
3. MPPT Control Scheme for Proposed Micro Converter.....	59
3.1 Theory of the Modified P&O MPPT Algorithm	59
3.2 Control Logic of the Modified MPPT Scheme.....	63
3.3 Summary	68
4. Design and Performance of the Proposed Micro Converter.....	69
4.1 Introduction	69
4.2 Design Specifications in Powerism	69
4.2.1 Results: Micro Converter, MPPT Controller Excluded.....	78
4.2.2 Results: Micro Converter, MPPT Operation	87
4.3 Hardware Experiment Testing.....	91
4.4 Analysis.....	98
4.5 Summary	100
5. Summary and Conclusion	102
5.1 Summary	102
5.2 Contributions	103
5.3 Future work	104
5.4 Conclusions	105
6. Bibliography	106
APPENDIX.....	117

LIST OF TABLES

Table 1-1. Fuzzy Logic Control rules base [54]

Table 1-2: Examples of electrolytic capacitors and their characteristics

Table 1-3: Examples of film capacitors and their characteristics

Table 2-1: Components used in the proposed quasi-resonant step-up converter

Table 3-1: MPP tracking scenarios for the modified P&O method

Table 4-1: Component values

Table 4-2: Non-ideal parameters

Table 4-3: Solar panel parameters

Table 4-4: Circuit Component parameters soldered on the PCB of the proposed micro converter

Table 4-5: Comparison of various step-up DC/DC Converters for PV energy applications

LIST OF FIGURES

- Figure 1-1: Total CO₂ emissions per country from 2015 [1, 3]
- Figure 1-2: Annual additions of Renewable Power Capacity, by Technology and total, in 2018
- Figure 1-3: Growth rate of renewable energy capacity [5]
- Figure 1-4: Common PV system configurations
- Figure 1-5: Example of switching power loss (hard switching)
- Figure 1-6: Conventional DC/DC converters: (a) buck, (b) boost, (c) buck boost
- Figure 1-7: Converter Gain as a function of Duty Cycle
- Figure 1-8: Diagram of a Resonant Converter Block
- Figure 1-9: Diagram of a Half Bridge Inverter Block
- Figure 1-10: Output Voltage Waveform of HB Inverter
- Figure 1-11: Diagram of a Full Bridge Inverter Block
- Figure 1-12: Output Voltage waveform of FB Inverter
- Figure 1-13: Diagram of an APWM Inverter Block
- Figure 1-14: Output Voltage waveforms of APWM inverter at input voltage V_i
- Figure 1-15: Circuit diagram of APWM Series Resonant Converter
- Figure 1-16: Circuit diagram of APWM Parallel Resonant Converter
- Figure 1-17: Circuit diagram of APWM Series- Parallel Resonant Converter
- Figure 1-18: Conventional interleaved boost converter
- Figure 1-19: Conventional three level boost converter
- Figure 1-20: (a) Cascade boost converter (b) Integrated cascade boost converter
- Figure 1-21: Hybrid boost-flyback converter with a coupled inductor boost converter

Figure 1-22: High step up single switch converter

Figure 1-23: Interleaved boost converter with an auxiliary transformer

Figure 1-24: Half-bridge soft- switching LLC micro converter introduced in [40]

Figure 1-25: Schematic of 1- MHz LLC series resonant converter introduced in [41]

Figure 1-26: Power- Voltage curve of a solar panel at various light intensities: $D > C > B > A$

Figure 1-27: A PV Panel connected to power electronic converter with integrated MPPT controller

Figure 1-28: Maximum power point tracking using conventional perturb and observe: (a) Light intensity increased, (b) moving towards high light intensity MPP operation

Figure 2-1: Derivation of the proposed DC/DC converter

Figure 2-2: Theoretical operating waveforms of the proposed converter

Figure 2-3: Micro converter Operating stage

Figure 2-4: Equivalent Circuit of the resonant tank in the proposed micro converter

Figure 2-5: (a) Proposed Micro converter voltage gain (valid at $D= 0.7$) (b) The APWM resonant circuit gain at various quality factor values

Figure 2-6: Current through S_2 at turn off, I_2 , as a function of d in the proposed micro converter

Figure 2-7: Current through switch S_1 at turn- off, I_1 as a function of d in the proposed micro converter

Figure 2-8: Current through switch S_1 at turn- off, I_1 as a function of d in a same topology without auxiliary circuit

Figure 2-9: Circuit diagram of the proposed micro converter: non- isolated topology

Figure 2-10: Circuit diagram of the proposed micro converter: non-isolated topology with voltage- doubler

Figure 2-11: Circuit diagram of the proposed micro converter: isolated topology with voltage-doubler

Figure 3-1: Maximum Power Point Tracking Process of the presented Micro converter

Figure 3-2: Modified Perturb and Observe maximum power point tracking controller implemented with the proposed converter

Figure 4-1: PSIM Solar Module (physical model)

Figure 4-2: PSIM waveforms of the proposed micro converter at light intensity of 600 W/m^2 with a switching frequency of 1.35 MHz and a duty ratio of 0.75 (a) input and output voltage of the micro converter along with output voltage of the integrated boost converter (b) Input and output power of the proposed micro converter (c) Boost inductor voltage and current (d) Auxiliary inductor voltage and current (e) Switch 1 voltage and current (f) Switch 2 voltage and current waveforms

Figure 4-3: PSIM waveforms of the proposed micro converter at light intensity of 800 W/m^2 with a switching frequency of 1.35 MHz and a duty ratio of 0.83 (a) input and output voltage of the micro converter along with output voltage of the integrated boost converter (b) Input and output power of the proposed micro converter (c) Boost inductor voltage and current waveforms (d) Auxiliary inductor voltage and current waveforms (e) Switch 1 voltage and current (f) Switch 2 voltage and current waveforms

Figure 4-4: (a) Light intensity of the solar panel in PSIM (b) Actual input power of the solar panel in compared to the reference maximum power

Figure 4-5: (a) Switch 1 voltage waveform at various light intensities (b) Switch 1 current

Figure 4-6: (a) Switch 2 voltage waveform at various light intensities (b) Switch 2 current waveform (c), (d) Enlarged voltage and current waveform at the selected time intervals

Figure 4-7: Micro converter gate driver application diagram obtained from LM5113-Q1 datasheet

Figure 4-8: Micro converter switch gate signal when the logic unit is powered at 1.01 MHz frequency

Figure 4-9: Switch S_2 waveforms and boost inductor current

Figure 4-10: Resonant Inductor and load voltage waveform and circuit Switches current waveforms

Figure 4-11: Voltage waveform of boost converter capacitor C_1 and switch current waveforms

NOMENCLATURE

<i>PV</i>	Photovoltaic
<i>MPP</i>	Maximum Power Point
<i>DC</i>	Direct Current
<i>GW</i>	Gigawatt
<i>MW</i>	Megawatt
<i>AC</i>	Alternating Current
<i>MPPT</i>	Maximum Power Point Tracking
<i>MOSFET</i>	Metal-oxide semiconductor field effect transistor
<i>ZVS</i>	Zero Voltage Switching
<i>ZCS</i>	Zero Current Switching
<i>P_D</i>	Dissipated Power
<i>RMS</i>	Root Mean Square
<i>FB</i>	Full Bridge
<i>HB</i>	Half Bridge
<i>APWM</i>	Asymmetrical Pulse Width Modulated
<i>IC</i>	Incremental Conductance
<i>FLC</i>	Fuzzy Logic Control
<i>CE</i>	Change of Error
<i>ZE</i>	Zero
<i>PB</i>	Positive Big
<i>NB</i>	Negative Big
<i>NS</i>	Negative Small
<i>PS</i>	Positive Small
<i>C_s</i>	Resonant capacitor

C_{in}	Input Capacitor
C_1	Boost circuit capacitor
C_2	Boost circuit capacitor
L_{in}	Resonant circuit inductor
L_m	Boost circuit input inductor
L_a	Auxiliary Circuit inductor
S	Switch
T	High frequency transformer
DR	Rectifying Diode
L_o	Output Inductor
C_o	Output Capacitor
KCL	Kirchoff's Current Law
KVL	Kirchoff's Voltage Law
ω_o	Switching Frequency
ω	Relative Operating Frequency
ω_r	Resonant Frequency
Q	Quality Factor
i_{La}	Auxiliary inductor current
V_{La}	Auxiliary inductor voltage
i_{res}	Resonant circuit current
D	Duty cycle
V_{inres}	Integrated boost converter output voltage
T_s	Switching period
R_{ac}	Equivalent load resistance
V_{in}	Input Voltage of the micro converter

V_o	Output Voltage of the micro converter
PCB	Printed Circuit Board
$PSIM$	Power Sim
R_L	Output Resistance
$MPPT$	Maximum Power Point Tracking
DSP	Digital Signal Processing
CCM	Continuous Conduction Mode
DCM	Discontinuous Conduction Mode
V_{lm}	Voltage across resonant inductor
MHz	Mega-Hertz

1. Introduction

1.1 PV Energy Systems

Currently, the total non-renewable energy share of global electricity production is just above 73.8% [1]. The use of fossil fuels has several drawbacks. Due to its massive contribution to the emission of greenhouse gases such as carbon dioxide CO₂ and methane, fossil energy sources are a major factor to increase global pollution. In 2018, the emissions of global warming CO₂ increased by 2.7% to record levels of global carbon budget [2], climbing to a record of 37.1 giga tones [3]. Fig. 1-1 shows the breakdown of total CO₂ emission per country [4]. In addition, the residue of fossil energy resources is critically limited and would be exhausted in near future. It is predicted

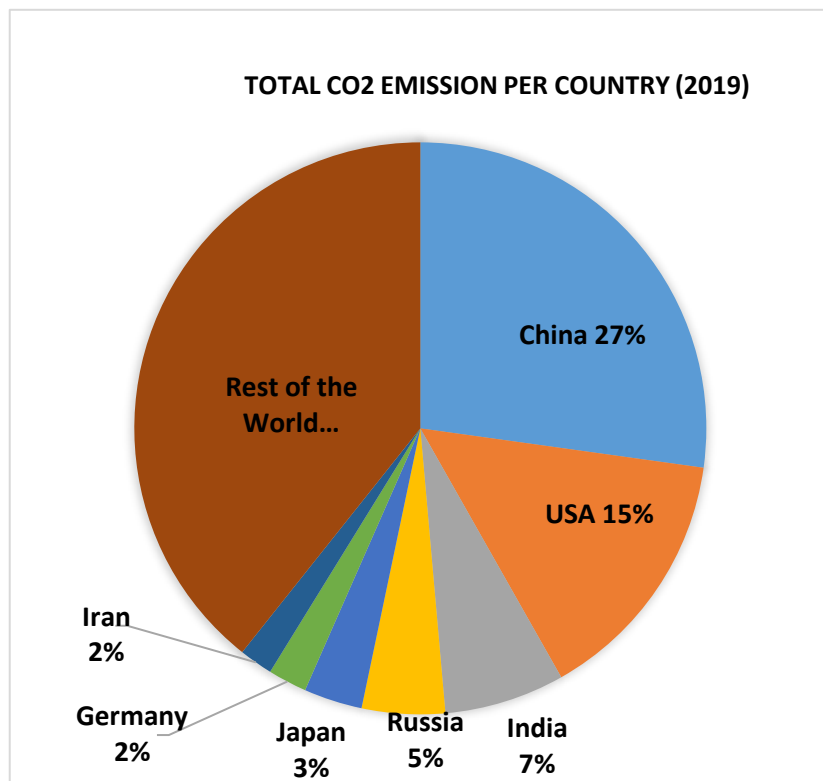


Fig. 1-1: Total CO₂ emissions per country from 2015 [1, 3]

that supplies will be thoroughly consumed by the year 2088 [5]. Hence, smooth transition towards the use of renewable energy has become a research of great urgency.

Renewable energy is energy that is obtained at a rate that is equal or faster than the rate at which it is consumed, including energy generated from a source that is inexhaustible. These include sources such as solar, wind, geothermal, and hydro-power. These sources are infinite in use, however, the amount of energy that can be obtained is usually limited per unit of time. For example, solar energy can only be obtained while sunlight is present and wind energy can only be obtained when wind is present.

Among all renewable energy sources, PV energy makes one of the largest contributions to global electricity generation which makes it significant player in the world’s energy portfolio. This is because of its simplicity, advancement in their field and its high reliability. Fig. 1-2 illustrates the growth rate of various renewable energy systems in 2018 with a total of 181 Gigawatts (GW).

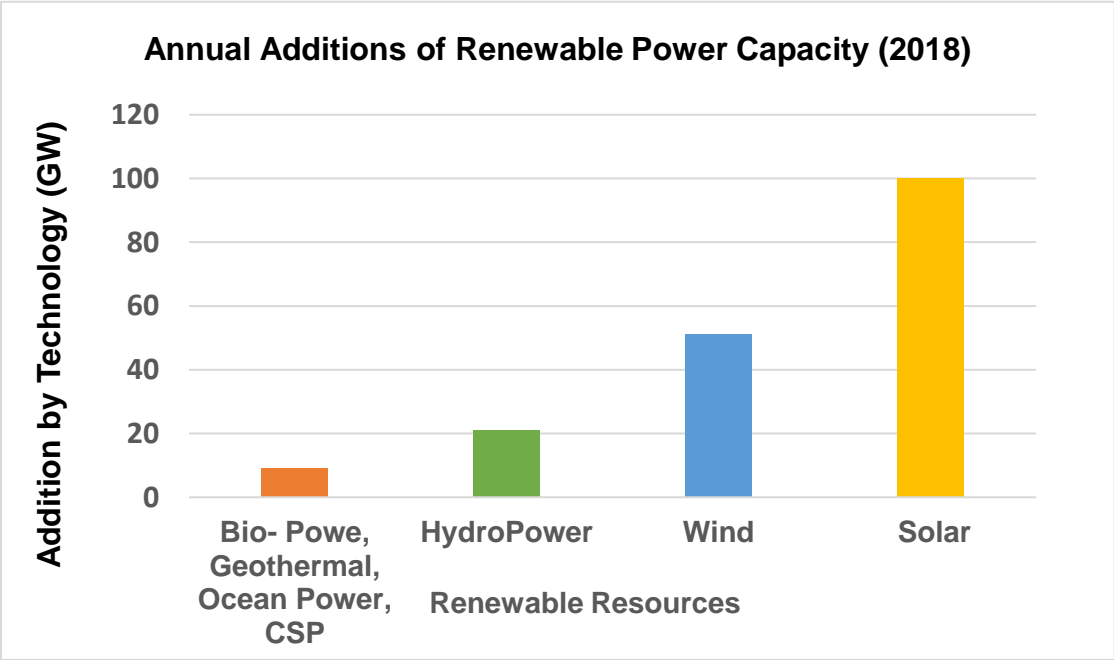


Fig. 1-2: Annual additions of Renewable Power Capacity, by Technology and total, in 2018

With 100 GW added, PV energy was the frontrunner and it is accounted for 55% of total addition renewable energy capacity. This is followed by wind with 28% and hydropower with 11% [1]. Fig. 1-3 gives the total PV capacity and the annual additions from 2008 to 2018. The combined global capacity of PV energy has increased considerably from 2008 to 2018, with 6.01 GW to above 505 GW respectively. It can be seen that the PV energy had the highest growth rate which increased by over 33%. The total global capacity of PV energy has increased from 6.01GW to 402GW from 2006 to 2017 [5] and is predicted to have increased by an additional 575GW by 2023 [6].

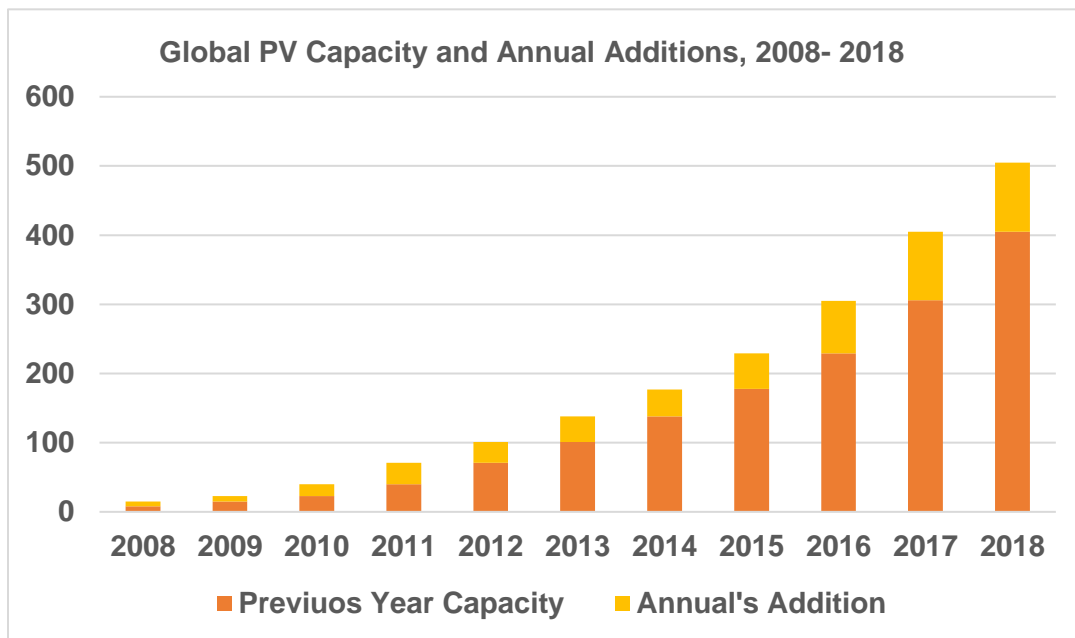


Fig. 1-3: Growth rate of renewable energy capacity [5]

Canada has a high share of renewable in energy supply at about 17.3%. A large portion of this energy is provided through hydro- power; however, the solar generation is on the rise. The cumulative installed capacity of PV energy in Canada has increased from 16.7 MW to above 3040 MW from 2005 to 2018 [7]. It is estimated that 320 tons of CO₂ can be avoided each hour through the use of solar PV energy in Ontario and this is projected to increase in future [8].

1.2 Power Conversion in PV Energy System

The captured energy of PV solar panel cannot be used instantly by the load and it needs to be converted into desired electrical energy. This is achieved by connecting power electronic converters to the PV panels. These converters transform electrical energy which is then transferred to the load or directly connected to the grid. The output voltage of a typical PV panel is relatively low; ranging from 12V to 40V, while the typical grid voltage level is 380 V. [10-12] Power electronic converter is therefore utilized to step-up the voltage such that it matches the grid requirements. A power electronic converter consists of active components such as switches and diodes and passive components such as inductors and capacitors. Different configurations of these components allow for the assembly of circuits that could carry out the required performance. High power efficiency, low components count, compact circuit and light-weight system are key criteria in the design of power electronic converters.

PV panels are arranged in several configurations which affect the topology of their electronic device. The device usually consists of DC/DC converter and if the system is connected to the grid, then a DC/AC converter is also required. The most common configurations of PV system are mainly centralized, string, multistring and AC module. Fig. 1-4 shows the schematic representation of these configurations [9].

Centralized configuration is illustrated in Fig 1-4 (a). This configuration is suitable for PV systems with a nominal peak power higher than 10 kW, where PV panels are all connected in series- parallel configuration. The strings have blocking diodes that prevents the revision of energy.

If each string in centralized configuration owns a separate DC/AC converter, then this is a string configuration shown in Fig 1-4 (b).

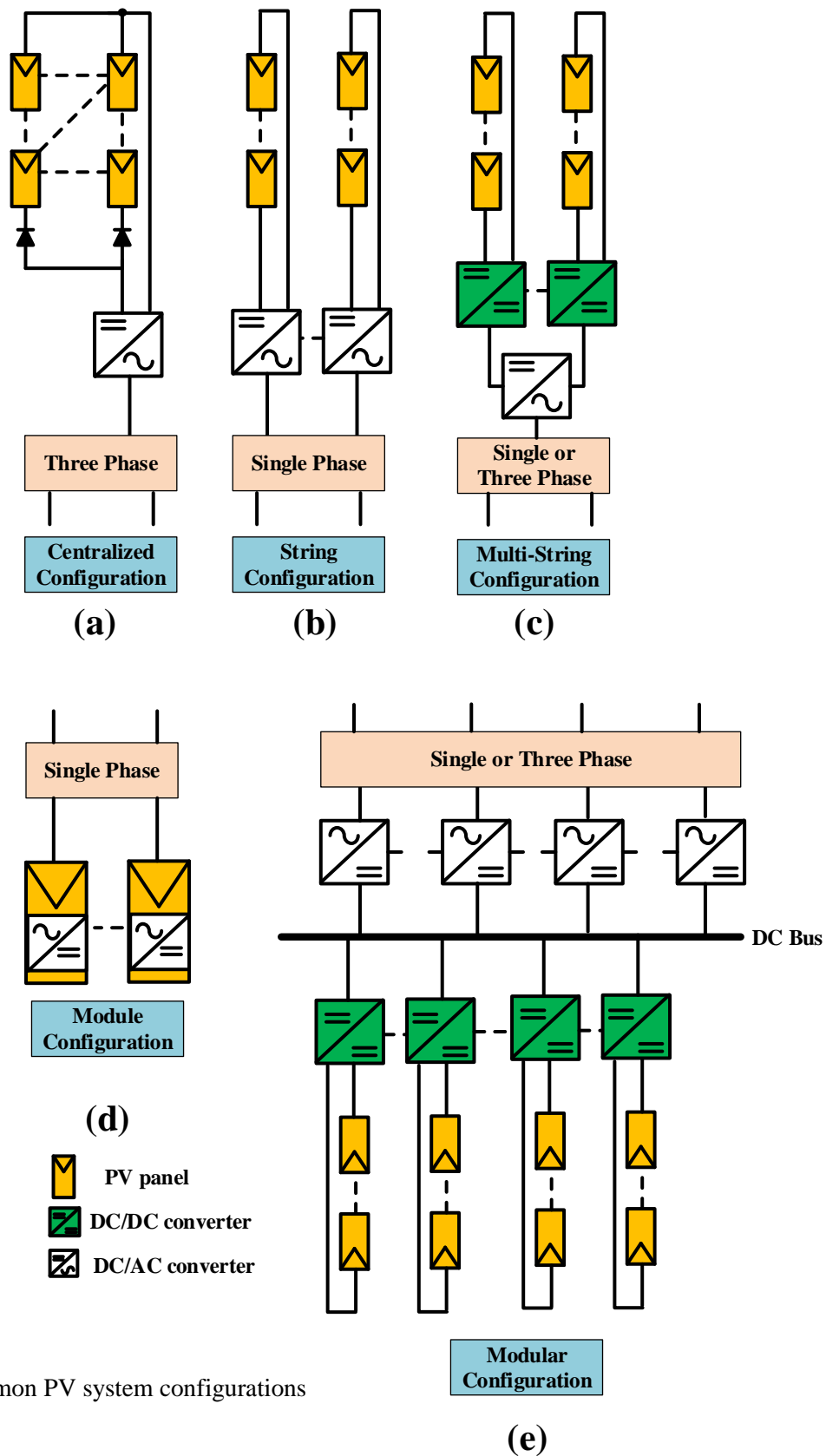


Fig. 1-4: Common PV system configurations

Multistring configuration is shown in Fig 1-4 (c). This configuration is an evolved version of string configuration that combines the advantages of both string and centralized configurations. The maximum power point tracking (which will be discussed thoroughly in section 1.6) is implemented in each string which makes the system more flexible with higher efficiency. AC module is a configuration in which each PV module has its own dedicated DC/AC converter that performs MPPT control at each module level. This configuration operates automatically like a plug-play system. It is associated with higher costs and it is difficult to implement. This configuration is given in Fig 4-1 (d)

Modular configuration is illustrated in Fig 1-4 (e) [12]. In this configuration each string is connected to a DC/DC converter which performs the MPPT control algorithm. A DC bus is shared between all DC/DC and DC/AC converters. The system enjoys a higher reliability and easier to maintain as in damage case, only the defected converter needs to be replaced.

1.3 Power Loss in Converters

As briefly discussed in section 1.2, power electronic converters are utilized to step up panel output voltage such that it matches the grid standards. Converters do not achieve 100% efficiency as there are two major types of power loss associated to power conversion process. Key power-loss contributors in a converter includes: Switching loss [14] and conduction loss [15].

Semiconductor field effect transistors (MOSFET) have a finite switching time. Fig. 1-5 depicts an example of switching power loss. In this figure switch voltage (v_s) and switch current (i_s) are shown as a function of time. Switching power loss occurs when a MOSFET is alternated from either on-state to off-state or vice versa. The overlap interval existed in the switch voltage and switch current results in power dissipation. This scenario is refereed as hard- switching [14] According to Fig. 1-

5, the amount of energy dissipated in the switch during its turn- on and turn- off interval can be calculated as

$$W_{c(off)} = 0.5V_d t_{c(off)} I_0 \quad (1-1)$$

$$W_{c(on)} = 0.5V_d t_{c(on)} I_0 \quad (1-2)$$

The instantaneous power loss $P_{T(t)}$ is plotted in Fig. 1-5 (c). From that, it can be clearly seen that a large power dissipation occurs in the switch operation during turn-on and turn- off intervals.

Average switching power loss P_{loss} in the switch due to the transitions is a function of the switch voltage, switch current, operating frequency and the overlap time $t_{c(off)}$ or $t_{c(on)}$ and is given by

$$P_{loss} = 0.5V_d I_0 f_s (t_1 - t_0) \quad (1-3)$$

$$P_{loss} = (E_{on} - E_{off}) f_s \quad (1-4)$$

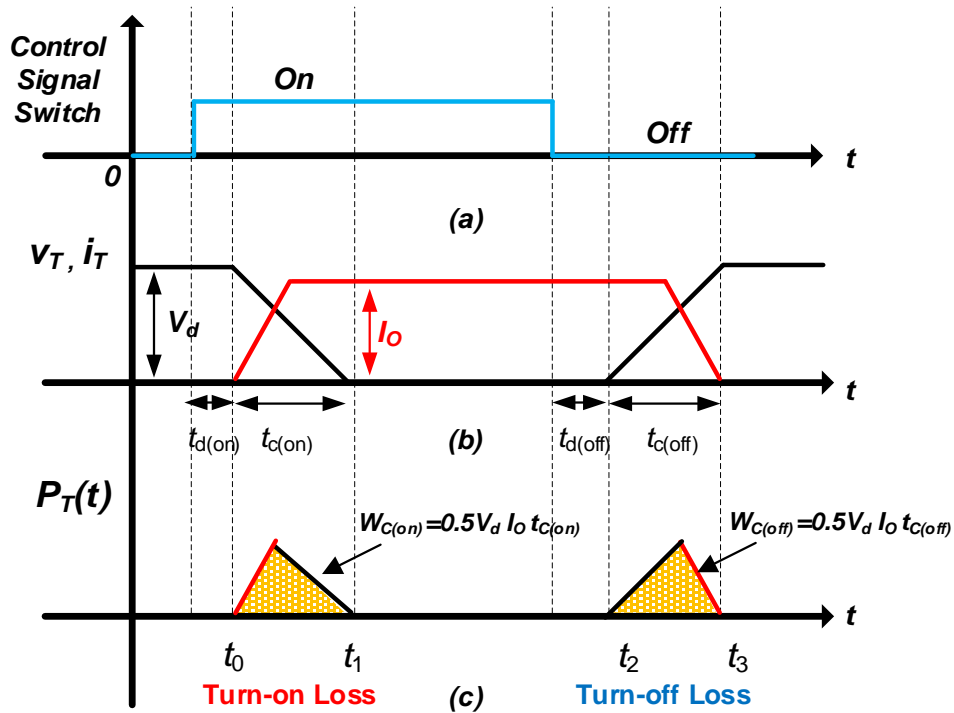


Fig. 1-5: Example of switching power loss (hard switching)

To decrease power loss due to hard switching, a technique known as soft-switching is utilized. Soft switching is a method to minimize the overlap interval in switch current and voltage waveforms. The two techniques that assist the power circuit to achieve soft-switching are: zero voltage switching (ZVS) and zero current switching (ZCS). Both techniques can be achieved by utilizing additional small-size inductors and capacitors in the power circuit. Various resonant circuits have been reported in literature to help achieving soft-switching operation.

When gate signal is applied, current flows through the switch. As switch is not ideal, a relatively low resistance appears over drain and source of the switch known as on-resistance $R_{ds(on)}$. This parameter varies depending on type of the switch (MOSFET, GaN) or ratings of the switch being used. As given in (1-5), power loss of the switch is also a function of $R_{ds(on)}$. This resistance is a major contributor of the dissipated power of the circuit. In (1-5) P_D represents power loss across the switch and I_s represents the switch current Root Mean Square (RMS) value. This type of loss is referred as conduction loss. [15]. Conduction loss of the switch is a value proportional to both ON resistance value and switch current RMS value during its on-state interval.

$$P_D = I_s^2 \times R_{ds(on)} \quad (1-5)$$

1.4 Existing Power Electronic Converters for PV Energy Systems

DC/DC converters are widely used to regulate output voltage of PV panels such that it matches the grid. Performance improvement, high efficiency and cost minimization are the key concerns in existing power electronic converters. To date, several standard power electronic converters are designed that are capable of increasing and/or decreasing the input voltage. Depending on the application, many alternative converters have been reported in literature as follow:

1. Step- Up (Boost) Converter

2. Step Down (Buck) Converter
3. Step Down/ Step Up (Buck- Boost) Converter
4. Full Bridge Converter
5. Resonant Converter

Of these five converters, boost, buck and buck- boost and resonant converters are the basic converter topologies. Full bridge converter is derived from step- down converter. In the rest of this section, first in 1.4.1, conventional converters including buck, boost and boost- buck type are explained. Then in 1.4.2 an introduction of basic resonant converter is provided. Lastly, in section 1.4.3 some other existing converters reported in literature is discussed.

1.4.1 Standard DC/DC Converter

Buck converter or step- down converter is shown in Fig. 1-6 (a). As the name is explanatory, buck converter produces a lower average output voltage than the input voltage of the converter. This converter consists of a capacitor, an inductor, diode and a single switch. When the switch is turned on, the diode becomes reversed biased. During this time the input provides energy to the load and the inductor; therefore, the inductor stores energy. When the switch is off, the inductor connects directly to the ground, energy stored in the inductor flows through the diode and will be transferred to the load. The gain of the converter is related to the fraction of switching period time at which the switch is on. This time is referred to as duty ratio D of the converter that has a value between 0 and 1.

Buck converter gain can be calculated in terms of the switch duty cycle given in Eq. 1-6 and it is equal to duty ratio. Consequently, the higher the duty cycle the higher the gain. It is also understood that the gain ranges from 0 to 1 so this converter cannot step up the voltage. Buck converters main

applications are DC power supply regulation, battery chargers and control of motor speed battery chargers [16].

(1-6)

$$\frac{v_o}{v_i} = D$$

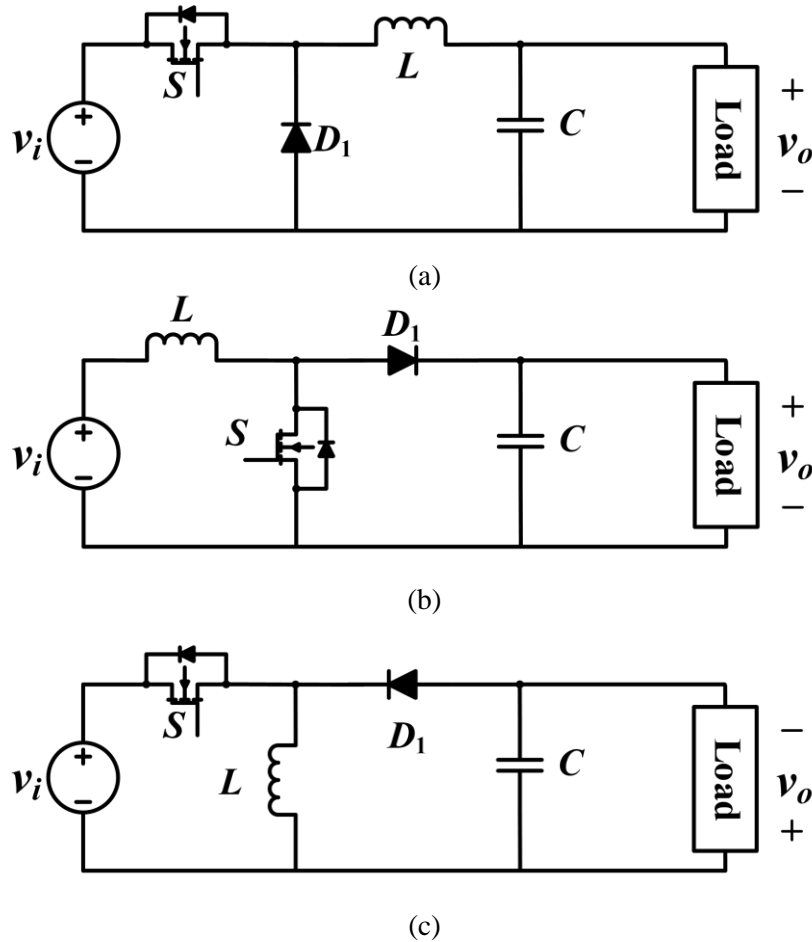


Fig. 1-6: Conventional DC/DC converters: (a) buck, (b) boost, (c) buck boost

Boost converter circuit topology is shown in Fig. 6(b). Similar to buck converter, Conventional boost converter also consists of an inductor, capacitor, diode and a switch but it has different component arrangement. As the name implies, boost converter is capable of increasing voltage level such that the output voltage is always greater than the input voltage. When the switch is on,

the diode is reversed biased so the output stage is isolated. In this period input provides energy to the inductor. When the switch turns off, output load receives energy both from the inductor and the input. Therefore, this inductor is charged when the switch is on and it gets discharged when the switch is off. The capacitor is assumed to be very large such that the output voltage becomes constant. The gain of boost converter is provided in equation 1-7. And it is once again proportional to duty cycle. As the duty cycle increases from 0 to 1, The gain increases from 1 to positive infinity. Therefore, the gain of boost converter ranges from 1 to positive infinity. The main applications of boost converter are DC power supply regulations and DC motor regenerative braking.

$$\frac{v_o}{v_i} = \frac{1}{1-D} \quad (1-7)$$

Basic Buck- boost converter is illustrated in Fig. 6(c). A buck- boost converter is obtained by the cascade connection of the step-up converter and step-down converter. Based on the switch duty cycle, this converter is able to either increase or decrease the input voltage. The gain of boost-buck converter is the product of both boost converter and buck converter gain. This converter is similar to buck converter in terms of circuit diagram however the place of inductor and diode is swapped. When the switch is closed, the diode is revers biased and the input charges the inductor. When the switch is off, the stored energy in inductor is transferred to the output. During the off-time interval, no energy is supplied by the input. The capacitor is assumed to be very large, resulting in a constant output voltage. Due to this connection when the diode is conducting, the current flows in opposite direction to the load. Thus, the output voltage polarity is reversed as can be seen in fig. 6(c). Equation 1-8 gives the gain of boost- buck converter. When the duty cycle is less than 0.5, the gain is less than 1 so the converter is operating in buck mode. When the duty cycle is greater than 0.5, gain becomes greater than 1 and the converter operates as a boost converter.

$$\frac{v_o}{v_i} = \frac{D}{1-D} \quad (1-8)$$

Gain of conventional boost, buck and boost-buck converter is plotted in Fig 1-7; by red, blue and green respectively. From this graph it can be observed that boost- buck converter has a wider range of gain from 0 to infinity. Boost converter operates with a minimum gain of 1 while buck converter achieves maximum gain equal to 1. Both boost and buck- boost converter can achieve a large gain if their switch operate with high duty ratio value. To step up solar PV panel output voltage from 35V to 380V, in a conventional boost converter, switches has to operate at almost 90% duty cycle. Theoretically, at a duty ratio close to 1, the voltage gain of conventional converters can be infinite. However, when the duty cycle increases, the switch turn-off period becomes very short. This results in large current ripples in the circuit and large turn-off current. Therefore, conduction losses

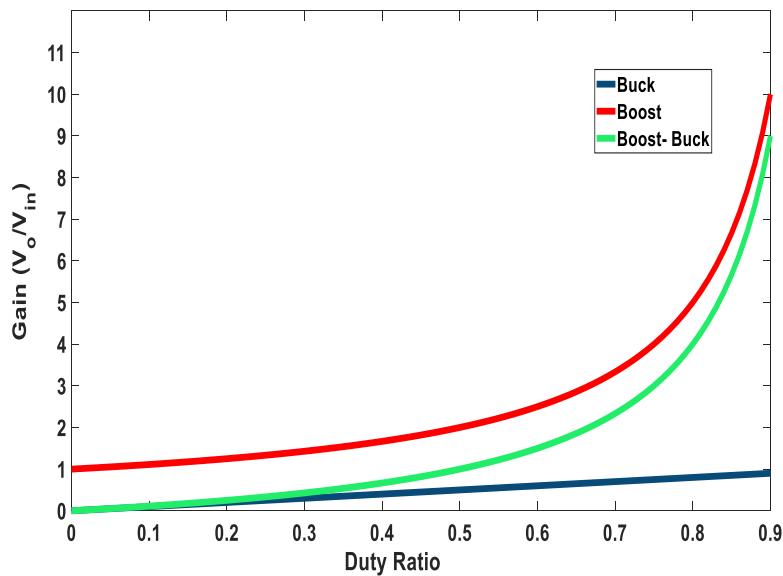


Fig. 1-7: Converter Gian as a function of Duty Cycle

increase considerably. In addition, in high- gain applications, the voltage stress of the switch and diode is equal to the output voltage which is large. Switches with high voltage stress has relatively more cost in compared to switches with lower voltage stress. Furthermore, due to the hard-switching, significant switching and reverse- recovery losses are also associated. [16]

1.4.2 Resonant Converters

Fig. 1-8 shows the general diagram of the whole resonant converter system used in PV applications. As can be observed this diagram consists of an inverter block, Resonant converter block, the rectifier block as well as the filter block. Resonant converters may vary based on several types of blocks implemented so far.

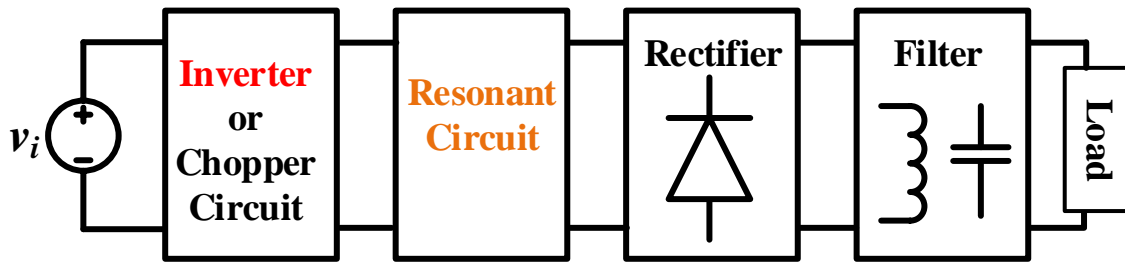


Fig. 1-8: Diagram of a Resonant Converter Block

There are mainly three types of single-phase Inverter blocks: Full Bridge (FB), Half Bridge (HB) and Asymmetrical Pulse Width Modulated (APWM) type. Circuit diagram of HB inverter is given in Fig. 1-9. In this type of inverter two power electronic switches are employed. Input DC voltage V_i applies to the HB inverter block then this source is divided into two equal parts. Both switches

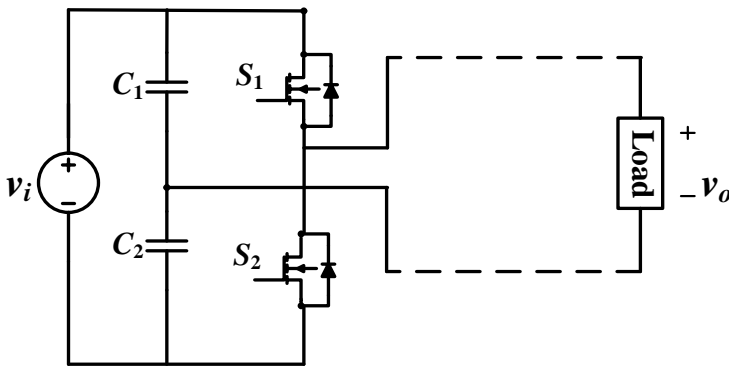


Fig.1-9: Diagram of a Half Bridge Inverter Block

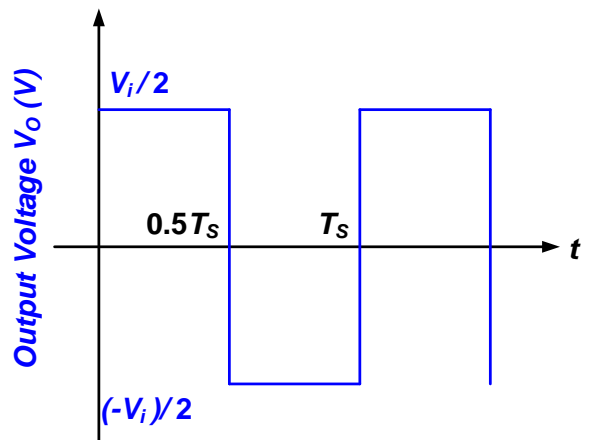


Fig. 1-10: Output Voltage Waveform of HB Inverter

receive gate signals with specific ON time and OFF time. When Switch 1 is triggered for the first half of the cycle, at that time period switch 2 is off. Current flows through switch 1 and the load voltage equals to half of input voltage $V_i/2$. Similarly, when switch 1 is off switch 2 carries the current flow to the load so the load voltage is kept at $V_i/2$ for the total switching period. Fig. 1-10 provides the output voltage waveform of HB inverter with input voltage V_i in a variable frequency control system.

Fig. 1-11 shows FB inverter block. In this type of inverter four power electronic switches are employed. The main difference between FB and HB inverter circuit is that the maximum value of output voltage equals input voltage in FB, while it equals half of the input supply voltage in HB. Gate driver triggers switch 1 and 2 simultaneously when switch 3 and 4 operate together. During ON time for switch 1 and 2, current flows through switches and it gets transferred to the load. Once switch 3 and 4 are triggered, the current flows through these switch paths. In both condition output voltage equals to input voltage. Fig. 1-12 shows the FB inverter output voltage with V_i and a variable frequency control system.

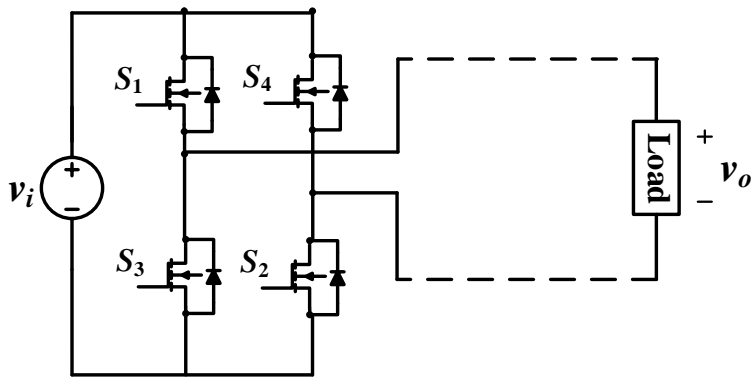


Fig. 1-11: Diagram of a Full Bridge Inverter Block

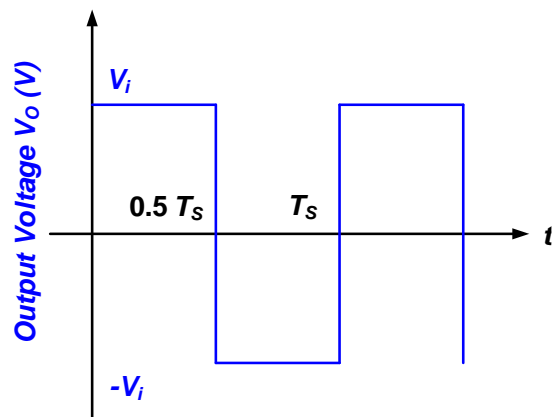


Fig. 1-12: Output Voltage waveform of FB Inverter

Contrary to the basic FB and HB inverters, asymmetrical pulse width modulated inverter drives switches with non-equal duty ratio values. In this inverter topology the switches conduct with duty cycles that are complementary with another. APWM is suitable for near- zero switching losses operation while driving at a very high frequency. Fig. 1-13 illustrates APWM inverter topology. Duty ratio of switches is complementary to another; If switch 1 drives with duty cycle D then switch 2 will receive $1-D$. An example of output voltage waveform is given in Fig. 1-14 for an APWM inverter which is operating at D with a variable frequency control system.

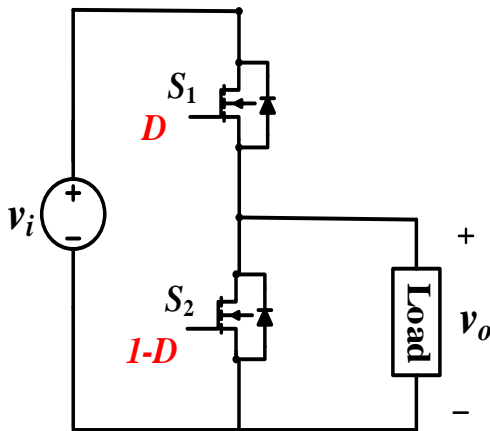


Fig. 1-13: Diagram of an APWM Inverter Block

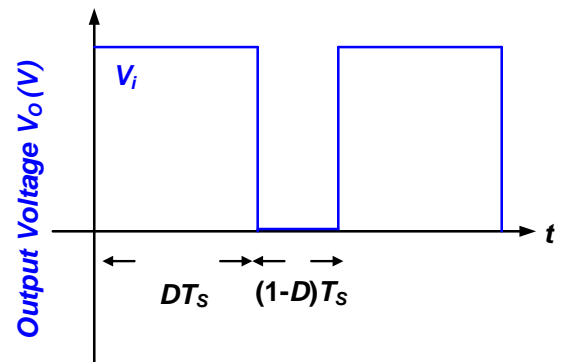


Fig. 1-14: Output Voltage waveforms of APWM inverter at input voltage V_i

To achieve small-size, light-weight power electronic converters, operating frequency is required to be raised such that the size of reactive components decrease. However, according to (1-3), higher switching frequency is associated with higher switching losses. Resonant power converters are receiving a renewed large interest as they can achieve zero current switching (ZCS) and zero voltage switching (ZVS) under a suitable circumstance. In other words, switching losses can be 100% avoided if resonant converters are employed with an appropriate switching frequency. To

obtain a ZVS operation and no loss in turn on interval, switches are required to operate upper than resonant frequency. [17] Lossless turn off switching operation is also obtained by placing lossless snubber capacitors directly across the switch devices. There are three main resonant converters as:

- 1- series- resonant
- 2- Parallel resonant
- 3- series-parallel resonant converters

Fig. 1-15 shows an APWM series- resonant converter diagram [18]. This circuit contains of chopper circuit, series- resonant tank, high frequency transformer and an output filter circuit. The APWM chopper applies a square voltage waveform to the resonant tank. Resonant tank consists of C_s and L_s that are connected in series. The function of C_s is to block the DC component of the output voltage V_s from transferring it to the load. In addition, it builds a resonant tank with inductor L_s . High- frequency transformer is utilized to isolate output stage from the converter. Rectifying stage with diodes DR_1 and DR_2 converts the sinusoidal i_s into a unidirectional output current i_o . Capacitor C_o helps with filtering out the output current ripple and provides a substantially constant output voltage V_o across the load.

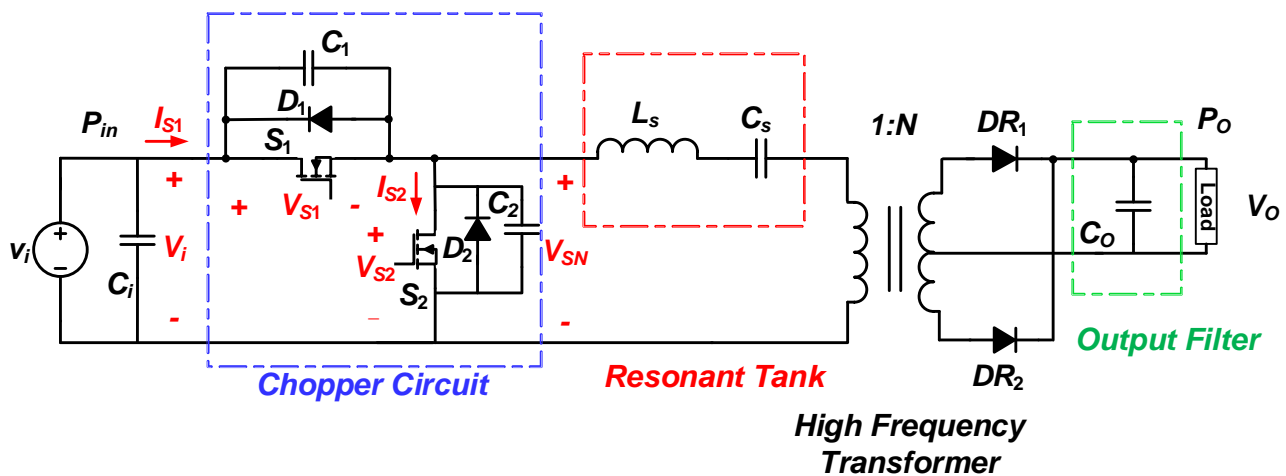


Fig. 1-15: Circuit diagram of APWM Series Resonant Converter

The most important advantage of this circuit is the DC blocking behavior of resonant capacitor. For this reason, this converter is suitable for very high-power applications where a full bridge converter is required. One more advantage to series resonant converters is that as the load decreases, the current in the power devices decreases. This allows to operate with lower conduction losses and higher efficiency when the load decreases. Main disadvantage of series- resonant converter is that it cannot be regulated for the no- load condition. This means that this converter can be used in applications where no- load regulation is not required and the circuit is being used as it is. Second disadvantage is that the output capacitor does carry high ripple current; Thereby this converter is only suitable for high-output-voltage and low-output-current. [18]

Fig. 1-16 illustrates a circuit diagram of parallel resonant converter. [19-20] Similar to series resonant topology, this circuit consists of a chopper circuit, parallel resonant circuit, a high frequency transformer, rectifying stage and the output filter. Contrary to series resonant converter, parallel resonant converter is able to control and regulate output voltage at no load. Main disadvantage of this converter is that the current carried by resonant components is rather independent of the load value. As a consequence, if the load changes the conduction losses of the circuit stays fixed. This results in a very poor efficiency at light load. Furthermore, as the input

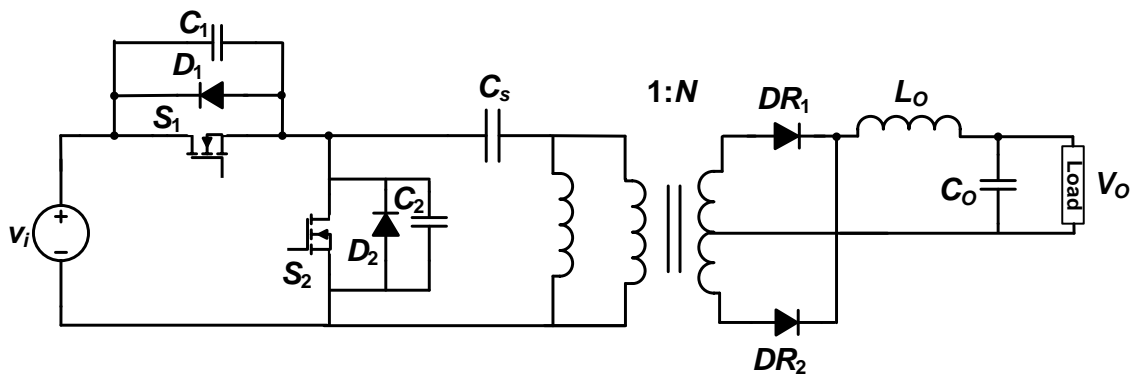


Fig. 1-16: Circuit diagram of APWM Parallel Resonant Converter

voltage to the converter increases, circulating current in the circuit increases. Due to this, this converter is only suitable for an application which runs at narrow range input voltage. This converter is only suitable for low output voltage and high output current. [17]

Fig. 1-17 shows a series- parallel resonant converter. [18] This combination attempts to take benefits of both series and parallel converter. With a proper selection of C_p this converter either becomes series- resonant converter or parallel- resonant mode. If C_p is not too small, then the circuit reverts to a parallel- resonant, so the converter is able to control the output voltage. As C_p gets smaller, converter approaches to series- resonant mode. [17]

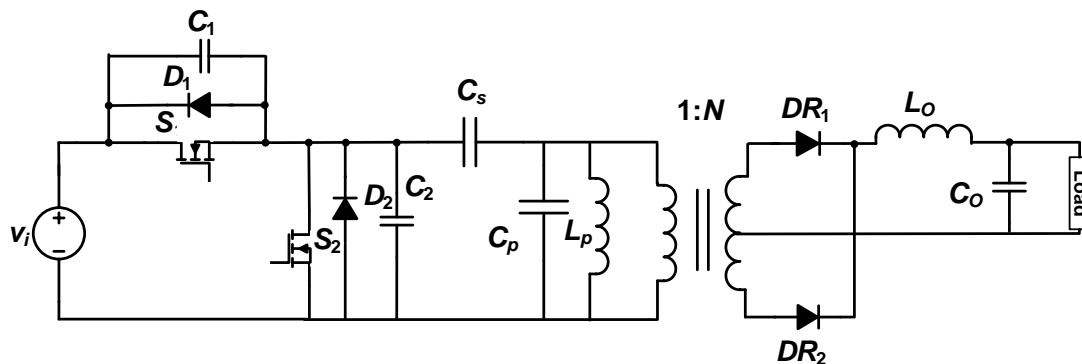


Fig. 1-17: Circuit diagram of APWM Series- Parallel Resonant Converter

1.4.3 Step- Up Converters Reported in Literature

To increase voltage level of PV panels in order to match with the grid, the gain of the power electronic converter has to be greater than 1. Therefore, buck converters are not suitable, instead, boost and boost- buck converter can be utilized. To achieve large gain, duty cycle of the converter has to be sufficiently high, however, higher duty cycle results in an increase of conduction losses. Consequently, the efficiency of converter drops considerably. How to achieve high step-up, low-cost, small-size, light- weight and high efficiency topologies are the main consideration in DC/

DC converter design. To attain this, several topologies with new configurations are presented and discussed in literature so far [21-41].

Fig. 1-18 shows a conventional interleaved boost converter. The interleaved structure is effective to increase the power level. This can minimize current ripple, resulting in component size reduction and enhanced transient response. [21-23] Because of current sharing, conduction losses in both active and passive components are reduced noticeably. This circuit consists of two inductors, two diodes, two switches with an output capacitor. Both switches are driven with same signal and same duty cycle. At the cost of additional components current ripple issue is improved,

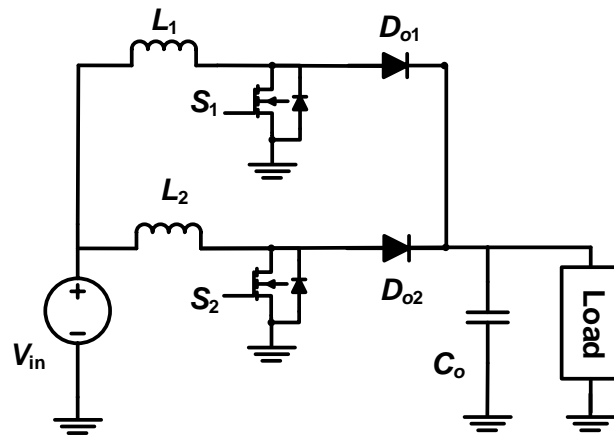


Fig. 1-18: Conventional interleaved boost converter

however, device still operates at hard- switching mode. Besides, in high- output voltage applications the efficiency is still limited as the diode reverse recovery problem is serious. A potential approach to reducing number of components, size and weight in this topology is to use one coupled inductor instead of using multiple inductors. [24-26] This can offer more benefits such as reduced core and winding loss, as well as improved switch current waveforms as ZCS is

achievable due to leakage inductance of coupled inductor. Besides electromagnetic emissions are decreased if properly implemented.

Fig. 1-19 illustrates a three- level boost converter. This topology can halve the voltage stress of the device and double the converter gain in compared to conventional boost converter. Due to this low voltage stress, switching losses are reduced and Electromagnetic noise is suppressed. Both conduction and switching losses are reduced in compared to conventional boost converter. Smaller inductor can be utilized with lower voltage level which yields higher power density, higher efficiency and lower cost. However, diode reverse- recovery problem is serious and the device operates with hard- switching. This topology is suitable for high voltage output applications. [27-28]

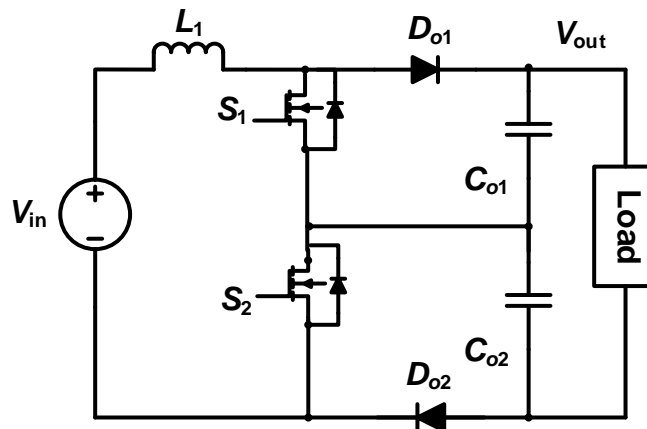


Fig 1-19: Conventional three level boost converter

Voltage conversion gain can be further increased to higher levels with less current ripple in a cascaded structure. Fig. 1-20 (a) shows a conventional cascade boost converter. [29] The first stage experiences lower voltage stress, as a result it can be operated with higher switching frequency to achieve higher power density. To reduce switching losses, second stage needs to operate with lower switching frequency. This topology requires two sets of components and control circuit. To

reduce complexity and the circuit cost, the integrated cascade boost converter is presented in Fig 1-20 (b). As can be observed, the two switches are combined into a single switch so complexity is reduced and component numbers are also decreased. When switch S is on, inductor L_1 and L_2 operate in charging mode. When switch turns off, the stored energy in L_1 is transferred to capacitor C_1 . In off-time interval, the energy stored in L_2 is delivered to the load through D_0 . This structure consists of three diodes, two inductors, two capacitors and one switch which is complex and expensive. [30-32]

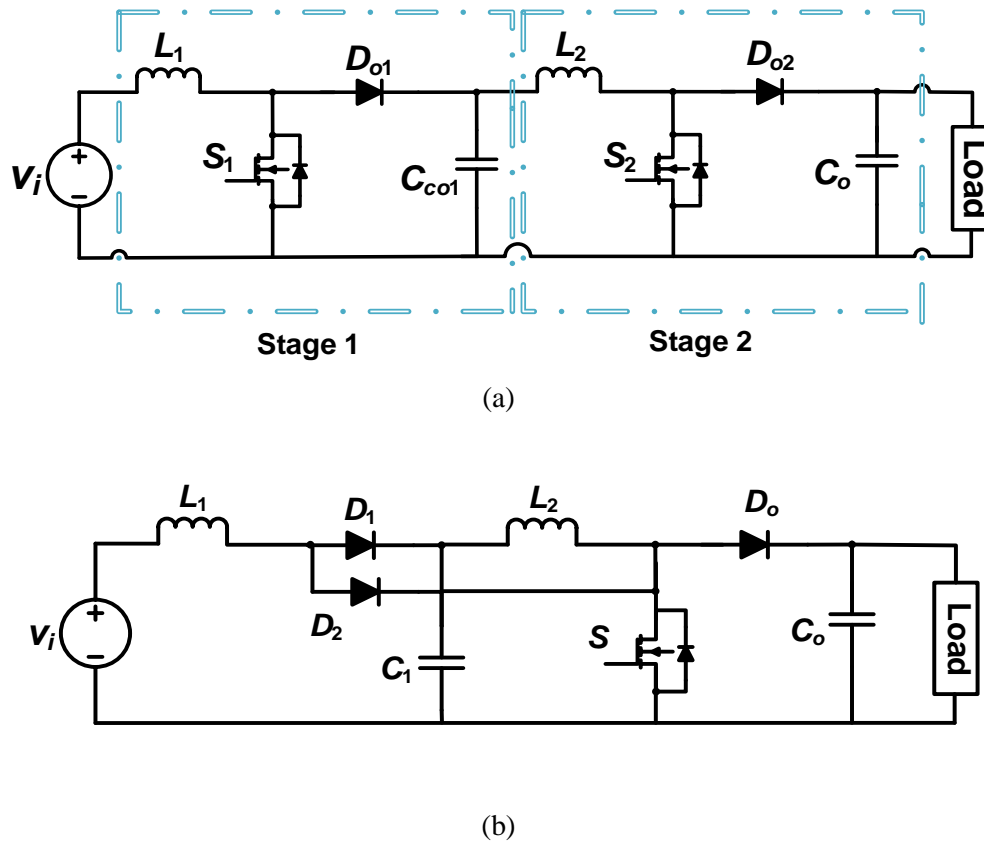


Fig. 1-20. (a) Cascade boost converter (b) Integrated cascade boost converter

In non-isolated DC/DC converters when an enlarged gain is required, coupled inductor can be employed which serves as a transformer. Fig 1-21 shows a very high step-up flyback-boost converter with a coupled inductor. This circuit is obtained by combining the conventional boost

converter with the flyback converter. The transformer of the flyback converter is integrated with the filter inductor of the boost converter. As the output of the flyback converter and boost converter are in series, a high voltage conversion is obtained from the circuit. A single switch is shared between both converters with a reduced switch voltage stress. [33-34]

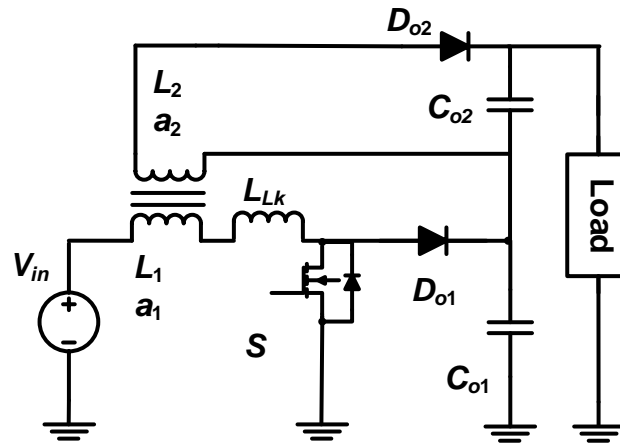


Fig. 1-21. Hybrid boost-flyback converter with a coupled inductor boost converter

Fig. 1-22 shows another single switch high step- up converter introduced in [35-36] The four-terminal switch cell shown in dashed block, consists of two diodes, two capacitors and a single switch. When switch is off, current flows through diodes D_1 and D_2 to charge C_x and C_y . When switch turns on, Capacitors discharge to the connected load and transfer power to it. In this topology the switch voltage stress is decreased by switch cell and the voltage gain is further extended. This topology is presented by integrating switch capacitors and boost converter together to obtain a high voltage gain. Major disadvantage of this topology are the large switching losses as the circuit operates with hard switching. Additionally, power level improvements are limited as

a large number of magnetic components are utilized. Consequently, they are better used in lower power applications.

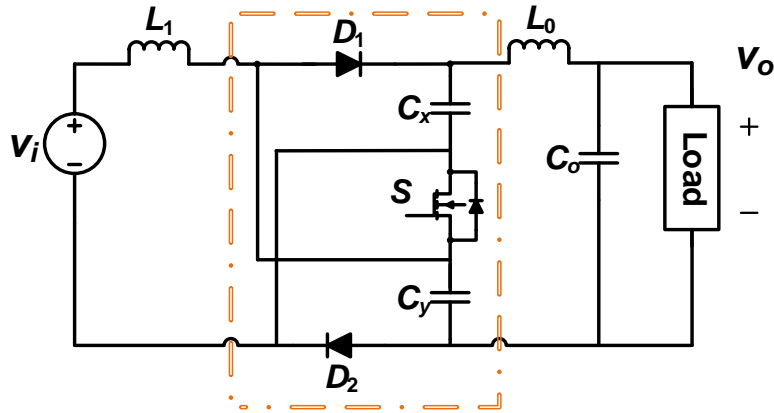


Fig. 1-22. High step up single switch converter

Fig. 1-23 shows a high- step- up interleaved boost converter with an auxiliary transformer. [37] This circuit is derived from deletion of the transformer existed in the isolated two- inductor boost converter. To couple the paths of inductor currents and to implement a current auto- sharing operation, an auxiliary transformer is implemented with a unity turn ratio. The current range is enlarged such that this circuit can be regulated form full load to no load. Disadvantage remaining in this circuit is the hard- switching conversion that deteriorates its efficiency.

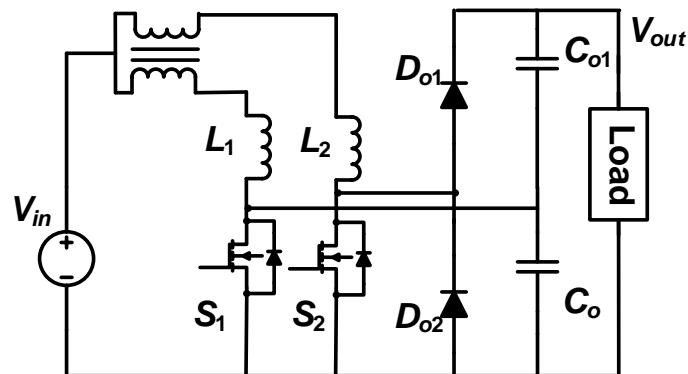


Fig. 1-23. Interleaved boost converter with an auxiliary transformer

Recently, there has been an increasing trend towards micro converters as it can be integrated into PV panel modules. This implies that converters should be compact and has light weight [38-39]. The aforementioned topologies [21]-[37] suffer from hard-switching operation which restricts the switching frequency and significantly deteriorate their efficiency; resulting in large size of the system. To minimize power loss in hard- switching boost converter, and to also make the converters more compact in size, two micro converters with soft-switching operation have been proposed in [40] and [41].

A half- bridge high- voltage- gain LLC micro converter has been discussed in [40]. This isolated topology is illustrated in Fig1-24 with two separate inductors and one transformer as magnetic components. Depending on the application, input voltage can also be applied to a full bridge chopper circuit. The power switches can operate with ZVS and the output diodes can achieve ZCS. Although high efficiency is achieved, the switching frequency has only hit maximum value of 100 kHz. Besides, the voltage step-up is realized through the use of high frequency transformer with large turns-ratio values; which altogether results in higher cost and big volume of the circuit.

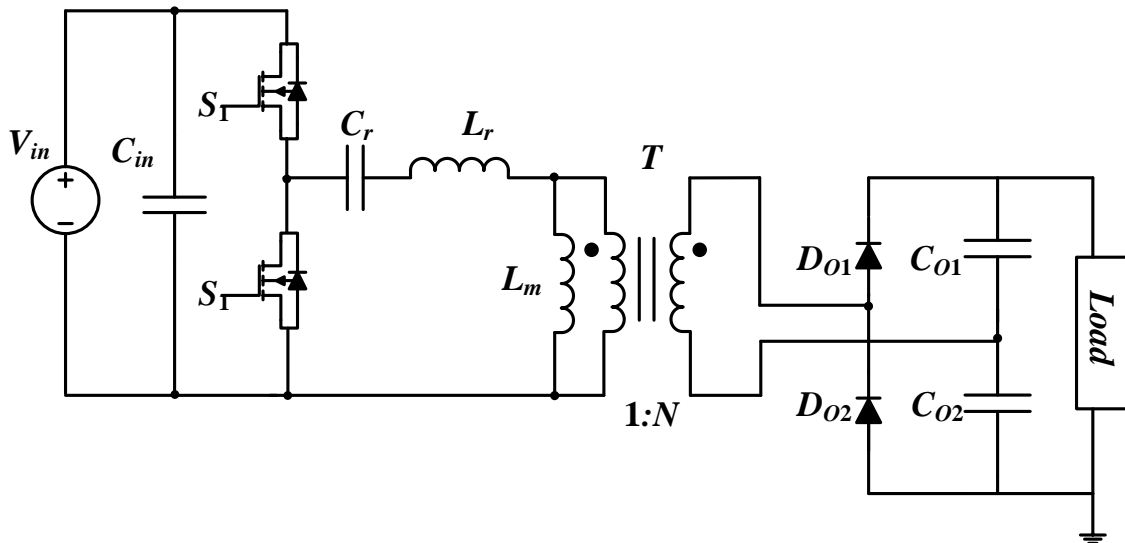


Fig. 1-24. Half-bridge soft- switching LLC micro converter introduced in [40]

To decrease system size, megahertz operation and optimized design of resonant converters has become a trend. Fig 1-25 illustrates a 1MHz series resonant DC/DC converter for PV applications which was introduced in [41]. The power losses are minimized as the zero- voltage switching turn-on and zero- current switching turn off is realized for the switches and diodes. Therefore, power efficiency is enhanced and small rated components are implemented in compared to [40]. However, the presented topology utilizes a high number of circuit elements which includes six switches; resulting in a high cost system. In addition, circuit components such as diodes experience high voltage stress.

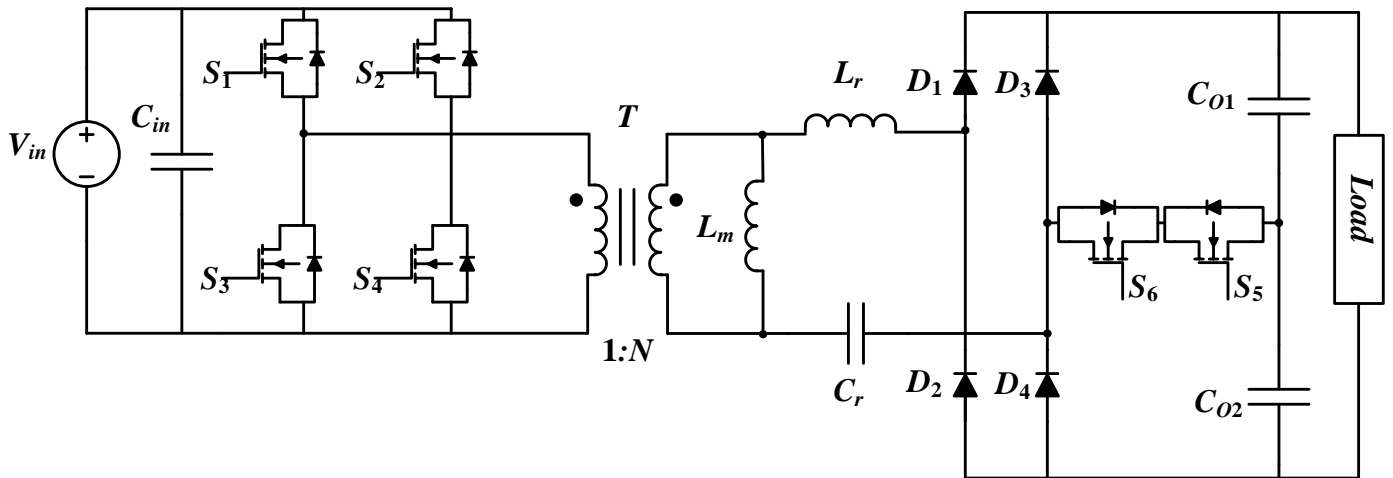


Fig. 1-25. Schematic of 1- MHz LLC series resonant converter introduced in [41]

1.5 Review on Maximum Power Point Tracking Techniques for PV Applications

PV energy systems have a varying output power affected by factors such as the position of the sun, the clarity of atmosphere and the cloud cover. Output power of PV panel is not a constant value and it varies with the irradiation and temperature. Fig. 1-26 gives the power- voltage curve of a PV for different light intensities. As can be observed, for each light intensity, there is only one operating point, known as maximum power point or MPP, at which output power is maximized. This issue brings us to the topic of Maximum Power Point Tracking or MPPT. Naturally, PV energy systems do not operate at this ideal condition as the location of this point is unknown. Hence, a controller is required inside of the converter to locate the optimal operating point such that the maximum power of panel is achieved. Fig. 1-27 shows an example of the overall systems.

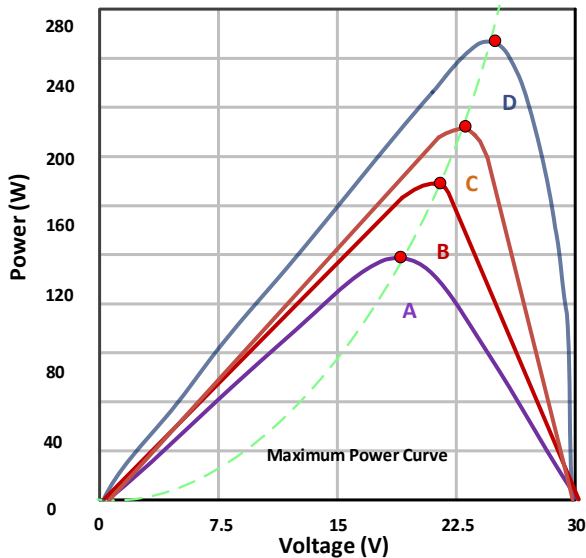


Fig. 1-26. Power- Voltage curve of a solar panel at various light intensities: $D > C > B > A$

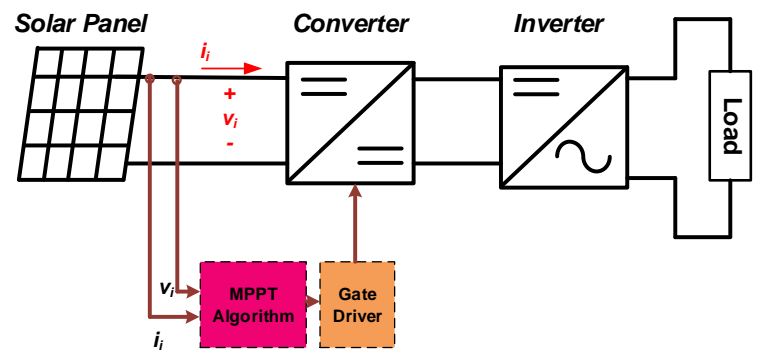


Fig. 1-27. A PV Panel connected to power electronic converter with integrated MPPT controller

There are numerous MPPT algorithms implemented in controllers so far, among which perturb and observe (P&O), incremental Conductance (IC) and Fuzzy Logic Control (FLC) received more

attention as they are more fitting to most PV applications. In this section, these three main techniques will be briefly discussed. [42-72].

1.5.1 Perturb and Observe

Due to its simplicity and generic nature, the perturb and observe (P&O) method is probably one of the most commonly used MPPT algorithm to date. [42-52] This method is based on the fact that at MPP the derivative of power as a function of voltage becomes zero ($dp=0$). By perturbing a control parameter of the converter (such as duty cycle), the operating point will change so that it gets closer to the point at which $dp=0$. When voltage of the converter is perturbed by applying control signal to the converter, the power change as well. If in next perturbation step $dp>0$, it means the operating point has moved towards maximum power and the applied change was correct. Therefore, the change in same direction will be applied to the control parameter until dp becomes zero. If $dp<0$, it means the applied change in the control parameter has moved it away from the MPP. In this scenario, the controller reverses the direction of next perturbation in compared to the previous step.

To comprehend the control strategy, Fig. 1-28 shows an example of a duty cycle-based P&O technique. As can be observed, if light intensity changes from A to B, the optimal operating point changes from 27 V to 32 V. To acquire new optimal point, a small change will be applied to the duty cycle parameter. If this change results in a boost in power, the MPPT algorithm will continue to move duty cycle in the same direction until MPP is achieved. If this results in power decrease, the direction of change will be reversed in next step [53].

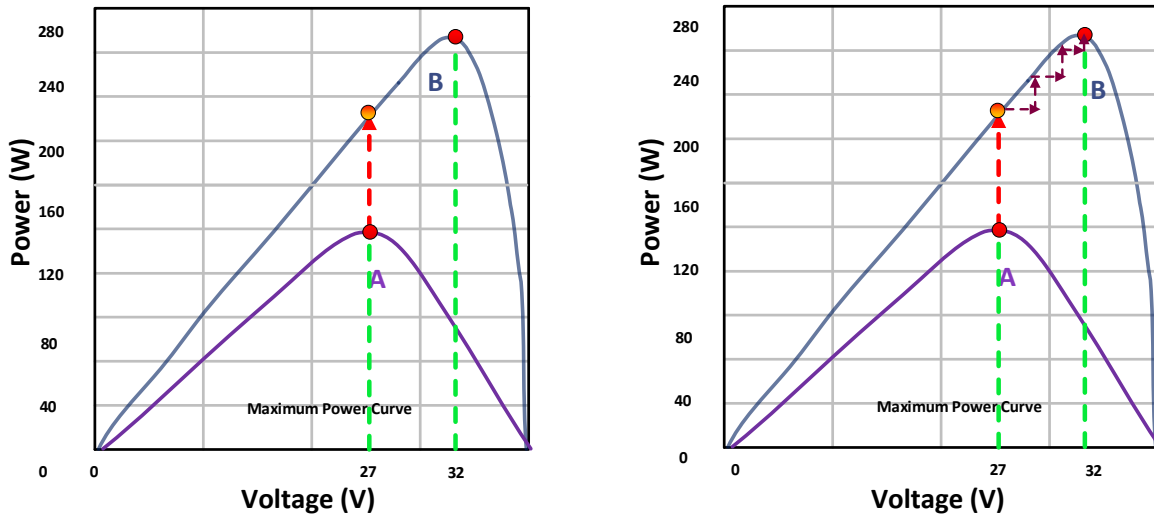


Fig. 1-28: Maximum power point tracking using conventional perturb and observe: (a) Light intensity increased, (b) moving towards high light intensity MPP operation

Perturb and Observe is an easy to be implemented as its structure is simple. It also has high efficiency at constant and high solar irradiation. The main disadvantage to this technique is that it can never operate at the MPP. Instead, it only oscillates around it due to the fact that controller will endlessly vary the control parameter. As well as that, rapid changes to the atmosphere deteriorates the algorithm functionality as it cannot adapt to sudden changes and may fail to track MPP practically.

1.5.2 Incremental Conductance

Incremental Conductance (IC) method is more advanced technique in MPPT. It also overcomes the issues found in P & O method. The IC method derives from the fact that at MPP the derivative of power with respect to voltage becomes zero. This derivative is zero at MPP, negative on the right side of MPP and positive on the left side of MPP curve. By setting the result of (1-9) equals to zero, (1-10)- (1-12) are derived as below. Incremental Conductance tracks optimal operating

$$\frac{dP}{dV} = \frac{d(IV)}{dV} = I + V \frac{dI}{dV} = I + V \left(\frac{\Delta I}{\Delta V} \right) \quad (1-9)$$

point by comparing the instantaneous conductance (I/V) to the incremental conductance ($\Delta I/\Delta V$) and applying a suitable change to the control parameter such as duty ratio. [54-60]

$$\frac{\Delta I}{\Delta V} = \frac{-I}{V} \quad \frac{dP}{dV} = 0 \quad \text{At MPP} \quad (1-10)$$

$$\frac{\Delta I}{\Delta V} > \frac{-I}{V} \quad \frac{dP}{dV} > 0 \quad \text{Left Side of MPP} \quad (1-11)$$

$$\frac{\Delta I}{\Delta V} < \frac{-I}{V} \quad \frac{dP}{dV} < 0 \quad \text{Right Side of MPP} \quad (1-12)$$

The goal of IC is to search for an optimal value of the control parameter at which the incremental inductance (I/V) becomes equal to the instantaneous conductance so that the system maintains its operation at MPP. Similar to P&O, by utilizing greater incremental size, faster tracking process can be developed. The main advantage of this technique is that it can achieve good results under very fast changing environment condition. Second advantage of IC over P&O is that this technique determines the moment it reaches MPP while P&O constantly oscillates around the optimal point. However, it requires both voltage and current sensor to measure the instantaneous voltage and current, resulting in higher costs. It also runs more complex mathematical set of equations which may result in a time-consuming and complicated process to achieve MPP. [61, 63].

1.5.3 Fuzzy Logic

One of the most powerful MPPT control techniques over last decade is fuzzy logic control [64-72]. This method deals with several truths. In other words, it functions based on several degrees of truth such as partially truth or partially false. FLC consists of three stages as Fuzzification, Interference and Defuzzification. There are two inputs in Fuzzy Logic technique: The error E and the Error Change (CE).

Fuzzification is the conversion process of input values into five linguistic variables: ZE (Zero), PB (Positive Big), PS (Positive Small), NB (Negative Big) and NS (Negative Small). Table 1-1 is a look up table at which FLC rules is provided. [67] Inference refers to the process at which the output is determined based on Table 1.1. This linguistic variable output is typically an appropriate perturbation in control parameter such as duty ratio. Once the output is selected, the type of output is changed from linguistic variable into a numerical variable through Defuzzification stage. At this stage, an analog signal is generated to control the power converter to move towards MPP.

To achieve more enhanced performance, a higher number of levels have to be used in FLC. However, the more levels used, the more complexity is associated to the control implementation. FLC has a great advantage of working with imprecise input values. It is easy to be implemented and very efficient. In addition, there is no need of certain mathematical equations and FLC can handle the non-linearity. However, this method consists of a relatively complex control method which requires multiple trial and error processes. [62]

Table 1-1. Fuzzy Logic Control rules base [67]

0	NB	NS	ZE	PS	PB
NB	PB	PB	PS	PB	PB
NS	PB	PS	PS	PS	PB
ZE	NS	NS	ZE	PS	PS
PS	NB	NS	NS	NS	NB
PB	NB	NB	NS	NB	NB

1.6 Electrolytic and Film Capacitors

For those PV converters discussed in section 1.4, capacitors with very large values are usually required for input filtering purpose (i.e. to ensure the input current has very low ripple current). For this reason, electrolytic capacitors are typically used due to their high energy density, meaning that they require very small physical size to store a significant amount of energy. Electrolytic capacitors are also more cost-effective and require much smaller system space than their film capacitors counterpart. However, the lifetime expectancy of electrolytic capacitors is relatively low, which can reduce the converter system life span. For instance, the lifespan of a 10 μ F electrolytic capacitor ranges from 1,000 hours (h) to 10,000h, while the PV panel life span is much higher than that of the electrolytic capacitor. Table 1-2 shows the characteristics of several different electrolytic capacitors available on the market.

Table 1-2. Examples of electrolytic capacitors and their characteristics

Electrolytic Capacitor	Capacitance	Rated voltage	Life expectancy
EEE-TG2A100P [73]	10 μ F	100 V	2000 h
UVZ2A0R1MDD [74]	0.1 μ F	100 V	1000 h
EEV-EB2E100Q [75]	10 μ F	250 V	4000 h
UVY2D0R1MED [73]	0.1 μ F	200 V	1000 h

Table 1-3. Examples of film capacitors and their characteristics

Film Capacitor	Capacitance	Rated voltage	Life expectancy
B32523Q1106K189 [76]	10 μ F	100 V	200,000 h
B32529C1104J189[76]	0.1 μ F	100 V	200,000 h
R60IR51005040K [77]	10 μ F	250 V	200,000 h
ECQ-E2104KF [78]	0.1 μ F	250 V	300,000 h

Film capacitors, on the other hand, have much higher life span than electrolytic capacitors. They are also less sensitive to the operating temperature, which makes them a better candidate for use in PV micro converters. To extend the life expectancy of the overall PV converter system, film capacitors can be utilized. Table 1-3 shows the characteristics of several film capacitors. It can be observed that the average life span of a film capacitor is at least 100 time that of the electrolytic capacitor.

To allow film capacitors to be used as the input filter capacitor, one approach is to utilize PV converter that is capable of drawing a continuous input current, thereby, the required input filter capacitance can be reduced. For this reason, the boost DC/DC converter that operates in continuous conduction mode (CCM) is a popular choice for PV converters.

1.7 Research Motivation

To ensure optimal energy system operation, it is required to integrate PV panels with power electronic converters. Existing DC/DC converters reported in literature suffer from several drawbacks such as a noticeable low efficiency due to hard-switching, costly and large-size components due to the use of higher rated components, high number of magnetic components, high voltage stress over diodes and switches and lower operation frequency to maintain continuous conduction mode. These drawbacks hinder the total system from achieving a desirable performance. The goal of this thesis is to address the downsides of the existing converters first, followed by proposing an improved topology for power electronic DC/DC converter. The proposed topology can be used in PV applications with integrated MPPT control scheme.

1.8 Thesis Contributions

In this thesis, a very high frequency micro-converter with extended soft switching operation using coupled magnetics for PV application is proposed. The contributions of this thesis research are summarized below:

1. Unlike the conventional DC/DC boost converter which has hard-switching, soft-switching is achieved for all switches in the proposed topology over an extended operating range (i.e. with ZVS turn-on and ZCS turn-off). By providing soft-switching operation, much high switching frequency (at least MHz) will be utilized in the proposed topology to reduce the physical size of all the passive components.
2. The input boost inductor and the auxiliary inductor in the passive auxiliary circuit in the proposed topology are integrated together using coupled magnetics, so that the number of

total magnetic components is reduced. The coupled inductor not only reduce the number of magnetic components required, but also helps to provide almost continuous input current and to provide extended soft- switching operations for both switches in the circuit.

3. The voltage stress across each switch in the proposed topology is much lower than those in the conventional boost converter. Hence, low-cost switches with lower voltage rating can be utilized.
4. Since the input current of the proposed circuit will operate in continuous conduction mode, this allows for the use of a small-sized film capacitor at the input side instead of an electrolytic capacitor, which typically has very short life-span. By eliminating the use of electrolytic capacitor in the proposed topology, the lifespan of the overall power conversion unit can be extended.
5. A custom-designed MPPT controller is also developed to work with the proposed micro converter topology to extract maximal amount of PV energy from the PV panel at various light intensities.

1.9 Thesis Outline

This thesis consists of 5 chapters. The organization of this thesis is as follows:

In Chapter 1, the background information of various power architectures for PV power conversion systems was provided. Then the review of different types of existing DC/DC converters for PV energy applications was presented. Their advantages and disadvantages of each converter was discussed. A brief summary of the MPPT control schemes was also presented at the end of this chapter.

In Chapter 2, a new micro converter utilizing coupled inductor with the ability to achieve soft switching in an extended range is presented. The detailed discussions on the circuit's operating principles, circuit's steady-state operating waveforms, circuit characteristics, design equations are provided in this chapter. In particular, the soft switching operating regions of the proposed converter are also explained in this chapter.

In Chapter 3, the modified MPPT control scheme that was implemented to support the proposed micro converter is discussed in detail. The presented MPPT control method is a tailored P&O methodology which is capable of achieving the optimal power point in a fast and accurate process for the presented converter.

In Chapter 4, the design and performance of the presented micro converter are provided. An example of the design procedure of the proposed converter is presented. Simulation and hardware experimental waveforms obtained from a proof of concept prototype are presented to highlight the merits of the proposed micro converter.

In Chapter 5, all thesis contributions are summarized. The future works related to this thesis are also highlighted.

2. Proposed Soft Switched DC/DC PV Micro Converter

As summarized in Ch. 1, the objective of this thesis research is to investigate and develop a PV micro converter topology with an extended soft switching operating range for all semiconductor switches, while at the same time, a continuous input current is achieved at the input without using large input filter capacitor. Based on the aforementioned objectives, a new micro converter is derived and presented in this Chapter. The derivation of the proposed converter circuit, converter's diagrams, converter's operating principles and operating stages, as well as the detailed theoretical analysis including the theoretical voltage gain calculations, soft-switching operation range will be discussed. Other alternative circuit configurations of the presented micro converter will also be described and explained at the end of this chapter.

2.1 Description of the Proposed PV Micro Converter

Fig. 2.1 shows the derivation of the proposed converter circuit. It is derived from the two-stage converter configuration that consists of a DC/DC boost converter followed by an asymmetrical-pulse-width-modulated (APWM) parallel resonant converter with a passive auxiliary circuit. The proposed circuit, shown by the bottom figure in Fig. 2.1, consists of an integrated boost converter circuit for performing MPPT and an APWM controlled parallel resonant converter with an auxiliary circuit for extending the ZVS operation for all switches. The boost circuit operates in continuous conduction mode (CCM) so that the input inductor current with reduced ripple current can be resulted. In addition, the boost inductor and the auxiliary inductor are coupled to each other

to minimize the number of magnetic components used in the final circuit. Table 2-1 gives the component list of the micro converter.

As shown in Fig. 2.1, the integrated boost circuit consists of input inductor L_{in} , the body diode D_1 of MOSFET S_1 , output capacitors C_1 and C_2 and switch S_2 which turns on with duty ratio D . When

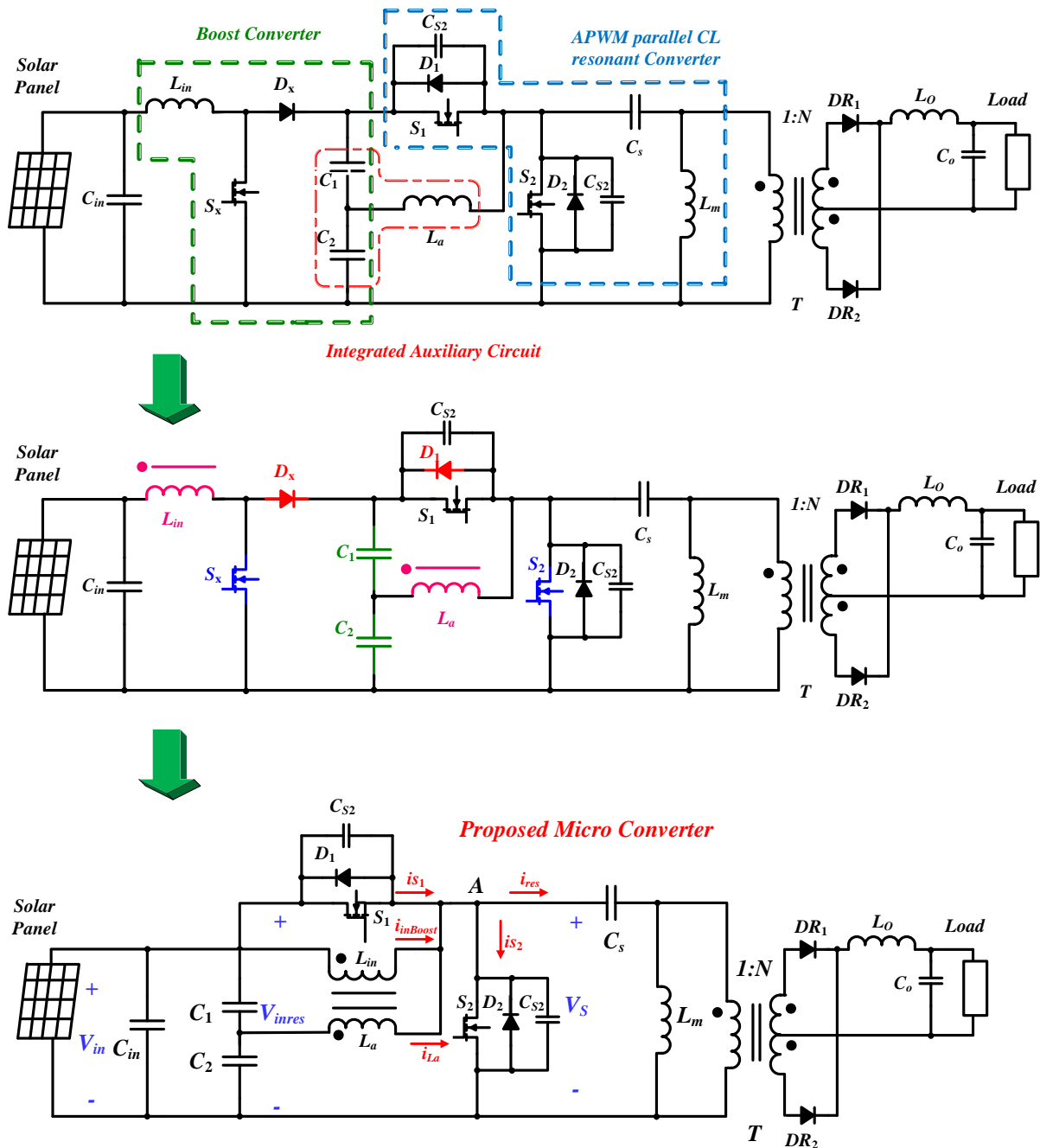


Fig. 2-1: Derivation of the proposed DC/DC converter

S_2 is on, body diode of MOSFET S_1 is reversed biased. S_2 is shared between both boost converter and APWM parallel resonant converter. The two switches conduct with complementary duty cycles with one another. Hence, S_2 turns on with duty ratio D , with a duty ratio of $1-D$ is applied to S_1 . The integrated auxiliary circuit consists of the auxiliary inductor L_a and capacitors C_1 and C_2 . L_a provides the additional compensating current in the resonant circuit as the duty ratio changes; hence, ZVS turn-on for both switches can be achieved at wide operation range [62]. To reduce the number of circuit elements, input inductor L_{in} and auxiliary circuit inductor L_a are combined into one coupled inductor. By doing so, CCM input current can be achieved while at the same time, soft-switching condition is also provided for both switches for much wider

operating range.

In general, the proposed converter works as follows: the variable voltage v_s turns into AC voltage through the resonant tank. The resonant capacitor C_S has two functions: 1) it blocks the DC component of the voltage v_s and 2) it forms a parallel resonant circuit with the magnetizing inductance of the transformer L_m to generate a sinusoidal resonant current for allowing the switches to achieve ZVS turn-on. A high frequency transformer with a turns ratio of $1:N$ is then used to provide electrical isolation, as well as stepping up the input voltage. Sinusoidal output voltage of

Table 2-1: Components used in the proposed micro converter

Component	Description
C_{in}	Input Capacitor
C_1, C_2	Boost circuit Capacitors
L_{in}	Boost circuit input inductor, Primary inductor of coupled inductor
L_a	Auxiliary circuit inductor, coupled with L_{in}
S_1, S_2	Switch
C_S	Resonant Capacitor
L_m	Parallel Resonant Inductor
T	High frequency transformer with turns- ratio $1: N$
DR_1, DR_2	Rectifying Diode
L_o	Filter inductor
C_o	Filter Capacitor

transformer is then rectified through DR_1 and DR_2 . Following that, C_o and L_o filters out the rectified voltage for high frequency ripples to provide a constant load voltage waveform.

2.2 Operating Principles of The Proposed Micro Converter

There are nine main operating intervals within a switching cycle of the proposed converter. The theoretical waveforms of the converter are shown in Fig. 2-2, with the corresponding operating stages shown in Fig. 2-3. For each interval, the converter operation is described as below.

[$t_0 < t < t_1$]: At the beginning of the period, gate signal V_{gs2} is removed from switch S_2 . Therefore, S_2 turns off and capacitor C_{S2} starts to charge. Due to negative resonant current i_{res} , and the positive current in auxiliary circuit i_{La} , capacitor C_{S1} is forced to discharge until the voltage across it reaches zero. At this time, switch diode D_1 starts to conduct to prepare switch S_1 for lossless turn-on in the next interval. The voltage across S_2 now equals $V_2 + V_1$ and the voltage across secondary coil of coupled

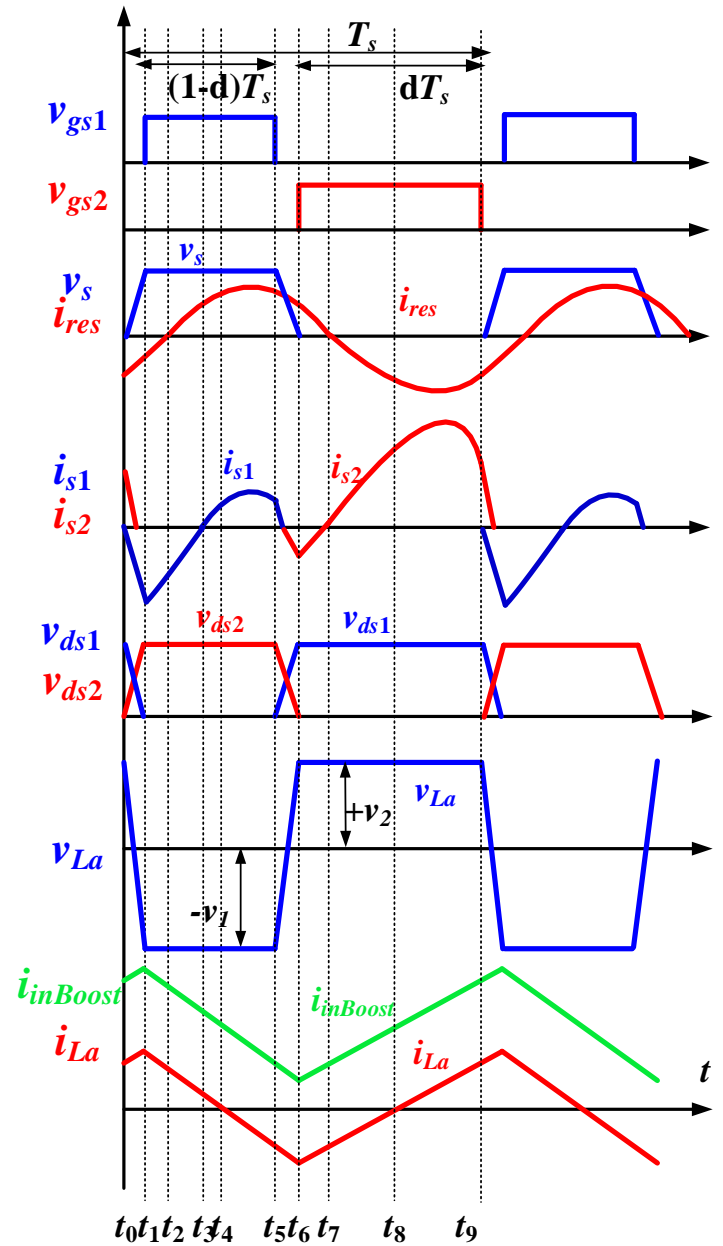


Fig. 2-2: Theoretical operating waveforms of the proposed converter

inductor V_{La} changes from $+V_2$ to $-V_1$; where V_2 and V_1 represents the voltage across capacitors C_1 and C_2 , respectively. During this interval, current in auxiliary circuit i_{La} reaches its positive peak and it starts to decrease in the next interval. Through boost converter circuit, energy stored in L_{in} is now transferred to parallel C_1 and C_2 . Fig 2-3 illustrates the operating stage of this interval.

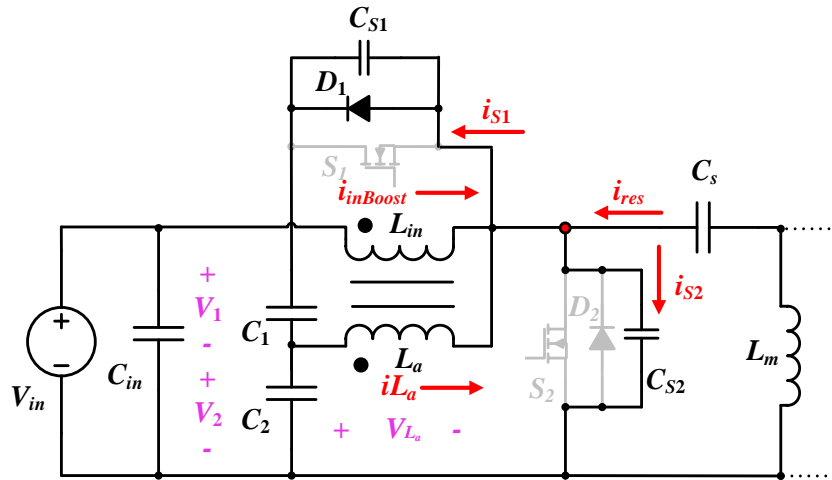
[$t_1 < t < t_2$]: At the beginning of this interval, V_{gs1} is applied to S_1 . Although S_1 is on, the voltage across it is negative so the current keeps flowing through the diode D_1 . During this interval, voltage V_{La} remains constant at $-V_1$. At the end of this interval, current i_{res} becomes zero and it increases to positive value in the next interval.

[$t_2 < t < t_3$]: In this interval, i_{res} changes its direction and starts to increase to positive values from zero. Diode D_1 is now reversed biased in boost circuit.

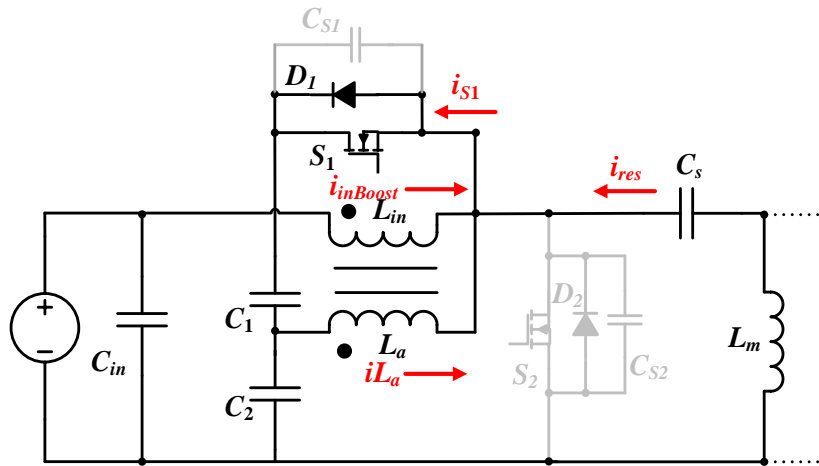
[$t_3 < t < t_4$]: In this interval Switch current i_{S1} changes its direction and it obtains positive value. The current flowing through D_1 in the prior stage now flows through S_1 and it turns on with zero power loss.

[$t_4 < t < t_5$]: Positive current in boost inductor and the positive current in switch S_1 makes the direction of auxiliary circuit i_{La} to drop into negative values.

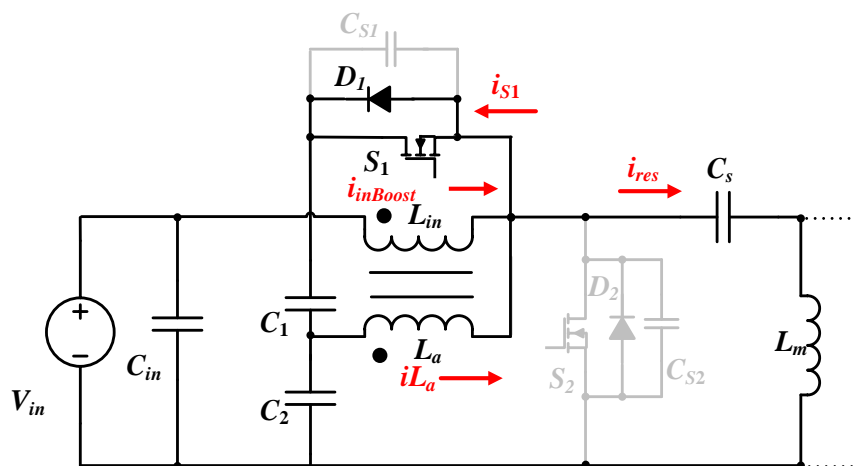
[$t_5 < t < t_6$]: At this interval, V_{gs1} is removed, so S_1 turns off. Following that, positive current i_{res} and negative current i_{La} in auxiliary circuit forces C_{S1} to charge and C_{S2} to discharge. Once C_{S2} is fully discharged, D_2 starts to conduct to set voltage across switch S_2 to 0 volts. Therefore, S_2 triggers on with ZVS in next interval. During this period voltage V_{La} changes from $-V_1$ to $+V_2$. This stage ends when i_{La} reaches its negative peak and switch S_2 turns on.



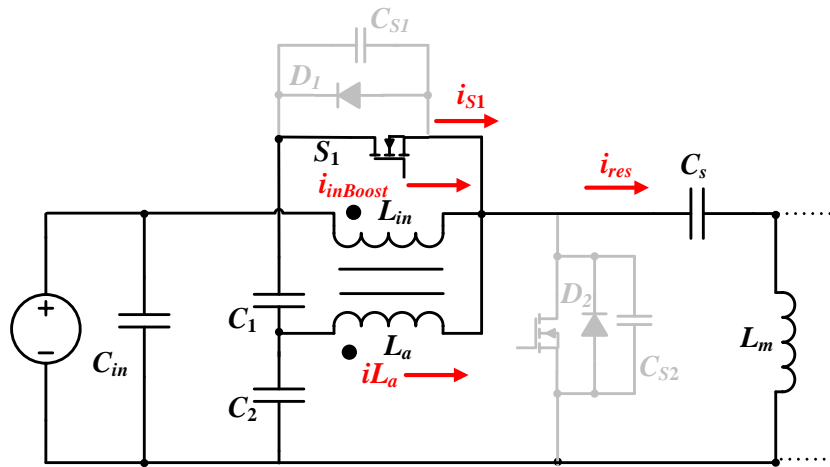
$[t_0 < t < t_1]$



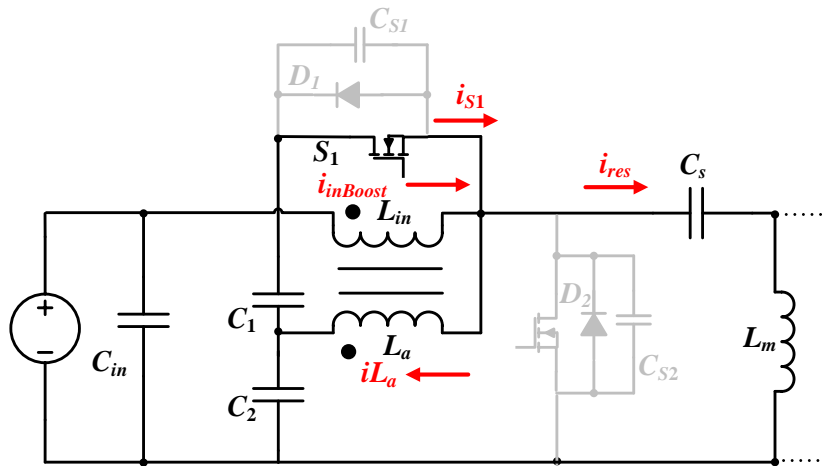
$[t_1 < t < t_2]$



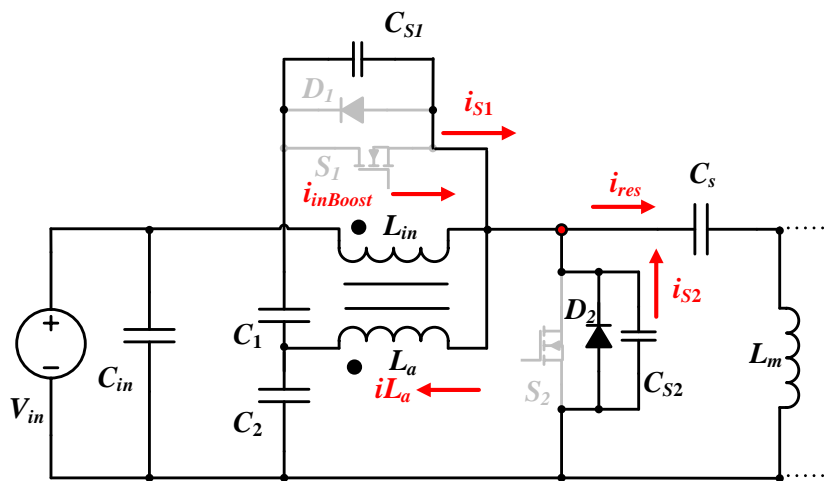
$[t_2 < t < t_3]$



$[t_3 < t < t_4]$



$[t_4 < t < t_5]$



$[t_5 < t < t_6]$

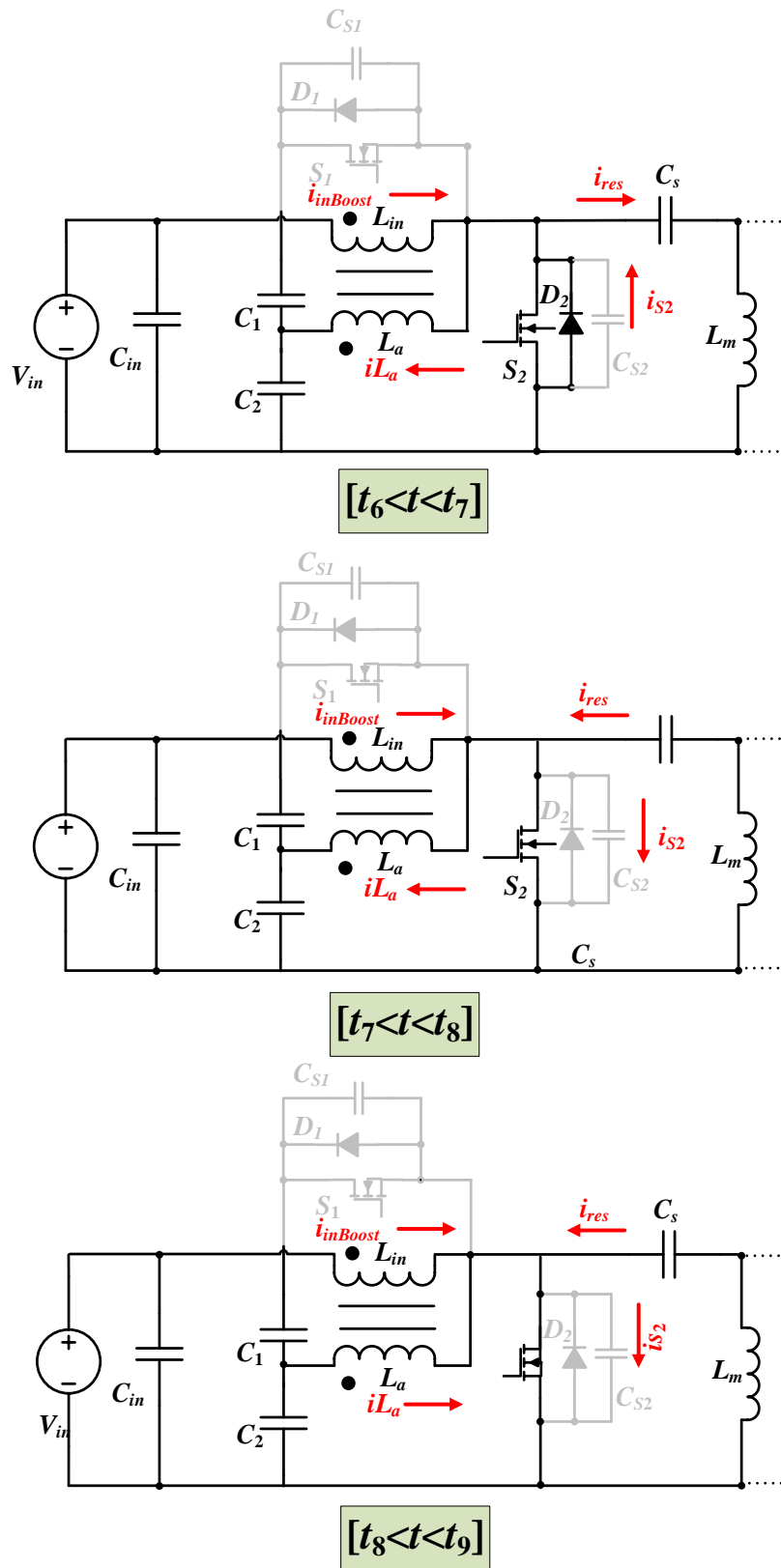


Fig. 2-3: Micro converter Operating stage

[$t_6 < t < t_7$]: At the beginning of this interval, S_2 triggers on with applying the gate signal V_{gs2} . The output voltage of APWM chopper now clamps to zero. Voltage V_{La} remains constant at $+V_2$ and i_{La} increases relatively to its positive peak point. Although S_2 triggers on, the voltage across it is still negative so the current keeps flowing through the D_2 . At the end of this interval i_{res} reaches zero value.

[$t_7 < t < t_8$]: Resonant current i_{res} starts obtaining negative values and the current flowing through D_2 now flows through S_2 so it turns on with ZVS. This stage ends when i_{La} becomes zero again. The stored energy in the resonant tank flows through S_2 to supply power to the load.

[$t_8 < t < t_9$]: i_{La} starts from zero and continues to rise linearly until it reaches the peak.

2.3 Theoretical Analysis of the Proposed Micro Converter

Kirchhoff's current law (KCL) states that for a parallel path, the total current entering a circuit junction is completely equal to the total current leaving the junction. Kirchhoff's voltage law (KVL) states that in a series closed loop path, the total sum of the voltage across each circuit component equals to zero. The inductor volt-second balance principle states that the average inductor voltage equals to zero.

By applying KCL and KVL principles, the characteristics of the proposed converter can be discussed. Fig. 2-1 shows the default direction of circuit component current and voltage. Equation (2-1) can be obtained by applying KCL to the junction noted as A.

$$\dot{i}_{inBoost} + \dot{i}_{La} + \dot{i}_{S1} = \dot{i}_{S2} + \dot{i}_{res} \quad (2-1)$$

By applying the inductor volt-second principle over one switching period ($(1-D)T_s V_1 = DT_s V_2$), and the fact that C_1 and C_2 split the half of input voltage of APWM chopper circuit ($V_1 + V_2 = V_{inres}$),

the steady state voltage of the auxiliary capacitors can be calculated as (2-2) and (2-3), respectively.

$$V_1 = DV_{inres} \quad (2-2)$$

$$V_2 = (1-D)V_{inres} \quad (2-3)$$

During intervals 2 to 5 [$t_1 < t < t_5$], by applying KVL, (2-4) is obtained. As switch S_1 is conducting, the voltage across it equals zero. Therefore, for voltage across auxiliary inductor, equation (2-5) is obtained.

$$v_{La} + v_{ds1} + v_1 = 0 \quad (2-4)$$

$$v_{La} = -v_1 \quad (2-5)$$

From interval 6 to 9 [$t_6 < t < t_9$], by applying KVL, equation (2-6) is derived. As switch S_2 is conducting during these intervals, the voltage across it equals zero. Therefore, for voltage across auxiliary inductor, (2-7) is obtained.

$$v_{La} - v_{ds2} + v_2 = 0 \quad (2-6)$$

$$v_{La} = v_2 \quad (2-7)$$

2.3.1 Proposed Micro Converter Voltage Gain

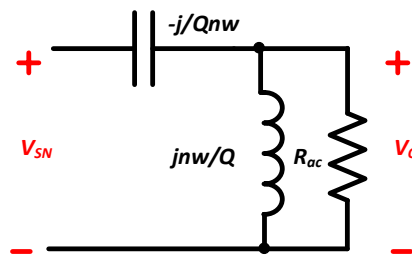
Regarding the overall voltage gain of the proposed circuit, first the input voltage of converter V_{in} steps up to the input voltage of the chopper circuit V_{inres} . This increase is realized through conduction of switch S_2 in integrated boost converter. The theoretical voltage gain of the integrated boost stage is given by (2-8); where D represents the duty ratio of switch S_2 in the proposed converter.

$$\frac{V_{inres}}{V_{in}} = \frac{1}{1-D} \quad (2-8)$$

After conversion of V_{in} into DC voltage V_{inres} , now V_{inres} sees APWM chopper circuit and is transformed into variable DC voltage v_s . This voltage is the output voltage of APWM chopper circuit which was discussed in section 1.4.2. Equation (2-9) gives the input voltage to the resonant tank v_s .

$$v_s = V_{inres} (1-D) + v_{sn} \quad (2-9)$$

Input voltage of parallel resonant network v_s possesses both DC and AC components as is expressed in (2-9). As was explained in section 2-1, the resonant capacitor C_S has the functionality of blocking the DC part of unidirectional voltage v_s .



Fig, 2-4: Equivalent Circuit of the resonant tank in the proposed micro converter

To further investigate the proposed micro converter performance, Fig. 2-4 is given which illustrates the equivalent n th harmonic of the parallel integrated resonant tank connected to the high-frequency transformer and the output load of the micro converter.

The AC voltage component v_{sn} is represented by the Fourier series in (2-10); where θ_n is the phase angle, n represents the n th order odd harmonic, Q represents quality factor of the circuit in Fig 2-3 which is given by (2.11), R_{ac} is the equivalent load resistance at the output of resonant tank given by (2-12), ω is relative operating frequency which is the ratio between operating frequency

of the micro converter ω_0 and its resonant frequency ω_r ; defining as $\omega = \frac{\omega_0}{\omega_r}$ where ω_r is given by (2-13).

$$v_{sn} = \sum_{n=1}^{\infty} \left(\frac{\sqrt{2}V_{inres}}{n\pi} \sqrt{1 - \cos(2n\pi(1-D))} \sin(n\omega_0 t + \theta_n) \right) \quad (2-10)$$

Where
$$\theta_n = \tan^{-1} \left(\frac{\sin(2n\pi(1-D))}{1 - \cos(2n\pi(1-D))} \right)$$

$$Q = \frac{R_L}{\omega_0 L_m} = \frac{R_{ac}}{\omega_r L_m} \quad (2-11)$$

$$R_{ac} = \left(\frac{\pi^2}{8} \right) \times R_L \times \frac{1}{N^2} \quad (2-12)$$

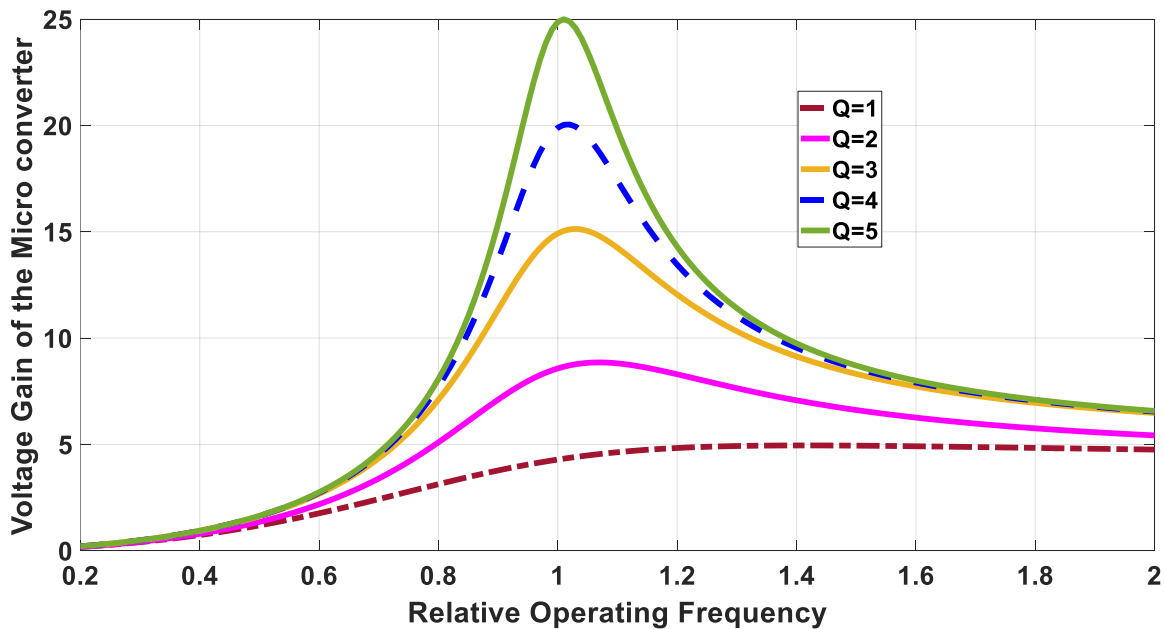
$$\omega_r = \frac{1}{\sqrt{L_m C_s}} \quad (2-13)$$

Harmonic components in the resonant circuit are assumed to be negligible, thereby fundamental approximation is used. The total voltage gain of the proposed topology is given by (2-14) which is calculated by multiplication of the following stages: 1) Integrated conventional boost converter gain 2) chopper circuit 3) Half bridge parallel loaded CL resonant converter 4) High frequency transformer turns- ratio as below.

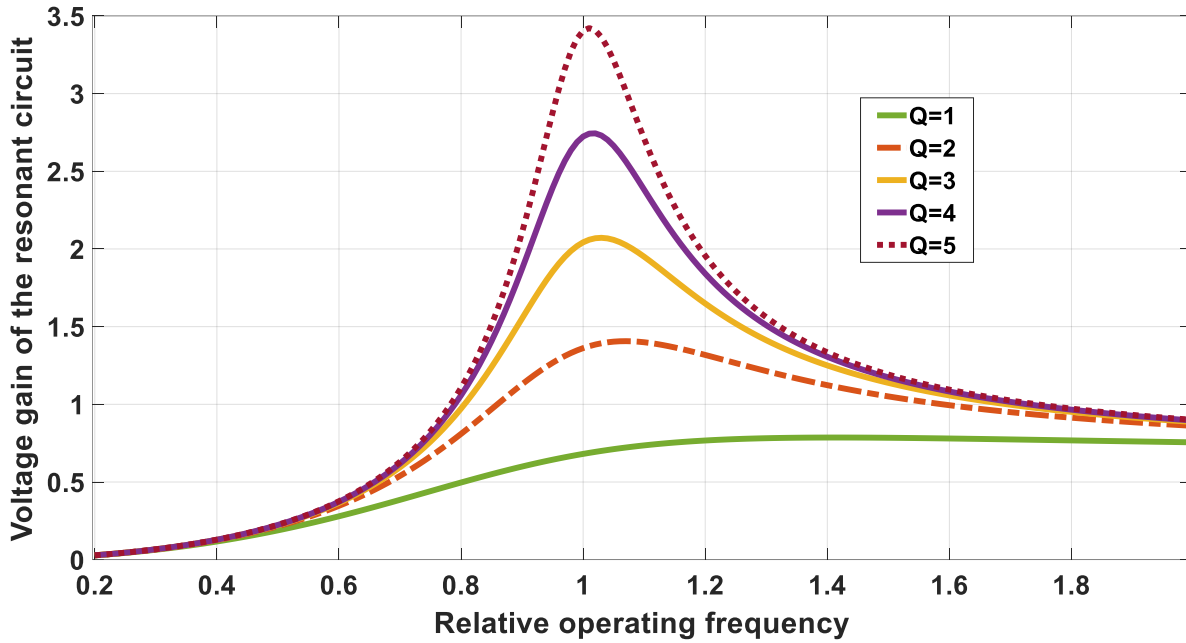
$$\frac{V_o}{V_{in}} = \left(N \times \frac{1}{1-D} \right) \left(\frac{1}{\frac{\pi^2}{8} \left(1 - \frac{1}{(n\omega)^2} - \frac{j}{(n\omega)Q} \right)} \right) \sum_{n=1}^{\infty} \left(\frac{\sqrt{2}}{n\pi} \sqrt{1 - \cos(2n\pi(1-D))} \right) \quad (2-14)$$

2.3.1.1 Voltage Gain vs Frequency

As is implied by (2-14), the voltage gain of the proposed micro converter is a function of duty ratio of the switches, quality factor and relative operating frequency. The turns ratio of the high-frequency transformer of the proposed micro converter is selected as 1:2 as the simulation in Chapter 4 is also carried out based on this parameter. Fig. 2-5(a) shows total gain of the micro converter given in (2-14) with respect to operating frequency at various quality factor values. These graphs are obtained at a fixed duty ratio value of 0.7. The relative frequency ranges from 0.2 to 2. From here it can be seen that higher gain is achieved when the micro converter is operating very close to resonant frequency. It is also comprehended that as quality factor increases, maximum obtainable gain also extends. This micro converter is the integration of boost converter, APWM parallel resonant converter and a high frequency transformer. To design the circuit components in Chapter 4, it is required to plot the gain graphs of the integrated parallel resonant. Fig. 2-5 (b) gives the gain of the CL resonant converter.



(a)



(b)

Fig. 2-5: (a) Proposed Micro converter voltage gain with $D=0.7$ (b) The resonant circuit gain at various quality factor values

2.3.2 Extended Soft- Switching Operation

In proposed micro converter which consists of boost and APWM resonant circuit, one switch may lose lossless turn- on when duty ratio is reduced or when the output load condition changes. The auxiliary circuit which is added to micro converter configuration in Fig 2-1 consists of a network of two capacitors (C_1 and C_2) and the secondary coil (L_a) of coupled inductor component. The coupled inductor provides compensating current such that switches S_1 and S_2 maintain ZVS over a wide range of duty ratio or loading conditions. The time variation of v_{La} and i_{La} can be calculated by (2-15) and (2-16), respectively [80].

$$v_{La} = \frac{2V_{inres}}{\pi} \sum_{n=1,3,5,\dots}^{\infty} \left(\frac{1}{n} \sin[n\pi D] \cos[n\omega_o t - n\pi(2-D)] \right) \quad (2-15)$$

$$i_{La} = \frac{2V_{inres}}{\pi\omega_o L_a} \sum_{n=1,3,5,\dots}^{\infty} \left(\frac{1}{n^2} \sin[n\pi D] \sin(n\omega_o t - n\pi(2-D)) \right) \quad (2-16)$$

As can be observed from theoretical operating waveforms at Fig. 2-2, The peak value of i_{La} occurs at $t=(DT_S)/2$ which is given by

$$I_{La-Peak} = \frac{1}{L_a} \int_0^{(DT_S)/2} V_2 dt = \frac{D(1-D)V_{inres}}{2f_o L_a} \quad (2-17)$$

In order to achieve ZVS for S_2 , turn- off current I_1 has to be positive. By applying KCL at the junction illustrated by red in Fig. 2-3 in interval $[t_5 < t < t_6]$, I_1 is obtained:

$$\begin{aligned} I_1 &= i_{res} - i_{inBoost,Min} - i_{La,Min} \\ I_1 &= i_{res} - i_{inBoost,Min} + i_{La,Max} \end{aligned} \quad (2-18)$$

Similarity, in order to achieve ZVS for S_1 , turn- off current I_2 has to be positive. By applying KCL at the red junction illustrated in Fig. 2-3 during interval $[t_0 < t < t_1]$, I_2 is calculated as

$$I_2 = i_{res} + i_{inBoost,Max} + i_{La,Max} \quad (2-19)$$

According to (2-18) and (2-19), to calculate turn- off current of switches in proposed micro converter, it is first required to obtain positive and negative peak current value of boost inductor.

Boost inductor maximal and minimal are given by

$$I_{inBoost,Max} = I_{inBoost,average} + \left(\frac{1}{2}\right)\Delta I \quad (2-20)$$

$$I_{inBoost,Min} = I_{inBoost,average} - \left(\frac{1}{2}\right)\Delta I$$

Where, ΔI represents the ripple current value of boost inductor given by (2-21) and $I_{inBoost, average}$ shows the average input current of the inductor as given by (2-22).

$$\Delta I = \frac{V_{in}(1-D)}{L_{in}f_o} = \frac{2\pi V_{inres}(1-D)^2}{L_{in}\omega_o} \quad (2-21)$$

$$I_{inBoost,average} = \frac{V_{inres}}{|Z_{in}|(1-D)} \quad (2-22)$$

By applying (2-21) and (2-22) into (2-20), maximum and minimum current of the boost inductor is finalized as given by (2-23).

$$I_{inBoost,Max} = \frac{V_{inres}}{|Z_{in}|(1-D)} + \frac{\pi V_{inres}(1-D)^2}{L_{in}\omega_o}$$

$$I_{inBoost,Min} = \frac{V_{inres}}{|Z_{in}|(1-D)} - \frac{\pi V_{inres}(1-D)^2}{L_{in}\omega_o} \quad (2-23)$$

It is also required to determine peak value of auxiliary inductor which was previously represented by (2-17). With the auxiliary circuit and integrated boost converter, the turn- off current I_2 of switch S_2 and the turn- off current I_1 of switch S_1 are given by (2-24) and (2-25) respectively, where input impedance to resonant tank Z_{in} of the per unit equivalent circuit of Fig. 2-4 is represented by (2-26), and ϕ_n represents the phase angle of Z_{in} .

$$I_1 = V_{inres} \sum_{n=1}^{\infty} \left(\frac{\sqrt{2}}{n\pi|Z_{in}|} \sqrt{1 - \cos(2n\pi(1-D))} \sin(2n\pi(1-D) + \theta_n - \varphi_n) \right) - \frac{V_{inres}}{|Z_{in}|(1-D)} + \frac{\pi V_{inres} (1-D)^2}{L_{in} \omega_O} + \frac{V_{inres} D(1-D)}{2f_O L_a} \quad (2-24)$$

$$I_2 = V_{inres} \sum_{n=1}^{\infty} \left(\frac{\sqrt{2}}{n\pi|Z_{in}|} \sqrt{1 - \cos(2n\pi(1-D))} \sin(\theta_n - \varphi_n) \right) + \frac{V_{inres}}{|Z_{in}|(1-D)} + \frac{\pi V_{inres} (1-D)^2}{L_{in} \omega_O} + \frac{V_{inres} D(1-D)}{2f_O L_a} \quad (2-25)$$

$$Z_{in} = \left(\frac{1}{1 + \left(\frac{Q}{n\omega}\right)^2} \right) + j \left(\frac{Q}{\left(1 + \left(\frac{Q}{n\omega}\right)^2\right)n\omega} - \frac{1}{n\omega Q} \right) \quad (2-26)$$

Introducing a variable M and Q which relates L_a to L_m as $M = (L_a / L_m)$ and L_{in} to L_m and $Q = (L_{in} / L_m)$, current I_1 can be normalized to its per unit value as

$$I_1 = \left(\frac{V_{inres}}{V_{inres, \min}} \right) \left(\sum_{n=1}^{\infty} \frac{\sqrt{2}}{n\pi|Z_{in}|} \sqrt{1 - \cos(2n\pi(1-D))} \sin(2n\pi(1-D) + \theta_n - \varphi_n) - \frac{1}{(1-D)|Z_{in}|} + \frac{\pi(1-D)^2 Q}{\omega Q} + \frac{d(1-D)\pi Q}{\omega M} \right) \quad (2-27)$$

Similarly, I_2 can be normalized to its per unit value as

$$I_2 = \left(\frac{V_{inres}}{V_{inres, \min}} \right) \left(\sum_{n=1}^{\infty} \frac{\sqrt{2}}{n\pi|Z_{in}|} \sqrt{1 - \cos(2n\pi(1-D))} \sin(2n\pi(1-D) + \theta_n - \varphi_n) + \frac{1}{(1-D)|Z_{in}|} + \frac{\pi(1-D)^2 Q}{\omega Q} + \frac{d(1-D)\pi Q}{\omega M} \right) \quad (2-28)$$

From (2-25) it can be comprehended that turn-off current I_2 is always positive for various values of duty ratio. Therefore, switch S_1 always achieve ZVS in all duty ratio conditions. Fig. 2-6 represents MATLAB graph of I_2 with respect to D at various values of quality factor Q and relative operating frequencies ω . This graph confirms the mathematical proof indicating that for all D values, I_2 is always positive so ZVS is easily achieved for switch 1.

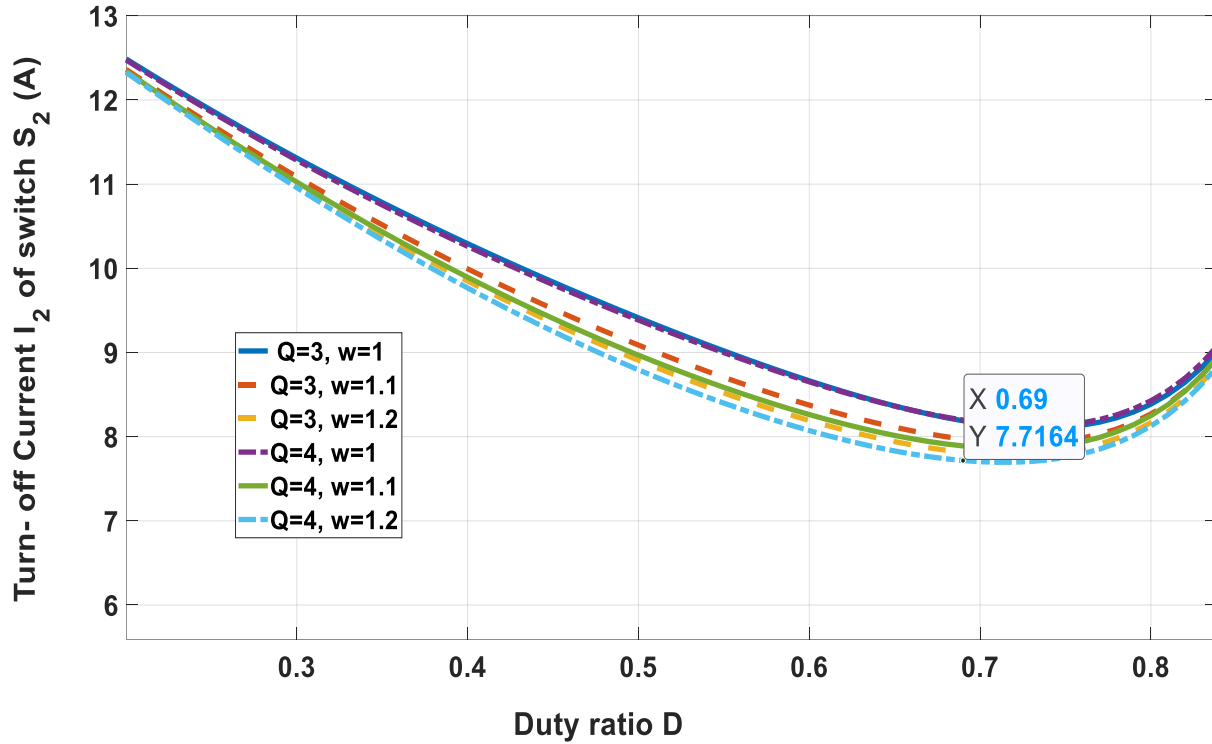


Fig. 2-6: Current through S_2 at turn off, I_2 , as a function of D in the proposed micro converter

To achieve ZVS for S_2 , turn-off current I_1 given by (2-24) must be positive such that switch S_2 turns on with zero power loss. Fig. 2-7 is plotted to show I_1 in the proposed micro converter. This graph is obtained at a wide range of duty ratio D with various quality factor Q and relative operating frequencies ω . This figure illustrates that with the selection of Q between 3 and 4, and with ω selected between 1 and 1.2, ZVS operation can be achieved in a duty cycle ranging from 0 to 0.76.

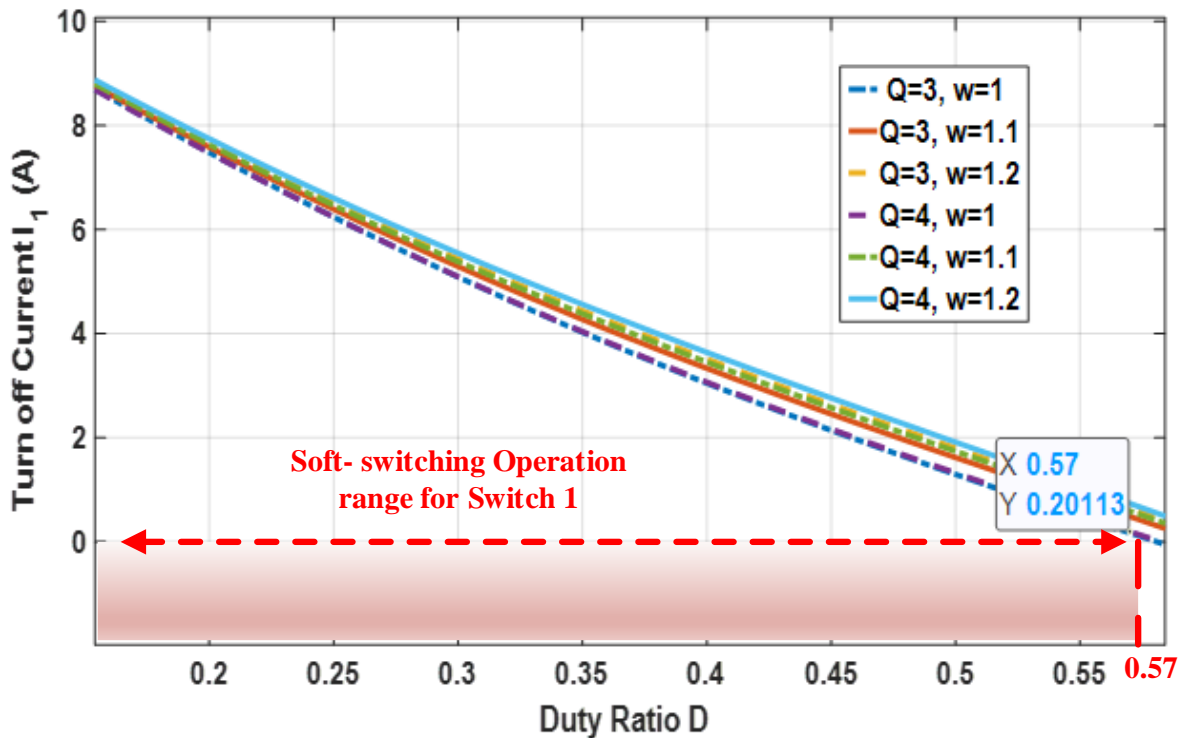


Fig. 2-7: Current through switch S_1 at turn-off, I_1 as a function of D in the proposed micro converter

To understand the extended soft-switching operation range in the proposed topology, Fig. 2-8 shows I_1 in the same micro converter topology without the aid of auxiliary circuit. This figure illustrates that with the selection of Q between 3 and 4, and w between 1 to 1.2, ZVS can only be achieved in a duty cycle value ranging from 0 to just above 0.57. In compared with the original topology of micro converter, this range is clearly limited. Therefore, the advantage of auxiliary circuit has also significantly contributed in achieving ZVS over a wider range of duty ratio value.

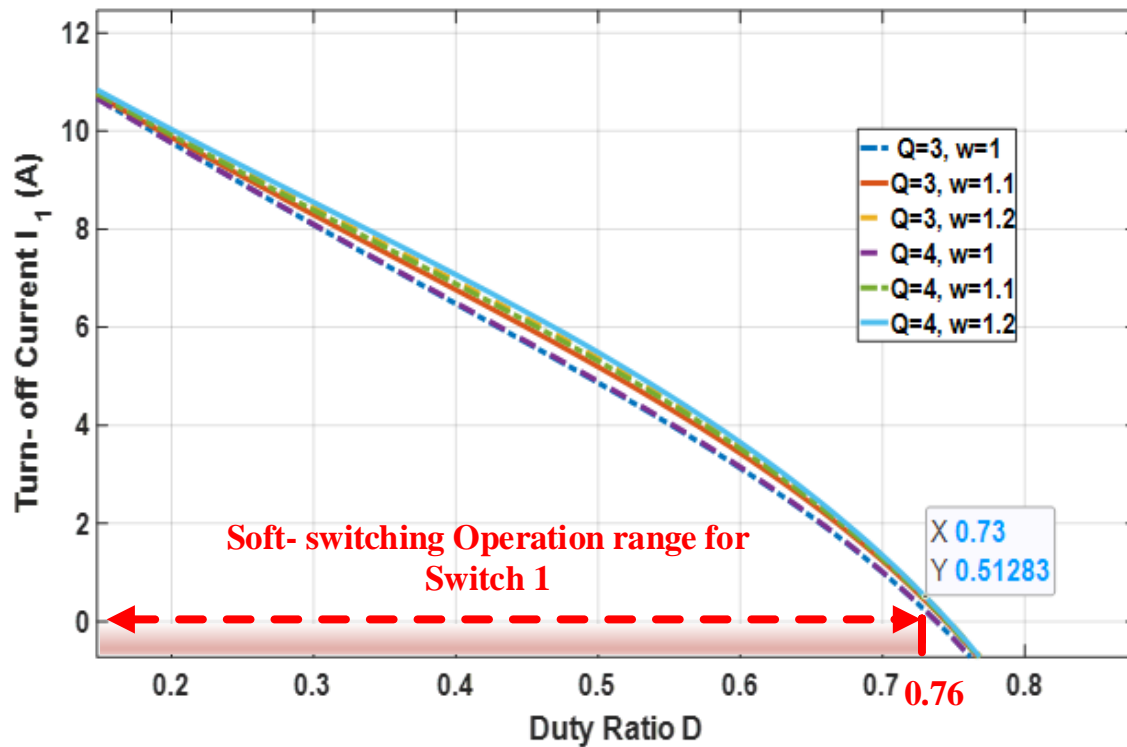


Fig. 2-8: Current through switch S_1 at turn- off, I_1 as a function of d in a same topology without auxiliary circuit

2.4 Derivation of Other Types of the Proposed DC/DC Micro Converter Topologies

Fig. (2-9)- (2-11) show several alternative topologies of the proposed micro converter. The configuration of all three topologies are similar to circuit diagram depicted in Fig. 2-1. They all include an APWM parallel converter consisting of a parallel inductor and series capacitor, an auxiliary circuit and the integrated boost converter, however, they are different in the load side stage configuration. The circuit diagram shown in Fig. 2-9 represents a non- isolated topology of Fig. 2-1. In this topology, there is no electrical isolation as the high frequency transformer is

replaced with a resonant inductor. Instead, the micro converter is directly connected to a full bridge rectifier.

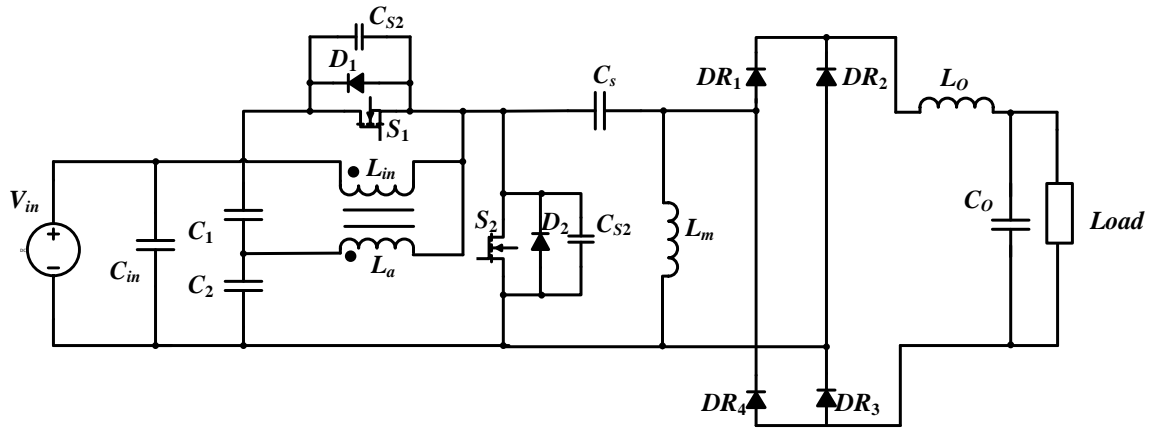


Fig. 2-9: Circuit diagram of the proposed micro converter: non- isolated topology

Voltage multipliers are a well- known rectifier that can be integrated with the proposed micro converter with or without transformer. Fig. 2-10 illustrates the use of a voltage doubler as the rectifying stage in a non- isolated topology of the proposed micro converter. In this topology, voltage stress of the capacitors is reduced in half (half of the output voltage). Accordingly, the

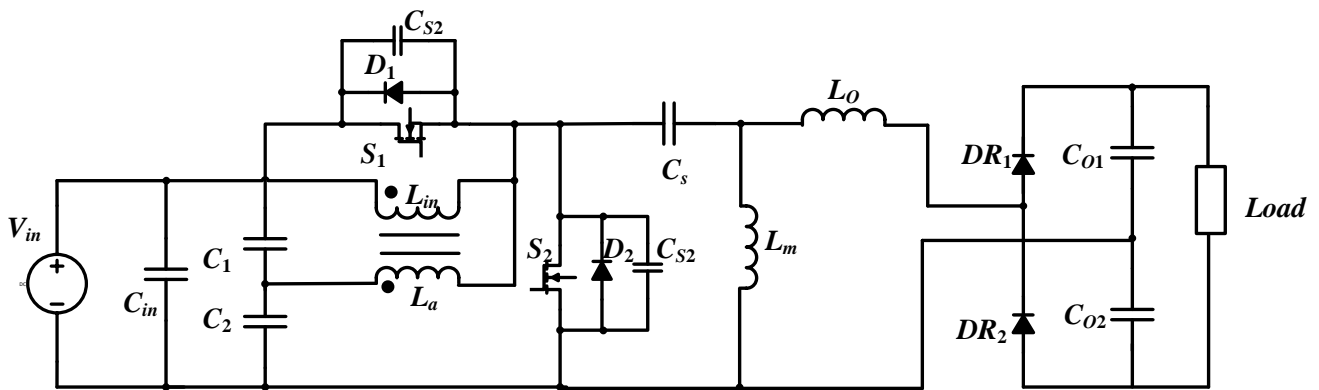


Fig. 2-10: Circuit diagram of the proposed micro converter: non-isolated topology with voltage- doubler

output voltage can be doubled compared to the circuit configuration shown in Fig. 2-10. This topology is suitable for high-output-voltage applications.

Voltage doubler can be integrated with isolated topology of the proposed DC/DC micro converter as is illustrated in Fig. 2-11. Likewise, voltage stress over output capacitors and diodes are decreased in half so the output stage can handle two times the output voltage in Fig. 2-1. This topology has the advantages of both Fig. 2-9 and 2-10; it is much more suitable for high voltage applications which requires load isolation.

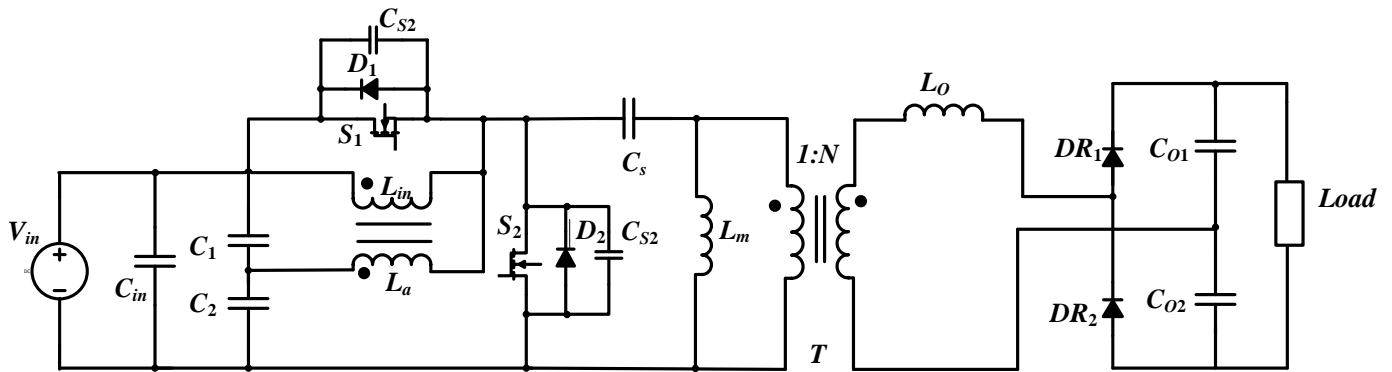


Fig. 2-11: Circuit diagram of the proposed micro converter: isolated topology with voltage- doubler

2.5 Summary

Chapter 2 introduced the proposed coupled- inductor based, photovoltaic micro converter with extended soft switching operation. The operating stages and operating waveforms of the micro converter have been discussed in detail with all the theoretical equations provided. Theoretical analysis based on the circuit parameters have also discussed and some MATLAB graphs are obtained to explain the characteristics of the proposed DC/DC micro converter.

3. MPPT Control Scheme for Proposed Micro Converter

To improve the performance of the conventional P&O algorithm used in PV energy systems, a modified P&O methodology is implemented as the control scheme for the proposed micro converter. This modified algorithm is able to converge to MPP fast and accurate at various light intensities. In this MPPT algorithm, the first drawback of constant oscillation in P&O is mitigated by applying an extra boundary check to the control loop. A second modification is also considered which is based on variable-size perturbation which helps the controller to find MPP faster when the converter is operating far from the optimal point. The theory is introduced in section 3.1, followed by the logic and related formulas that are provided in section 3.2. At the end of this section, a comprehensive flowchart of the modified MPPT is also provided that explains the algorithm in details. This chapter will be summarized in section 3.3.

3.1 Theory of the Modified P&O MPPT Algorithm

Based on the various maximum power tracking techniques described in section 1.5, the P&O algorithm is selected to be implemented with the proposed micro converter. As mentioned in section 1-5, the IC method requires more complex mathematical equations to achieve MPP. It also requires additional number of current and voltage sensors which results in higher system cost. Fuzzy logic method is not also selected in this micro converter as it requires several linguistic

variables that results in complexity of the controller. Hence, due to its simplicity, P&O based control method has been selected for this work.

Although the conventional P&O algorithm is simple, one main drawback with the P&O methodology is that the circuit will never operate at the optimal power point once it gets fairly close to the MPP. Instead, it will oscillate around this point due to the fact that the controller will endlessly vary the control parameter. With a bigger step size of control variable, the process of reaching MPP becomes faster especially when large change is applied to light intensities condition. However, with a big scale step size, the algorithm never converges the MPP and will oscillate around the optimal power point continuously. Oppositely, if the control step size is selected as a fixed small value, the controller takes significantly long to reach the maximal operating point when the light intensity changes. To overcome this drawback, a tailored P&O controller is applied to the proposed micro converter with variable-size based perturbation. This modified methodology would check and see if in two consecutive steps, the change in power is less than a specific positive value β . If this is the case, then no new change will be applied to the control parameter in the next step and the circuit keeps operating very close to MPP. Otherwise, if the change in power is greater than β , a variable- size perturbation will be applied to the control parameter. Control parameter in this methodology is the duty ratio of the switches in the proposed micro converter.

Considering the PV energy system characteristics depicted in Fig. 1-26, it is obvious that at the maximal operating point, (3-1) must be true.

$$\frac{dP}{dV_{in}} = 0 \tag{3-1}$$

By applying chain rule to (3-1), (3-1) can be re-written as

$$\frac{dP}{dV_{in}} = \frac{dP}{dD} \cdot \frac{dD}{dV_{in}} \quad (3-2)$$

Where V_{in} is the input voltage to the micro converter circuit diagram in Fig. 2-1 and D is the duty ratio applied to S_2

In case of a DC/DC boost converter, the input voltage is related to the output voltage and the duty ratio by (3-3), where V_o is the output voltage of the converter.

$$D = 1 - \frac{V_o}{V_{in}} \quad (3-3)$$

$$\frac{dD}{dV_{in}} = \frac{-1}{V_{in}^2} V_o \neq 0$$

Considering (3-1)- (3-3), it holds that

$$\frac{dP}{dV_{in}} = 0 \Leftrightarrow \frac{dP}{dD} = 0 \quad (3-4)$$

The above property has been discussed thoroughly in [79]. Based on [79], the function $P(D)$, for various light intensities, has only one extreme point, coinciding with the MPP of PV system. Accordingly, adjustment of duty-cycle in DC/DC converters based on (3-4) ensures convergence to the MPP under any light intensity condition.

The process of power maximization is shown in Fig. 3-1. As can be observed, the duty ratio adjustment follows the direction of dP/dD . Therefore, the value of duty cycle is increased in the right side of the MPP of the PV power curve; resulting in voltage deduction of the panel and an increase of output power. Similarly, when the starting point is on the left side of the MPP,

following the direction of dP/dD , duty ratio will continue to decrease such that the voltage and power will progressively increase until MPP is achieved.

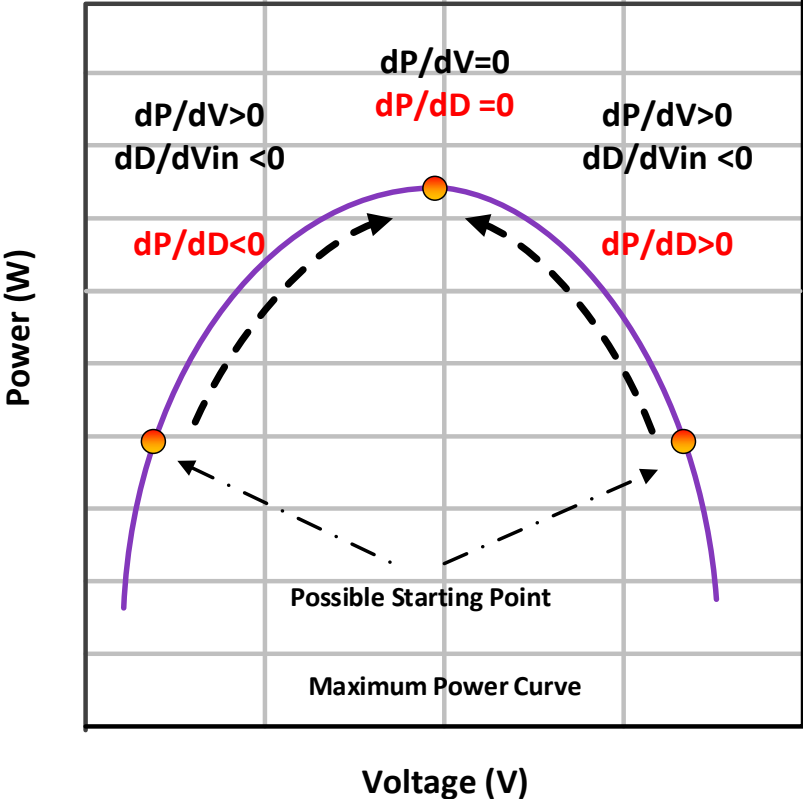


Fig. 3-1: Maximum Power Point Tracking Process of the presented micro converter

Table 3-1 shows the different scenarios of achieving maximum operating power point from different directions with different duty ratio.

Table 3-1: MPP tracking scenarios for the modified P&O method

Case #	Change in Power	Previous Change in duty cycle	Next Step change in duty cycle
1	$> \beta$	+	+
2	$> \beta$	-	-
3	$< - \beta$	+	-
4	$< - \beta$	-	+
5	$-\beta < \text{ or } < \beta$	\uparrow or \downarrow	No change

3.2 Control Logic of the Modified MPPT Scheme

The implemented P&O in the proposed micro converter consists of five dependent scenarios which differs from each other based on the change of power with respect to the previous iteration and the location of operating point on the power- voltage curve. These scenarios are shown in both Fig. 3-1 and Table 3-1. In the proposed micro converter, the operating point is varied by a perturbation to the duty ratio of the switches. This is due to the fact that the operating input voltage and duty cycle of the converter are mathematically related according to (3-3). This implies that when the operating duty cycle increases, the operating voltage decreases. This relationship can be utilized to estimate both the operating point of the panel and the direction in which MPP can be achieved. If both operating power and voltage has increased in compared to the previous step, it implies that the panel is operating at the left side of the MPP and its perturbation is on correct direction. Case 1 in Table 1-3 shows this case. Contrary to case 1, if both power level and voltage level decrease,

it implies that the operating point is on the right side of the power curve and the direction of perturbation is incorrect. Case 4 shows this condition in which the direction of perturbation needs to be reversed such that MPP can be reached. That is to say, a raise in duty ratio of the next step must be applied. In case 2 the change in power is positive while the change in duty ratio has been negative. This shows the operating point on the right side of the MPP of power- voltage curve of the panel in a movement towards MPP. This expresses that the direction of perturbation is precise and the duty ratio has to keep decreasing in the next step. Case 3 is the opposite of this condition in which the change in power is negative and the change in duty ratio is positive. In this case, the operating point is on the left side of the power- voltage curve and it is moving further from the MPP which is the wrong direction. Therefore, the change in duty ratio has to get inversed and becomes negative in the next step to put the tracking system on the right path. As was mentioned previously, to minimize the oscillation around MPP, the tracking controller algorithm checks to see if the absolute value of change in power is less than a specific positive amount β . If this is true, it signifies that the operating point is in in near region of MPP. Therefore, the controller won't apply new perturbation and it halts the duty ratio variation as is shown in Case 5.

To overcome the disadvantages of the conventional P&O, in addition to the boundary limit of β , a variable-size perturbation is selected in this MPPT algorithm. This changeable perturbation size is relative to the absolute value of change in power. If in two consecutive steps, the difference in power is a small value, then next step perturbation will be proportionally small. In this condition operating point is almost close to the MPP. Contrary to this scenario, if a big change happens to input power in two consecutive sampling steps, then a bigger magnitude of perturbation will be applied to the control parameter so that MPP convergence process becomes faster.

Fig. 3-2 shows the flowchart that demonstrates how this P&O MPPT controller performs. Initially, the controller obtains the panel output voltage and current value. Following that, the controller calculates the associated instantaneous power using (3-5); where k denotes the current operating state.

$$P(k) = V(k) \times I(k) \quad (3-5)$$

The controller also calculates next step input power using (3-5). From here, the controller calculates the difference occurred in power in the two successive steps as given by (3-6).

$$\Delta P = P(k) - P(k - 1) \quad (3-6)$$

Once the gap in power has been determined, MPPT controller will check to see if the absolute value of power is less than positive value β as shown in (3-7). This will verify whether the micro converter is operating in close region to MPP. If (3-7) is confirmed, the oscillation will be avoided and the duty cycle will not be changed any more.

$$|\Delta P| \leq \beta \quad (3-7)$$

If (3-7) is not the case, then the controller proceeds to determine how the control parameter must be perturbed to reach the optimal point rapidly. In order to achieve MPP, the control law of (3-8) has been implemented based on incremental PV power measurements, as follow

$$D(k) = D(k - 1) \pm \Delta D(k) \quad (3-8)$$

$$\Delta D(k) = S \cdot |\Delta P| \cdot \text{sign}(\Delta D(k - 1)) \cdot \text{sign}(\Delta P(k - 1))$$

Where $\Delta D(k-1)$ is the duty-cycle variation at step $k-1$; $\Delta P(k-1)$ is the change in power at step $(k-1)$; S is a constant value, $|\Delta P|$ is the absolute value of power change at step $k-1$ which contributes in adjusting the speed of the convergence to the MPP; and lastly the function $sign(n)$ is defined as

$$sign(n) = 1, \text{ if } n \geq 0 \quad (3-9)$$

$$sign(n) = -1, \text{ if } n \leq 0$$

In the beginning of the control algorithm, an initial duty ratio value of $D_{(0)}$ as well as a small perturbation $\Delta D_{(k-1)}$ is given to the control unit as the input of the algorithm. As the controller may operate at very much higher speed in compared to the micro converter, a sampling time is also considered in this methodology. This sampling time adds some delay in such a way that voltage and current will be measured once a specific number of cycles is passed. To implement this, a parameter referred to as counter max is implemented into MPPT algorithm. The MPPT algorithm counts each time that the code is processed and once it reaches the counter max specific number, it changes to sampling mode and measures the corresponding parameters.

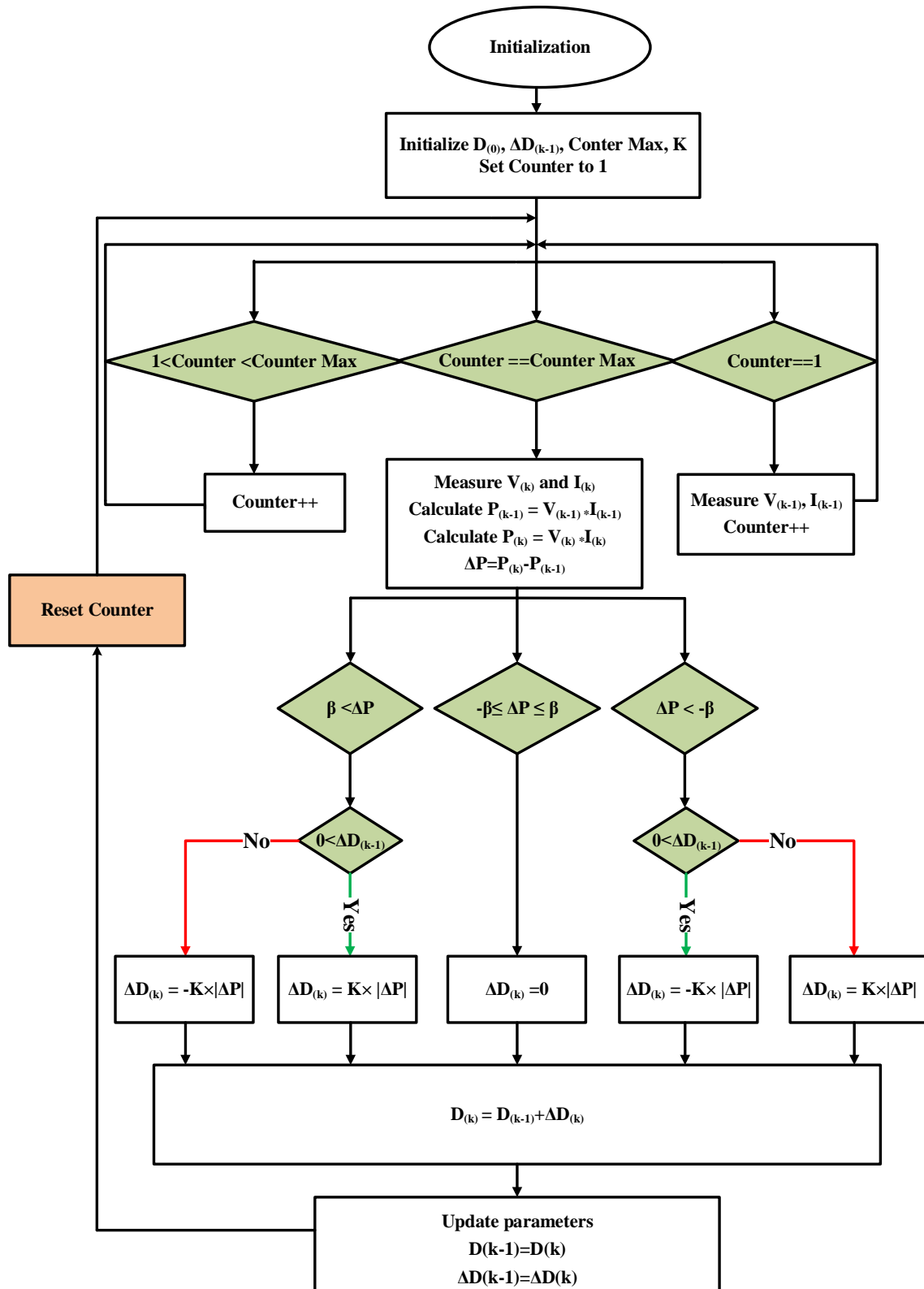


Fig. 3-2: Modified P&O maximum power point tracking controller implemented with the proposed converter

3.3 Summary

This chapter presented the tailored MPPT scheme that is implemented with the proposed DC/DC micro converter. The control principles of the MPPT algorithm are based on the P&O control methodology discussed in section 1.5. The algorithm is adjusted such that the oscillation near the optimal power point is alleviated and the speed of convergence process is accelerated. A flowchart of the modified MPPT algorithm and its operating states have been explained in this chapter.

4. Design and Performance of the Proposed Micro Converter

4.1 Introduction

In this chapter, a design example of the proposed micro converter is given. Then the proposed circuit and the designed MPPT controller are implemented in PSIM with the required system design specifications. The proposed circuit is simulated to confirm that it is capable to operate under continuous conduction mode and is able to achieve ZVS under an extended range of duty ratio. The printed circuit board (PCB) of the hardware prototype is then designed using ALTIUM DESIGNER. The hardware experimental works, together with the simulation results obtained from PSIM will be provided in this chapter to highlight the functionality and advantages of the proposed circuit.

4.2 Design Specifications in Powerism

To validate the functionality of the proposed DC/DC micro converter, a single 210W solar panel connected to the proposed isolated micro converter shown in Fig. 2-1 is simulated in PSIM. According to (2-14), the gain of the whole proposed micro converter with isolation equals to multiplication of the individual voltage gain in the following stages: boost converter gain, APWM parallel resonant converter gain and the gain of high frequency transformer. In this simulation, high frequency transformer turns ratio N is selected as 2. As was illustrated in Fig 2-5 (b), in order to attain a resonant circuit gain of $V_o/V_{in}=2$, quality factor Q can be considered as 3. Therefore, $Q=3$ is selected to further design the rest of circuit components. One of the highlighted purposes

of this thesis is to achieve soft switching at very high frequency range. Thus, an initial operating switching as $f_o = 1.2$ MHz is assumed. Output resistance is selected as $R_L = 600\Omega$; hence the equivalent load at the output of resonant tank is calculated using (2-12). By rearranging (2-11), resonant inductor value is calculated as

$$L_m = \frac{R_L}{Q\omega_o} = \frac{600}{3 * 2 * \pi * 1.2M} = 6.63\mu H$$

By a selection of $L_m = 7\mu H$, by considering the fact that for ZVS operation switches must conduct at a switching frequency higher than resonant frequency and by using (2-13)

$$\omega_r < \omega_o \Rightarrow \frac{1}{\sqrt{L_m C_s}} < 2 * \pi * 1.2MHz$$

$$C_s > 2.5nF$$

C_s is selected equal to 3nF, resonant frequency of the proposed micro converter is accordingly calculated as

$$f_r = \frac{1}{2 * \pi * \sqrt{L_m C_s}} = \frac{1}{2 * \pi * \sqrt{7 * 2.5 * 10^{-15}}} = 1.203MHz$$

One of the highlights of this thesis is to ensure that input current operates at CCM while keeping soft-switching at the extended duty ratio range. By definition, at the boundary of continuous conduction mode, the input inductor current $i_{inboost}$ goes to zero at the end of the off interval. Therefore, to ensure CCM operation, equation (4-1) is being used [16].

$$I_{inboost,B} = \frac{1}{2} i_{inboost,peak} = \frac{T_S V_{inres}}{2 * L_{in}} D(1-D) \quad (4-1)$$

To design the boost circuit stage, a gain of $V_{inres}/V_{in}=2.5$ is considered. For an input power of 210 W, an input voltage of 35V, a duty ratio of 0.7 and an operating frequency of 1.2 MHz, minimum value of L_{in} is required such that the converter always operates at CCM mode. By rearranging (4-1), the average value of the inductor at the boundary between continuous and discontinuous conduction is calculated as

$$L_{in} = \frac{T_S V_{inres}}{2 * I_{inboost,B}} D(1-D) = \frac{1}{1.2MHz_s} \frac{2.5 * 35}{2 * 7} (0.7) * (0.3) = 1.1 \mu H$$

Therefore, if $L_{in}=1.1 \mu H$ is used, the converter will operate at the boundary between continuous and discontinuous mode. To further ensure a CCM operation, an inductor larger than $1.1 \mu H$ must be used. To estimate the right inductor for the proposed micro converter, the following equation can be used [81]

$$L_{in} = \frac{V_{in} (V_{out} - V_{in})}{\Delta I_L * f_S * V_{out}} \quad (4-2)$$

Where ΔI_L is the estimated inductor current ripple that can be calculated using

$$\Delta I_L = (0.2 \sim 0.4) * I_{OUT(max)} * \frac{V_{out}}{V_{in}} \quad (4-3)$$

Where $I_{OUT(max)}$ is the maximum output current required in the application. By considering a current ripple of 0.5, a gain of 2.5 and the switching frequency as 1.2 MHz, input inductor is calculated using (4-2) as below

$$L_{in} = \frac{35(87.5 - 35)}{0.6 * 1.2MHz * 87.5} = 29\mu H$$

Coupled inductor implemented in this topology is selected with unit turn- ratio, so auxiliary inductance L_a has the same value as L_{in} .

To adjust the output capacitor values C_1 , C_2 equation (4-4) is given [16].

$$C_{OUT} = \frac{I_o DT_s}{\Delta V_{OUT}} \quad (4-4)$$

The peak- to- peak voltage ripple of the output ΔV_{OUT} is desired to be around 2 %. Therefore, output capacitor of boost converter which is the sum of parallel C_1 , C_2 is calculated as below.

$$C_{OUT} = \frac{\frac{210}{115} * 0.7}{1.2MHz * 2} = 540nF$$

Table 4-1 shows all the component parameters which are selected for the isolated DC/DC micro converter. Component values given in table 4-1 are considered as ideal. However, to study a real- life scenario all non- ideal component parameters should be inserted into PSIM software as well. These non- ideal parameters include the inductor resistance, switch on- resistance and diode forward voltage. These parameters are derived from the component datasheets and they are reported in Table 4-2.

Table 4-1: Component values

Parameter	Component Value
Input Voltage	35V
Rated Power	210W
Input Capacitor C_{in}	10 μ F
Output Capacitor C_o	10 μ F
Output Inductor L_o	330 μ H
Resonant Capacitor C_s	3 nF
Resonant Inductor L_m / Primary Winding Magnetizing Inductance	7 μ H
Boost Inductor L_{in}	22 μ H
Boost parallel capacitors C_1, C_2	290 nF
Auxiliary inductor L_a (Coupled with boost inductor L_{in})	22 μ H
Primary Turns	1
Secondary Turns	2
Tertiary Turns	2
Operating Frequency	>1 MHz
Control Variable for achieving MPPT	Duty ratio
Load	600 Ω

Table 4-2: Non-ideal parameters

Parameter	Component Value
Input Inductor resistance	65 mΩ
Auxiliary Inductor resistance	65 mΩ
Resonant Inductor resistance	20 mΩ
Output Inductor resistance	325 mΩ
Diode Forward Voltage	3.2 V
Diode Resistance	35 mΩ
Switch on Resistance	540 mΩ
Switch output capacitance C_{oss}	80 pF
Switch output capacitance C_{iss}	250 pF
Body Diode Forward Voltage	2.5V

The circuit is implemented in PSIM to obtain simulation result waveforms and to further verify the highlighted merits of the proposed micro converter. This circuit consists of an input DC voltage source which accounts as the light intensity, connected to a single 210W solar panel that is attached to the proposed micro converter as shown in the appendix.

The output voltage of the solar panel can provide a DC voltage ranging from 0 to 40V to the micro converter. Solar panel was designed through the use of the “solar panel physical model” in PSIM. Various parameters were obtained from a particular solar panel’s datasheet in order to re-create the panel’s power-voltage and current-voltage curves such that the panel can be precisely simulated in PSIM.

The frequency of the micro converter is fixed and is selected very close and slightly above the resonant frequency. To test the functionality of this circuit first its performance is evaluated without including MPPT loop in section 4.2.1. At this point, two separate light intensities are applied as the input of the solar panel. During this simulation the duty cycle is kept constant at the corresponding optimal value of each light intensity to study the efficiency of the circuit. The frequency and duty cycle are implemented with a square wave voltage source.

In section 4.2.2, the performance of MPPT algorithm is evaluated. The controller which was previously discussed in section 3.3 is integrated with the proposed micro converter. Once the MPPT control loop is implemented in PSIM, varying light intensity will be applied to the proposed micro converter to verify the MPPT performance. This is performed by feeding in the converters input voltage (V_{in}) and current (i_{in}) into the controller. The duty ratio, D is varied to allow the proposed converter to achieve MPP and maintain operating at this point. Subsequently, the square wave voltage source which was utilized to generate gate signal in section 4.3.2 has been removed; it is replaced with a C block which allows users to enter the C programming code and to define and custom code. The Modified MPPT algorithm described in Chapter 3 is entered into this C block and the code is also provided in Appendix. Output of C block is a raw value of optimal duty ratio which is further compared with a sawtooth waveform to provide the ideal gate control signal to switches.

The solar panel that is designed in PSIM is a physical mode solar module. To perform an accurate simulation, various technical parameters such as number of cells, voltage and current at maximum power, and the maximum power are required to be applied. These parameters are derived from a 210W Evergreen solar panel ES-A-210 -fa3* datasheet. These parameters are located in table 4-3. Once all technical parameters are inserted, the simulation software would design the voltage-power curve for the panel at several light intensities. Fig. 4-1 shows the solar module (Physical module) implemented in PSIM.

Table 4-3 Solar panel parameters

Parameter	Component Value
Model	ES-A-210 -fa3*
Number of cells	100
Cell type	Polycrystalline Silicon
Maximum power rating (P_{max})	210W
Standard light intensity	1000
Reference temperature	25
Open Circuit Voltage (V_{oc})	44.2 V
Short Circuit Current (I_{sc})	6A
Voltage at maximum power point (V_{mpp})	37.1V
Current at maximum power point (I_{mpp})	5.5A

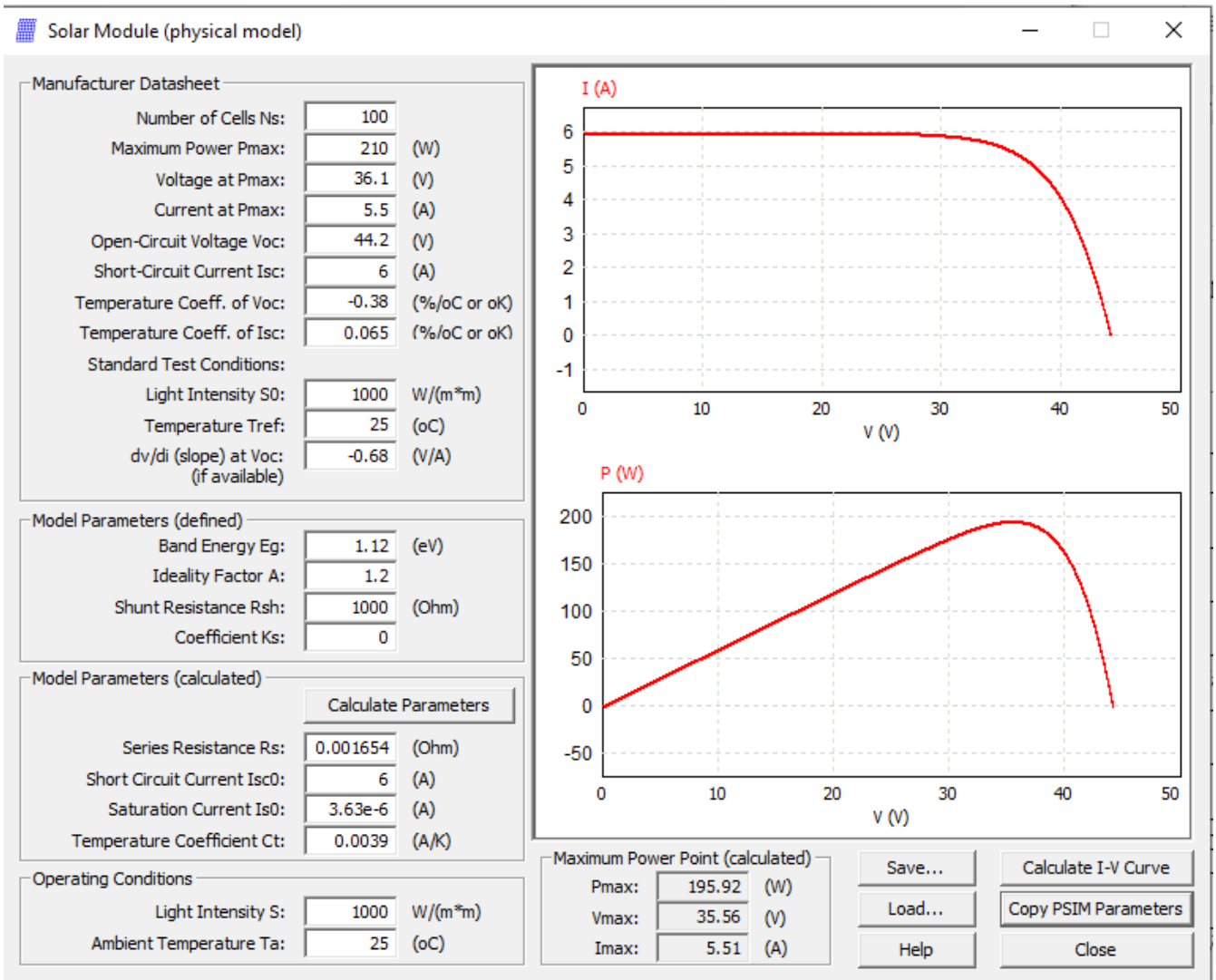


Fig. 4-1: PSIM Solar Module (physical model)

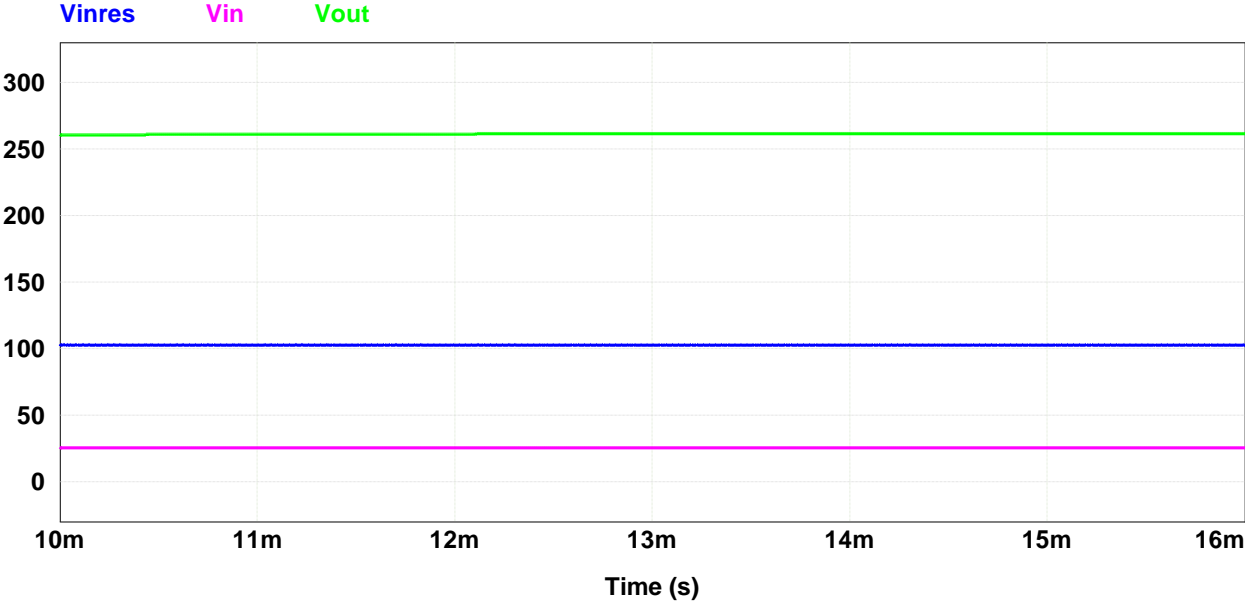
4.2.1 Results: Micro Converter, MPPT Controller Excluded

To test the functionality of the proposed micro converter at fixed light intensities, an input light intensity of 600 W/m^2 is applied for the first test. Switching frequency of the proposed DC/DC micro converter is fixed at 1.1 MHz and duty ratio D is set to 75% . The frequency is determined very close but slightly above resonant frequency so that switches can operate under zero voltage switching. Fig. 4-2 (a) illustrates the input voltage V_{in} and output voltage V_{out} of the micro converter along with the output voltage waveform V_{inres} of the integrated boost converter. Input voltage of the micro converter is shown in pink, whereas V_{out} is indicated in green and V_{inres} is illustrated in blue. As can be observed, the input voltage of 25 V is stepped up through the integrated boost converter to an average value of 102 V before it sees the APWM resonant tank. From here it can be seen that the whole circuit is able to step up the input voltage from 25 to 261 V at the output stage in the given condition.

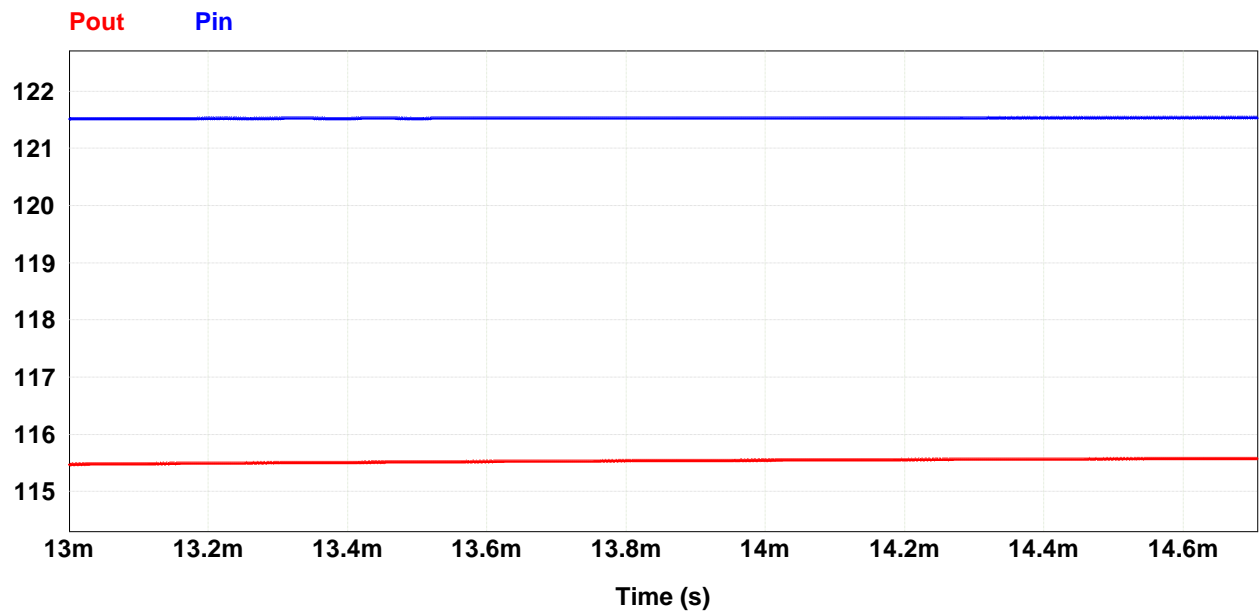
Output power of the micro converter P_{out} in red is compared with the input power P_{in} in blue in Fig. 4-2 (b). As can be seen, input power to the micro converter in this condition is almost 121 W . This power is transferred to the load where power value is at 115 W . By dividing output power over the input power, efficiency of circuit is calculated, which is greater than 96% .

The auxiliary inductor voltage V_{La} (green) and auxiliary inductor magnified current I_{La} (orange) are given in Fig. 4-2 (c). As can be seen, the inductor current is continuous, which verifies the CCM operation. Fig. 4-2 (d) illustrates the boost inductor voltage V_{Lin} (blue) and current $I_{inBoost}$ (red). Similar to auxiliary inductor, the boost inductor also proves the continuous conduction mode operation in this condition.

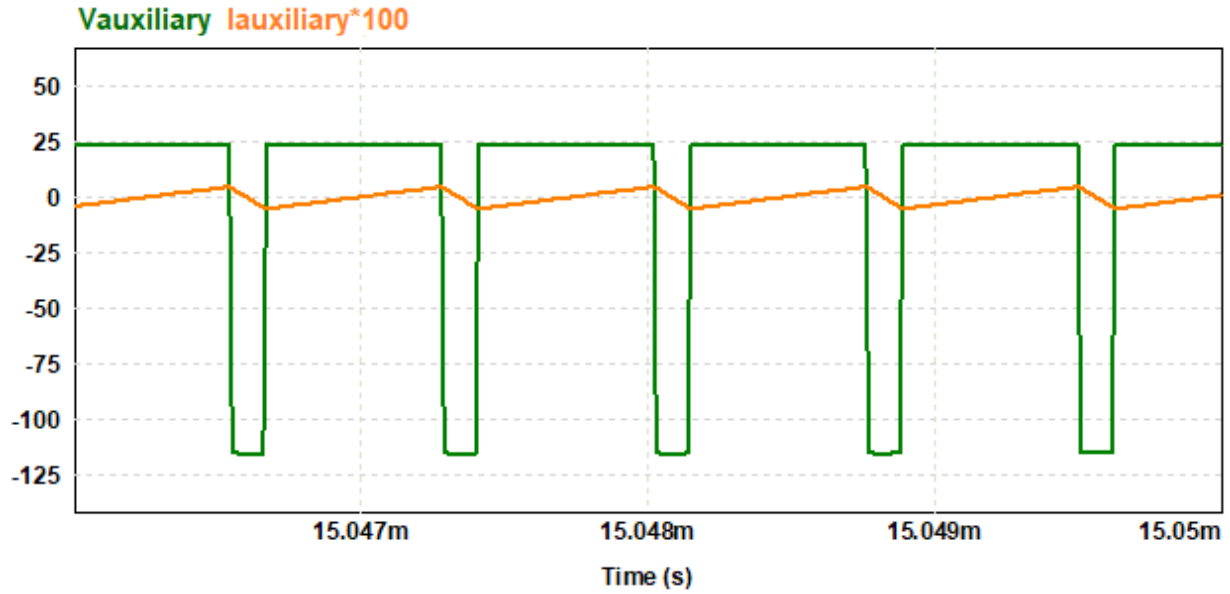
Fig. 4-2 (e) demonstrates voltage and current waveforms of switch 1; where Switch 1 voltage V_{ds1} is illustrated in blue and switch 1 current I_{S1} (multiplied by 10) is illustrated in green. As can be observed, this switch is achieving ZVS in the given condition. Switch 2 voltage and current are also given in Fig. 4-2 (f). Switch 2 voltage V_{ds2} is shown in blue where switch 2 current I_{S2} is illustrated in red color. Similar to S_1 , it is also obtained that S_2 is able to achieve ZVS in given condition.



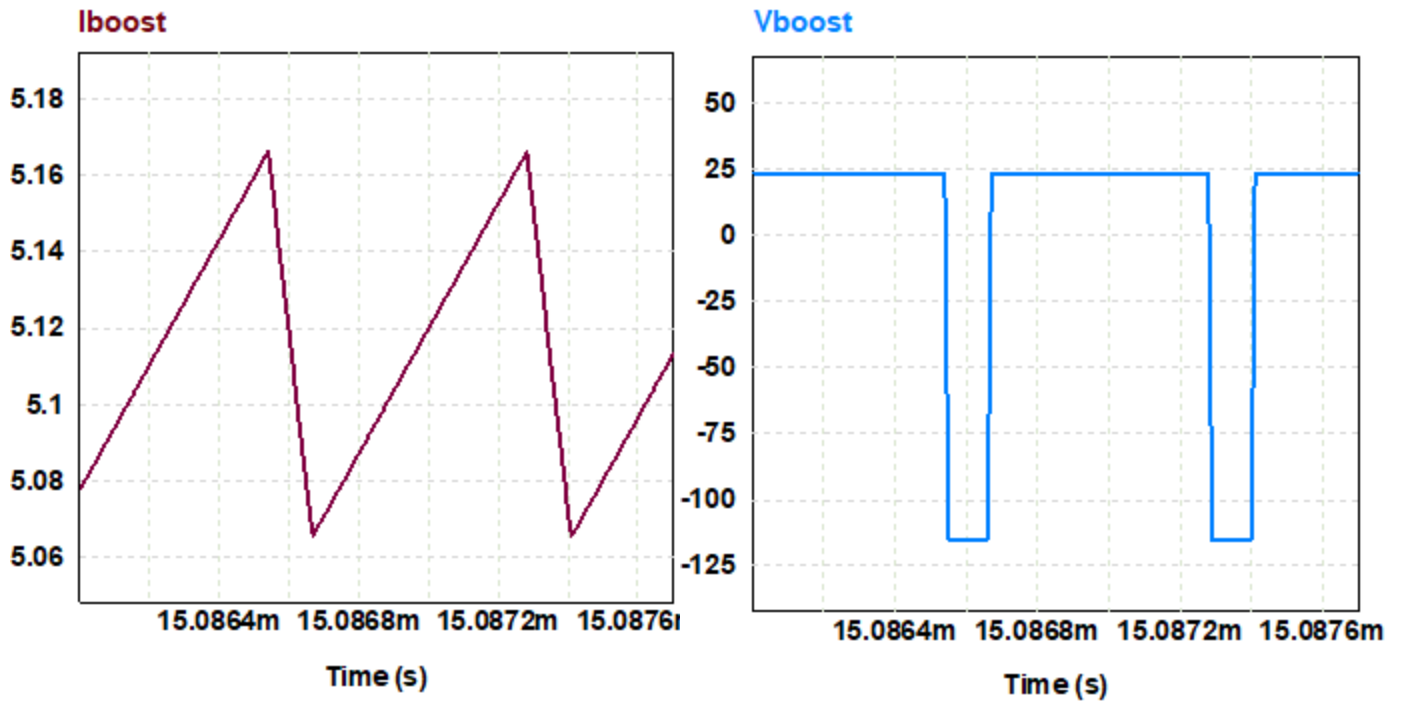
(a)



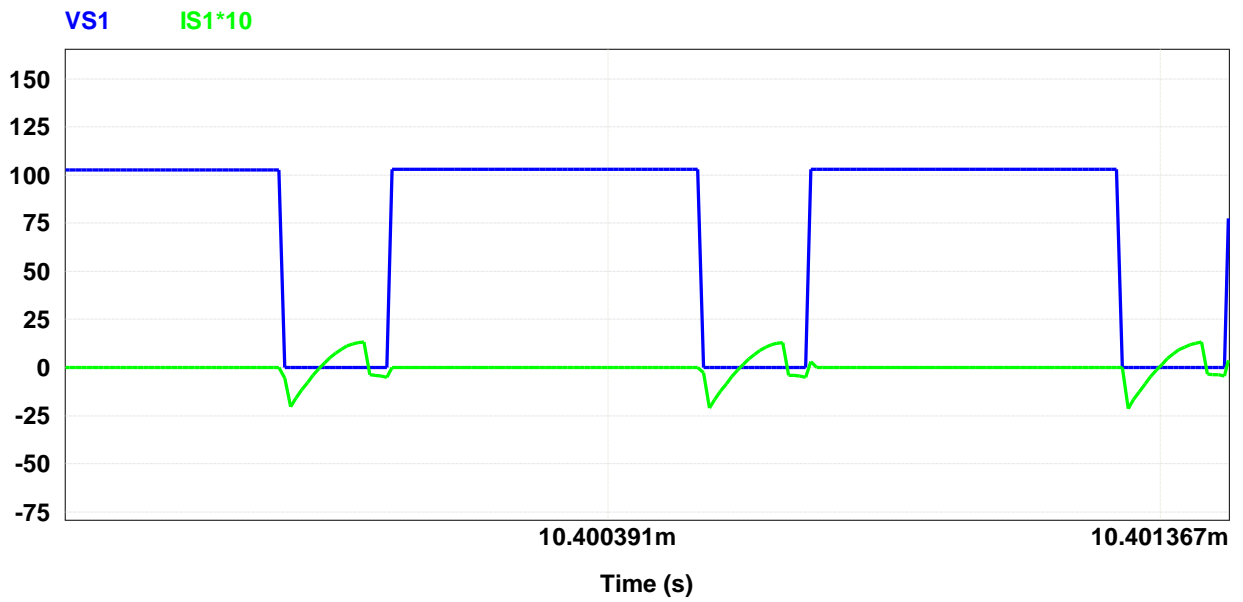
(b)



(c)



(d)



(e)

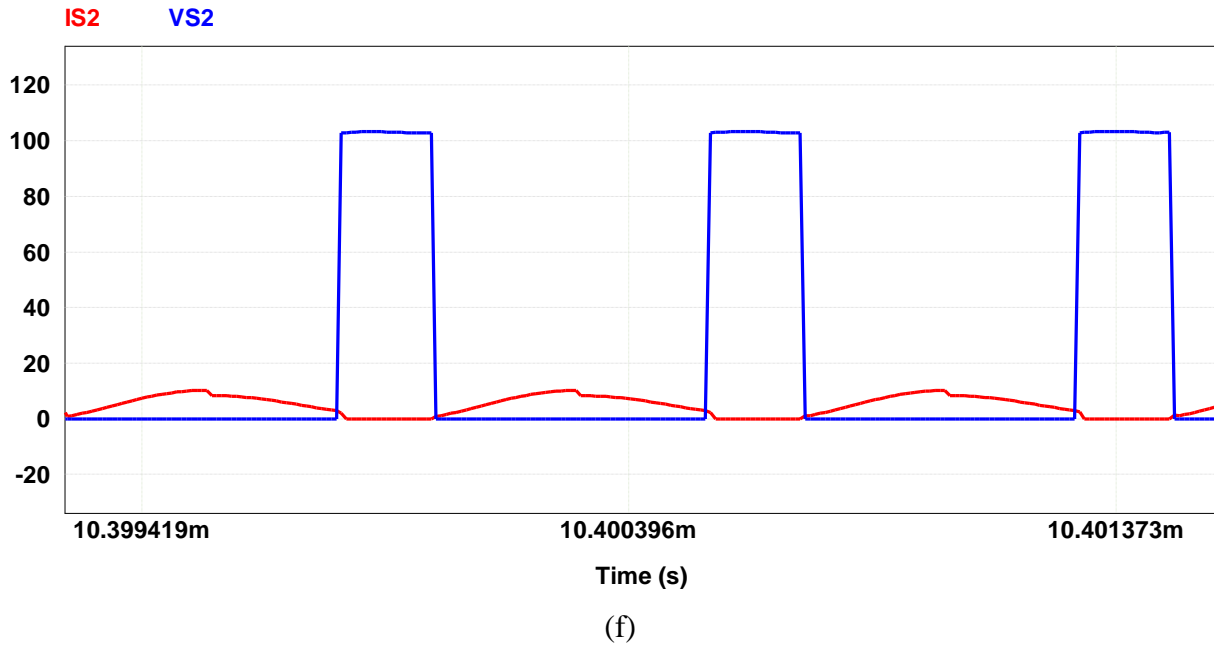


Fig. 4-2: PSIM waveforms of the proposed micro converter at light intensity of 600 W/m^2 with a switching frequency of 1.35 MHz and a duty ratio of 0.75 (a) input and output voltage of the micro converter along with output voltage of the integrated boost converter (b) Input and output power of the proposed micro converter (c) Auxiliary inductor voltage and current (d) Boost inductor voltage and current (e) Switch 1 voltage and current (f) Switch 2 voltage and current waveforms

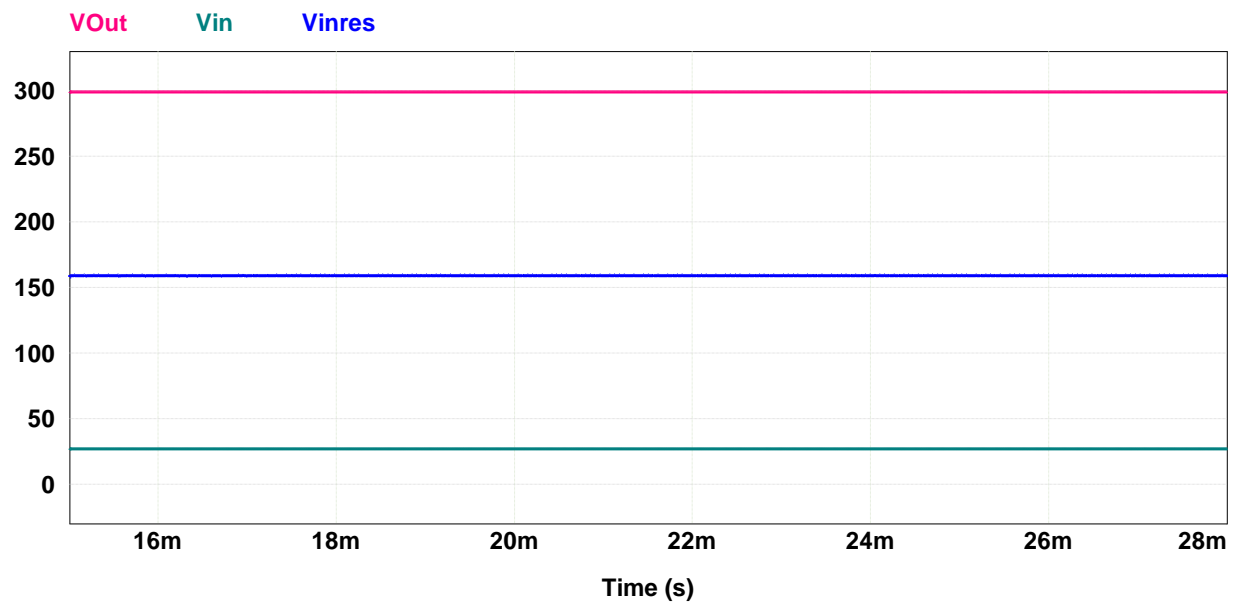
Thereafter, PSIM simulation is carried out one more time with a different light intensity equal to 800 W/m^2 . This new condition is applied as the input of the solar panel. Switching frequency is kept fixed and the same as previous test stage at 1.1 MHz . This frequency is set such that switches can operate under zero voltage switching. The corresponding optimal duty ratio at the new light intensity is set as 83% . Fig. 4-3 (a) gives input voltage V_{in} and output voltage V_{out} waveforms of the proposed DC/DC micro converter. In addition, Fig. 4-3 (a) illustrates the output voltage V_{inres} of the integrated boost converter at the given condition. Input voltage is shown in green and output voltage is indicated in pink; where the output voltage of the boost converter is depicted in blue. As can be observed, the V_{in} equal to 28 V is initially stepped up through the integrated boost converter

to an average value of 159 V before it applies to the APWM parallel resonant tank. In addition, it is observed that the circuit is able to step up input voltage from 28 to just above 299 V at the given condition.

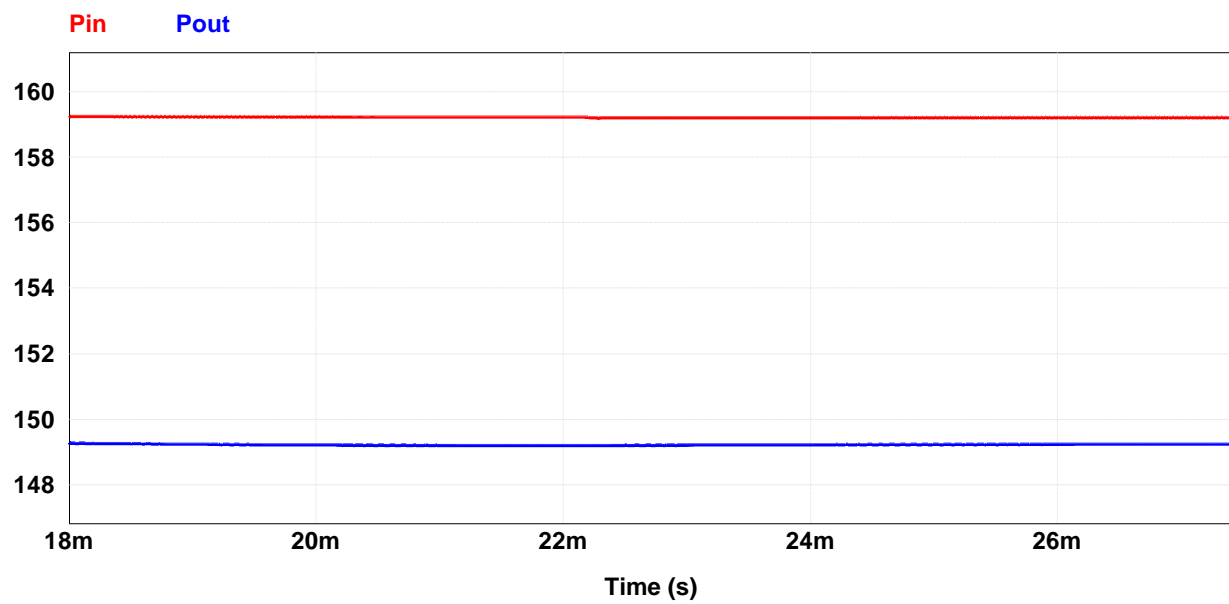
Fig 4-3 (b) shows the output power P_{out} of the micro converter in blue and the instantaneous input power P_{in} in red. As can be observed, the input power to the circuit at this condition hits 158 W. This power is transferred to the resistive load where almost 150.5 W is delivered. The efficiency of the proposed micro converter is calculated and it hits greater than 95% in this scenario.

Auxiliary inductor voltage V_{La} in blue and auxiliary inductor magnified current I_{La} in green are depicted in Fig. 4-3 (c). As auxiliary inductor current is flowing continuously without reaching zero values, operation in CCM is confirmed. Fig. 4-3 (d) illustrates the boost inductor voltage V_{Lin} and $I_{inBoost}$, with blue and red color respectively. Both current waveforms display continuous conduction mode operation at this light intensity.

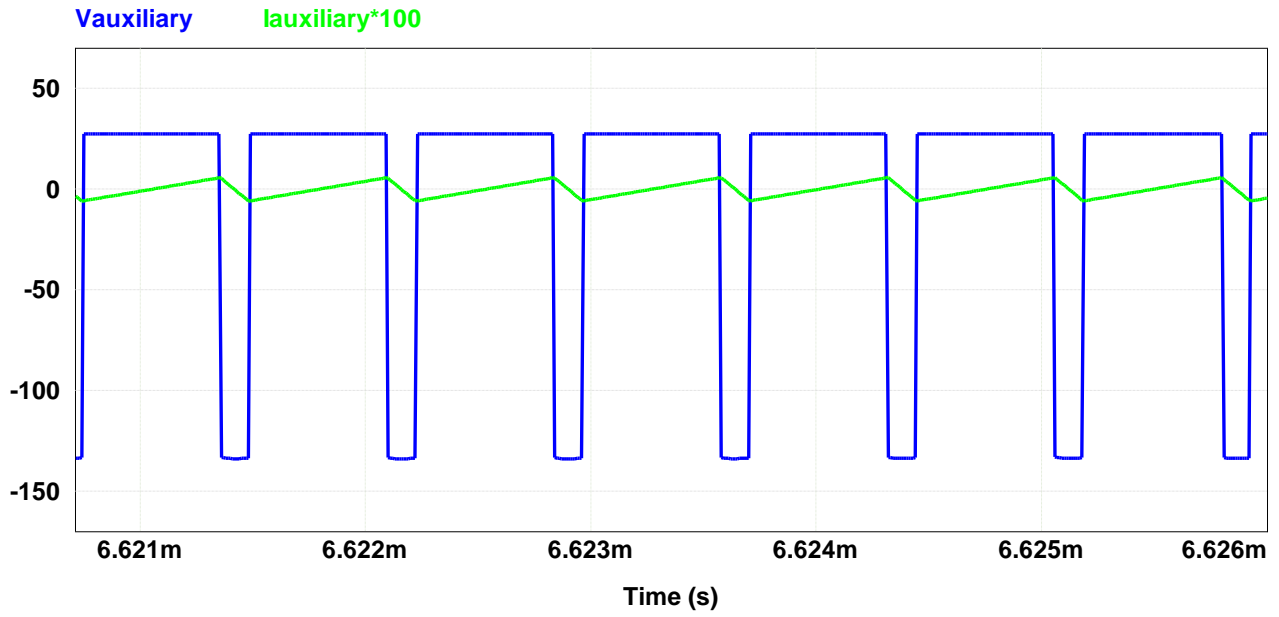
In Fig. 4-3 (e) switch 1 voltage V_{ds1} is illustrated in red where a magnified value of switch 1 current $10 * I_{S1}$ is illustrated in blue color. As can be observed, this switch is achieving ZVS in the given condition. Switch 2 voltage and current are given in Fig 4-3 (f). Voltage V_{ds2} is shown in red where a waveform of switch 2 current I_{S2} is illustrated in green. It is verified that S_2 is also able to achieve ZVS in the given condition.



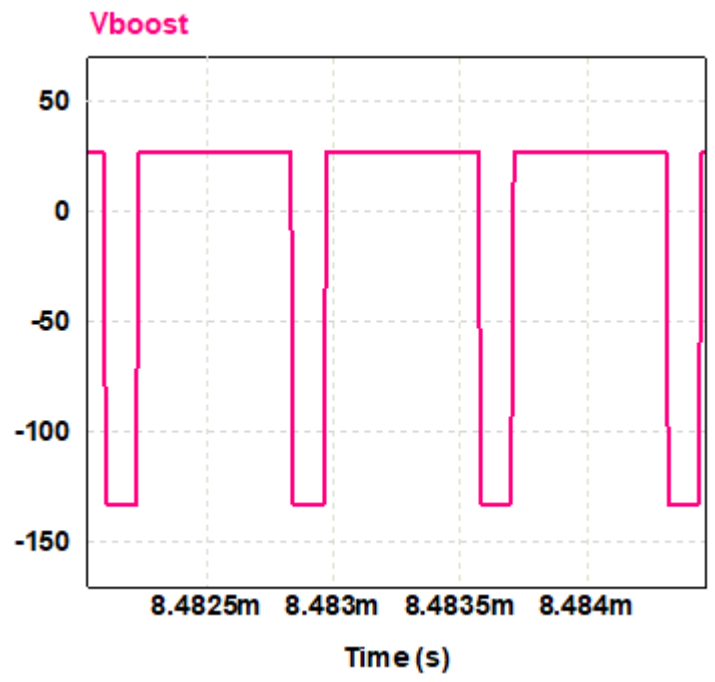
(a)



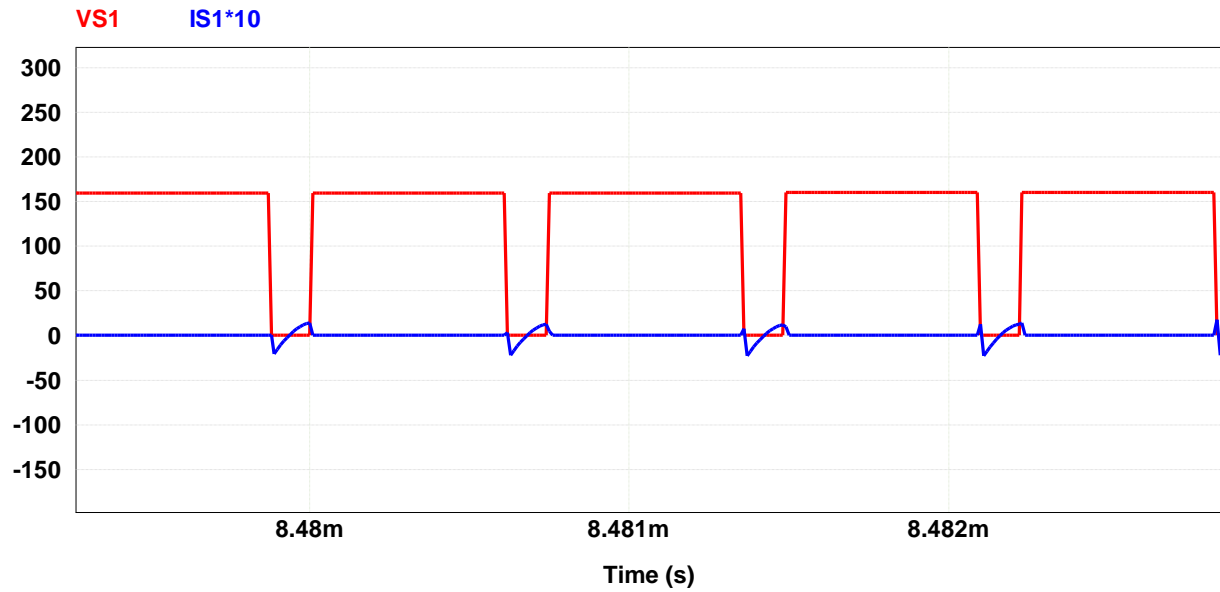
(b)



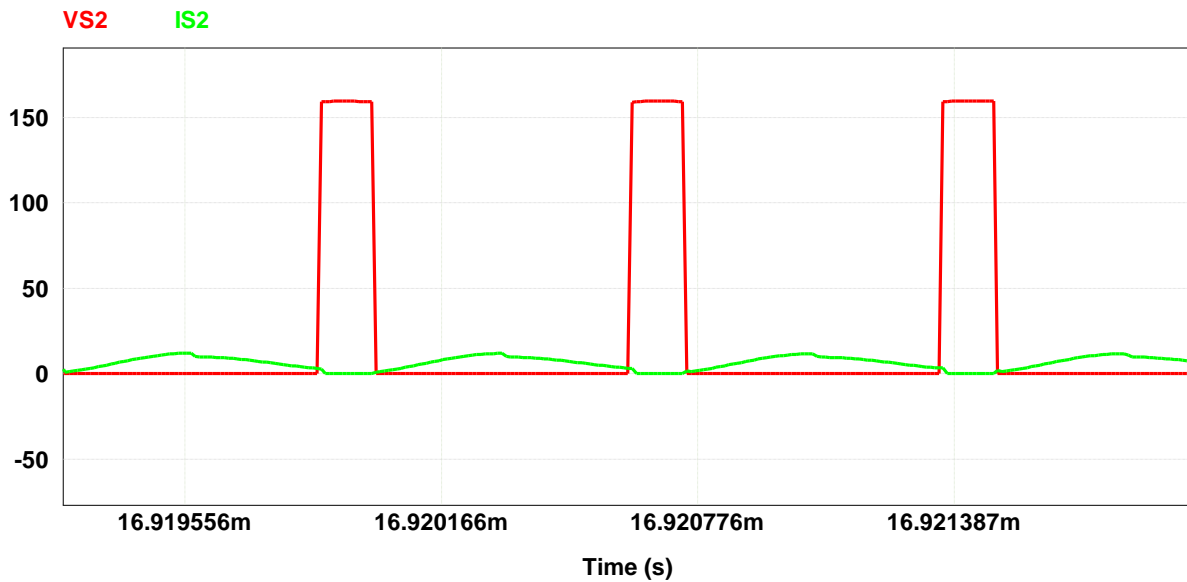
(c)



(d)



(e)



(f)

Fig. 4-3: PSIM waveforms of the proposed micro converter at light intensity of 800 W/m^2 with a switching frequency of 1.35 MHz and a duty ratio of 0.83 (a) input and output voltage of the micro converter along with output voltage of the integrated boost converter (b) Input and output power of the proposed micro converter (c) Auxiliary inductor voltage and current waveforms (d) Boost inductor voltage and current waveforms (e) Switch 1 voltage and current (f) Switch 2 voltage and current waveforms

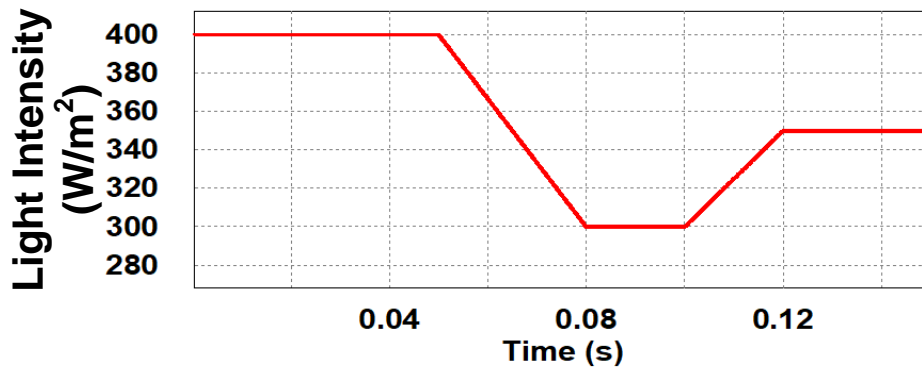
4.2.2 Results: Micro Converter, MPPT Operation

The previous simulation was carried out based on a constant optimal duty cycle value and a fixed near- to- resonant switching frequency. In the previous simulation, the circuit was not controlled to achieve the maximum power operating point. In this section, PSIM simulation results are provided on the same DC/DC micro converter which is controlled by an MPPT controller. Input current (i_{in}) and voltage (v_{in}) of the micro converter along with an initial value for duty cycle and its perturbation are fed to the MPPT controller as the input. The output of MPPT controller is a constant duty ratio value which will be further compared with a sawtooth waveform to generate an optimal switch control parameter with a desired duty cycle value. From this point, the duty ratio of the converter is no longer constant and it follows the direction of dP/dD to reach the ideal power value. Therefore, the square wave voltage that generated the switch signal is removed from PSIM. Instead, a C code block is implemented that contains the control algorithm of the modified MPPT discussed in Chapter 3.

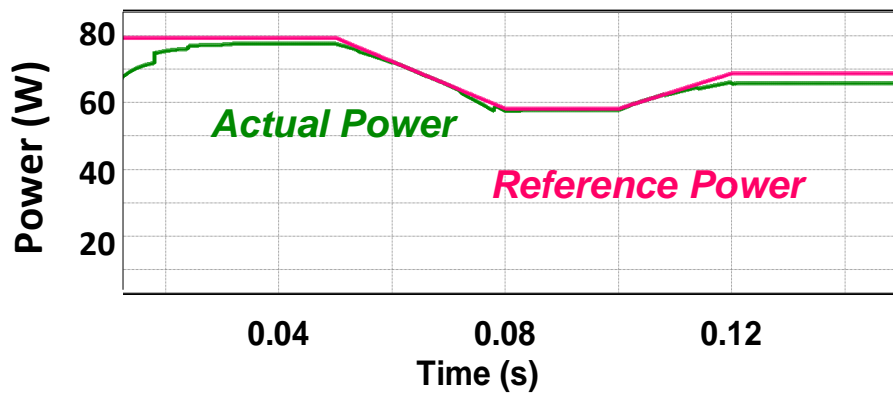
A piecewise linear voltage source is selected to further alternate the light intensity of the solar panel in multiple time frames. To achieve optimal power point, the MPPT controller previously discussed in Chapter 3 is now integrated with the proposed micro converter. In order to test various atmospheric conditions, the light intensity of the solar panel which is generated by the piecewise linear voltage source is varied. As was discussed in section 1-5, when the light intensity changes, the optimal value for duty ratio also change.

Fig. 4-4 displays the simulation results of various parameters in the proposed micro converter at a varying light intensity condition. The light intensity input is represented in Fig. 4-4 (a) in red. Fig 4-4 (b) shows the actual output power of the solar panel in green in compared with its reference

value in red. From here, it can be observed that the MPPT controller is successfully tracking the optimal power point and it maintains performing at it when the light intensity changes. It also shows that it approximately 20 milli seconds (ms) for the controller to achieve optimal duty ratio value and obtain maximum power operating point. It is verified that MPPT controller can rapidly track desirable operating point while a circuit efficiency above 95% is maintained for various light intensities.



(a)



(b)

Fig. 4-4: (a) Light intensity of the solar panel in PSIM (b) Actual input power of the solar panel in compared to the reference maximum power

Fig. 4-5 (a) provides the drain- source voltage of switch 1 V_{ds1} in blue where Fig 4-5 (b) gives switch 1 current I_{s1} in red. Zoomed-in waveforms of both graphs are provided in Fig 4-5 (c-d). As can be seen, the overlap interval in both selected areas is almost zero, hence soft- switching operation of Switch S_1 is verified.

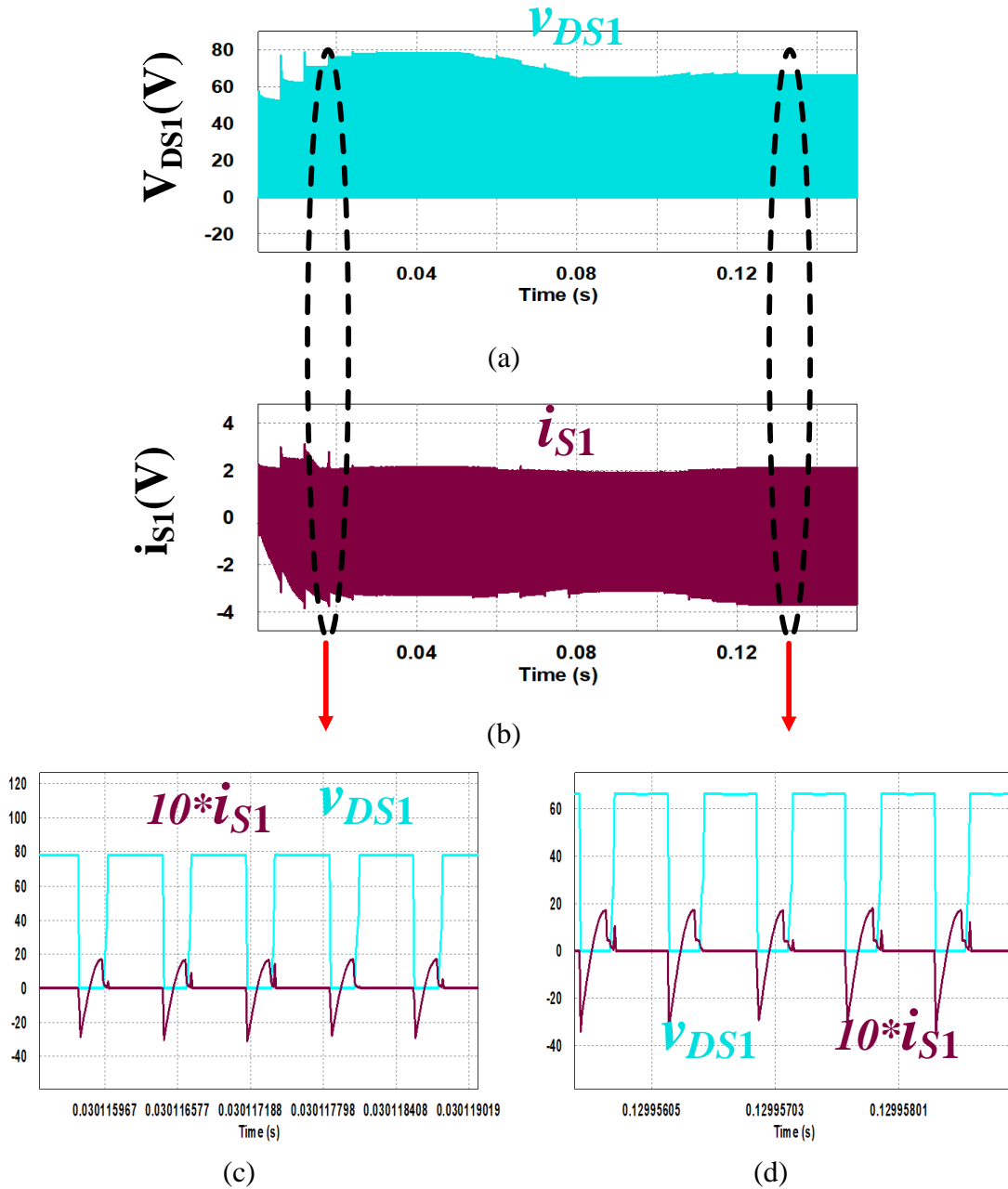


Fig. 4-5: (a) Switch 1 voltage waveform at various light intensities (b) Switch 1 current waveform (c), (d) Enlarged voltage and current waveform at the selected time intervals

Fig. 4-6 (a) provides the drain- source voltage of switch 2 V_{ds2} in blue and Fig. 4-6 (b) gives switch 2 current waveform I_{s2} in orange. Zoomed-in waveforms of both graphs are illustrated in Fig. 4-6 (c)- (d). As can be realized, the overlap interval in all selected areas is zero. Therefore, Switch S_2 turns on with ZVS.

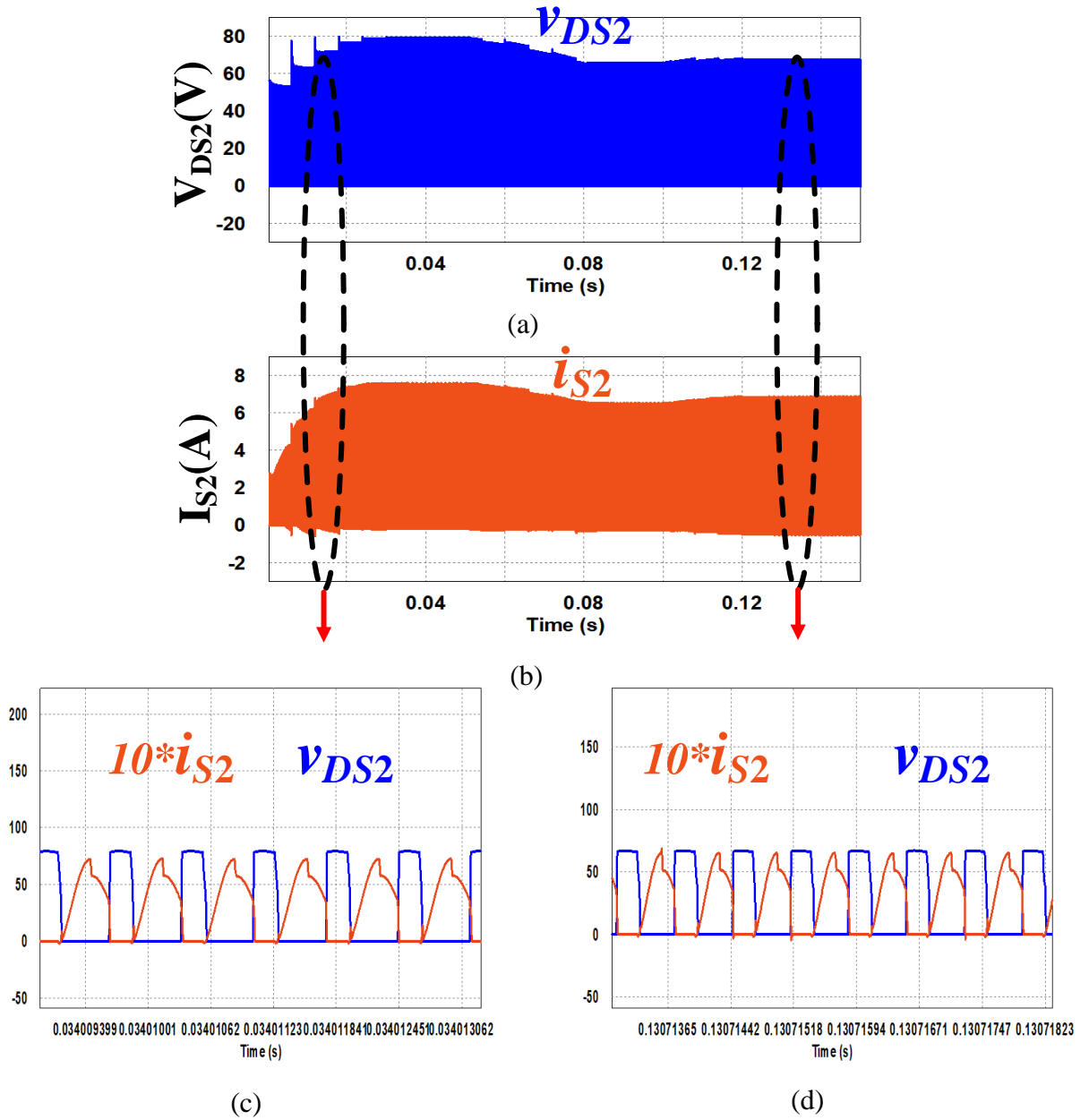


Fig. 4-6: (a) Switch 2 voltage waveform at various light intensities (b) Switch 2 current waveform (c), (d) Enlarged voltage and current waveform at the selected time intervals

4.3 Hardware Experiment Testing

In this section, experimental test is carried out to verify the performance of the proposed DC/DC micro converter. The circuit parameters and components are selected based on the proposed micro converter without the high- frequency transformer (see Fig. 2-10). To briefly summarize, in resonant circuit $C_s= 1.7$ nF, $L_m=16$ μ H and coupled inductor $L=22$ μ H is a shielded inductor (MSD1583). Boost parallel capacitors $C_1, C_2= 3.3$ μ F are KEMET surface mount multilayer ceramic chip capacitor. To operate at high frequency range, IRL510PBF MOSFET switch manufactured by Vishay Siliconix is used. All diodes are hyper-fast recovery diodes (RHRP15120). These components are given in Table 4-4. A printed circuit board (PCB) of the proposed MHz micro converter is designed using electrical design software Altium- Designer. When schematics of the micro converter is sketched, the footprint of each component is also added to the library of the PCB project based on each component's footprint provided in their datasheets. Width of the traces was adjusted based on the rated current flowing through each component. The layout of the PCB is given in appendix.

Table 4-4 Experimental Circuit Component Parameters

Parameter	Component Value
Input Capacitor C_{in}	10 μ F
Output Capacitor C_o	10 μ F
Output Inductor L_o	330 μ H
Resonant Capacitor C_s	1.7 nF
Resonant Inductor L_m	16 μ H
Boost Inductor L_{in} (Primary winding of the coupled inductor)	22 μ H
Auxiliary inductor L_a (Secondary winding of the coupled inductor)	22 μ H
Boost parallel capacitors C_1, C_2	3.3 μ F
Near o resonance operating frequency	1.03 MHz
Duty cycle	0.6
Load	600 Ω

Half-bridge gate driver employed in the topology is LM5113-Q1 that can operate up to several MHz frequency. This gate driver is designed to drive low and high side mode silicon MOSFET or Gallium Nitride FET in a boost, buck or half- bridge configuration. A simplified diagram of the application is given in Fig. 4-7.

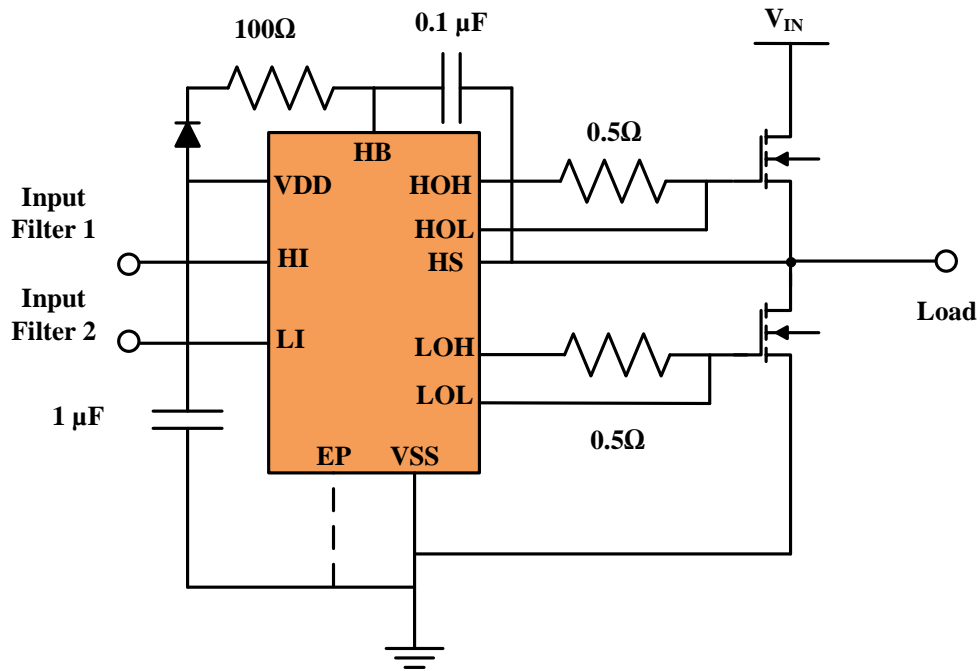


Fig 4-7: Micro converter gate driver application diagram obtained from LM5113-Q1 datasheet

To begin the experimental test, first control circuit components including the gate driver and switches are soldered on the PCB logic unit. The Digital Signal Processing (DSP) device that is used in the experimental procedure is Texas Instrument Evaluation Board with part number TMS320F28335 that operate up to 150 MHz frequency. This evaluation board can generate a gate signal with an average value of 3V supply voltage. The output of DSP is connected to the input of gate driver and is further increased to a higher voltage around 4.5 V to match the gate signal of circuit switches. Once the logic unit is powered, the frequency of micro converter switches is gradually increased to make sure that the system can operate within MHz switching frequency.

Fig. 4-8 gives the first Oscilloscope graphs illustrating the gate signal waveforms of switch 1 and 2 at 1.01 MHz which verifies the control unit ideal performance.

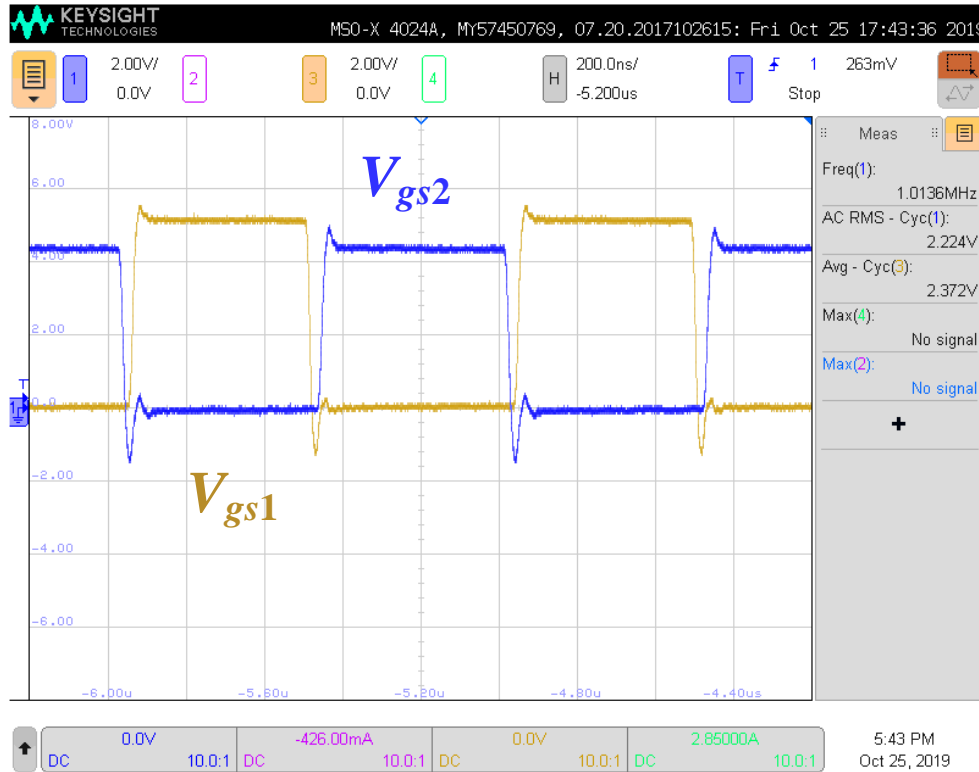


Fig. 4-8: Micro converter switch gate signal when the logic unit is powered at 1.01 MHz frequency

To verify the desirable functionality of the proposed micro converter, all components including coupled inductor are soldered on the PCB board and a resistive load of $600\ \Omega$ is connected directly to the output of the converter prototype. Once ZVS is observed, the frequency is kept constant which is about 1.04 MHz. At this stage, duty cycle can be varied to capture several voltage gain values if required. Fig. 4-9 shows certain values of the proposed micro converter at $V_{in}=30\ \text{V}$ and $D=0.6$ which verifies the ZVS and near ZCS operation. This figure shows switch 2 voltage (v_{s2})

and current (i_{s2}) waveforms along with boost inductor current ($i_{inboost}$) at this operating condition. Switch 2 voltage waveform v_{s2} is illustrated in blue, i_{s2} is in green and $i_{inboost}$ is given in gold.

From Fig 4-9 it can be seen that switch 2 current has a value at 1.67A, where its drain- source voltage has an average value of 100 V. It is observed that soft- switching is achieved and boost inductor current also confirms CCM operation with a maximum value at 0.54 A.



Fig. 4-9: Switch S_2 waveforms and boost inductor current

In next experimental stage, an input voltage of $V_{in}=25V$ is applied to the PCB and a duty ratio equal to 0.6 is set in DSP as the duty cycle of the switches. Frequency is kept fixed at 1.04 MHz. Fig. 4-10 is obtained at the given condition which illustrates both switch current waveforms, along with load voltage V_o and the resonant inductor voltage V_{Lm} waveforms. From Fig 4-10, it can be

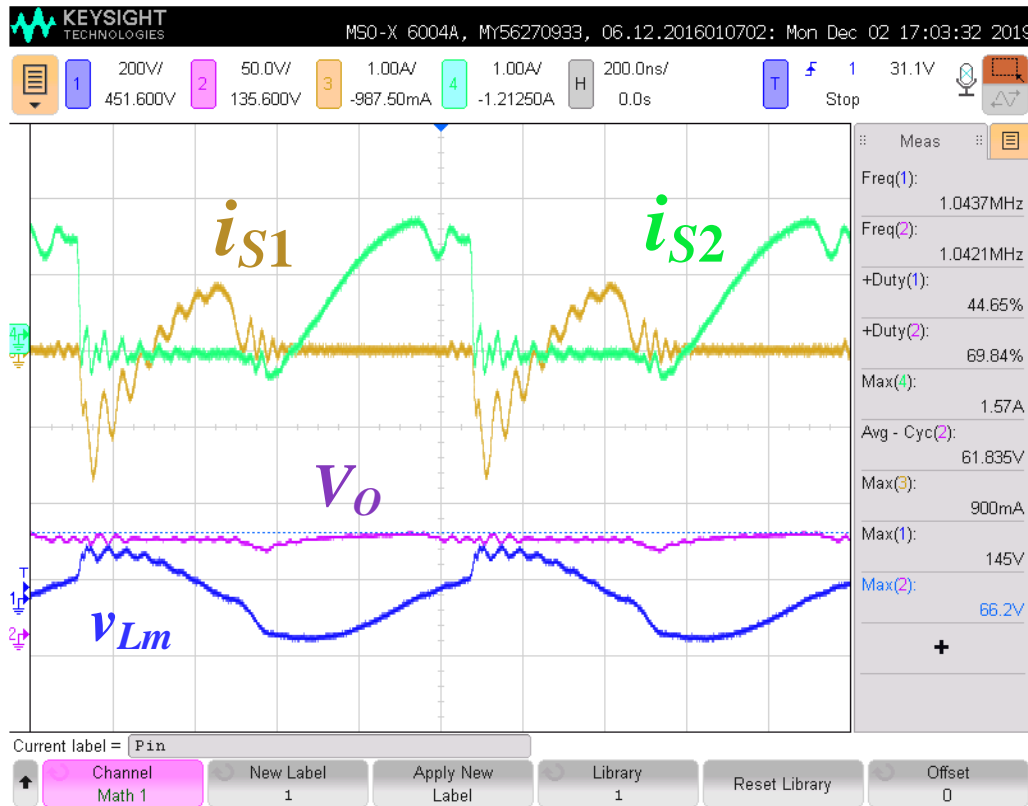


Fig. 4-10: Resonant Inductor and load voltage waveform and circuit

seen that i_{s2} has a maximum value of 1.57A where i_{s1} maximum current shows 0.9A; i_{s2} is demonstrated in green and i_{s1} is in gold. The input voltage is stepped up to an average output voltage V_o equals to 62 V at the given condition; where V_o is illustrated in blue. To verify the functionality of the diodes on PCB, resonant inductor voltage V_{Lm} is also measured and is shown

in blue. As expected, V_{in} is a sinusoidal waveform in blue with a maximum peak value at 140 V. Lossless operation of switches is once again verified additionally.

Lastly, to capture DC-link voltage waveform, an input voltage of $V_{in}=31V$ is applied to the micro converter with a duty ratio set at 0.6. Fig. 4-11 is obtained at given condition which provides C_1 voltage waveform, along with switch current waveforms. It can be seen that i_{s2} has a maximum value of 3.55 A and i_{s1} maximum current shows 1.97A; which are illustrated in gold and green respectively. As C_1 and C_2 have equal voltage values, DC-link voltage equals two times the V_{C1} which is around 85V. Hence, the input voltage is increased approximately 2.5 times though the integrated boost converter before it sees APWM resonant circuit.

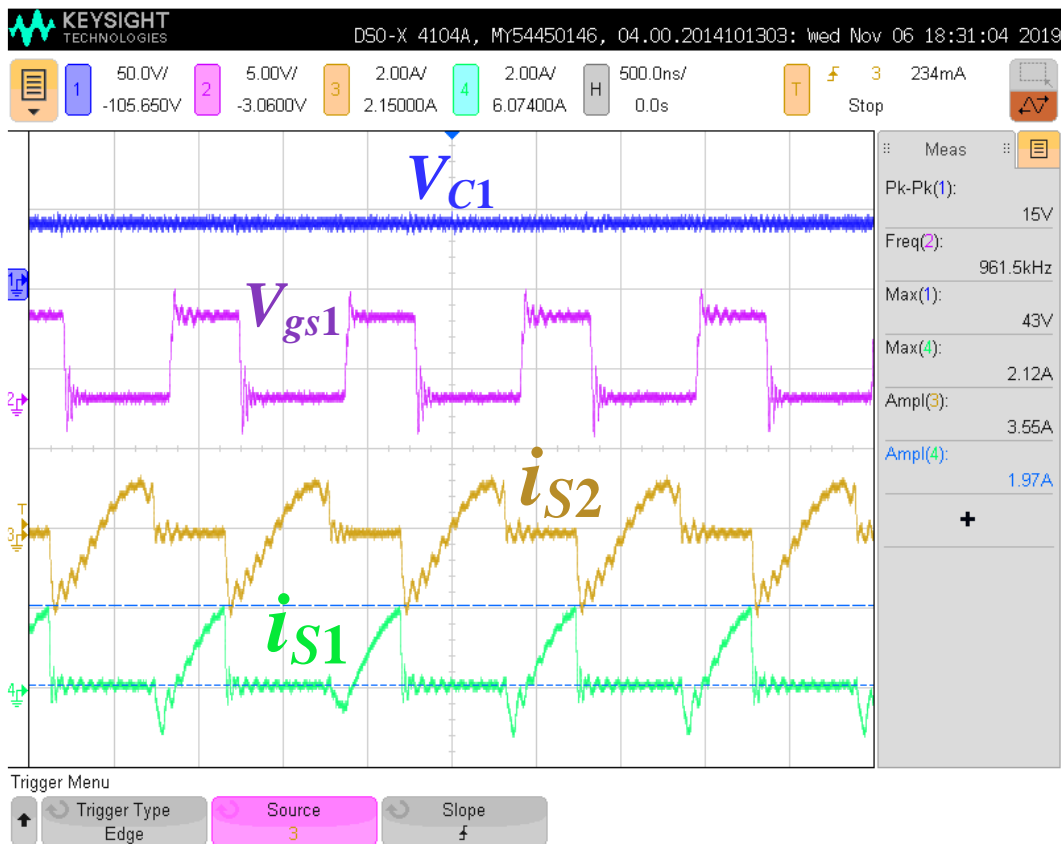


Fig. 4-11: Voltage waveform of boost converter capacitor C_1 and switch current waveforms

4.4 Analysis

Table 4-5 shows the summary of performance comparison among several different PV converters including the proposed circuit. The required number of components of each converter, values of inductors and capacitors, peak voltage stress over switches, voltage stress over diode, switching type, operating switching frequency, use of coupled inductor and total converter efficiency are compared in this table. It can be seen that [21] and [29] have almost the same range of component value, similar voltage stress over switch and diodes; however, [29] can achieve higher voltage gain. In [33] a coupled inductor is implemented in a hybrid boost-flyback converter which can avoid extreme duty cycle and also eliminates the number of passive elements. Compared to [21] and [29], the switch and diode voltage stress is reduced to almost half of the output voltage, depending on the turns- ratio of the coupled inductor. The converter in [35] consists of a single switch topology which utilizes the least number of switch elements and it is only suitable for low output power levels. Despite the low number of components, all aforementioned topologies suffer from hard- switching operation and they are only suitable for operation up to 100 kHz. Even though ZVS performance has also achieved in basic circuits of [21], [27], [29] and [33] through the use of additional auxiliary circuit, yet higher number of components and poor efficiency could not be mitigated in those realizations. To achieve soft-switching operations, [40] and [41] have been presented. The converter in [40] has achieved high efficiency through the use of small value components. However, the input current is discontinuous which requires a larger input capacitor. Although a lower voltage stress is applied to the circuit components, the converter has higher costs as voltage step-up is mostly realized through the use of high turns- ratio transformer. To increase frequency, [41] is presented which is a 1MHz soft- switching topology with a fairly high efficiency. This circuit utilizes a high number of semiconductor elements; resulting is high cost

system. In addition, input current is also in DCM which requires a large input capacitor. This thesis has presented a DC/DC micro converter which has significantly lower- rated and lower- cost components. Besides, this circuit can realize soft- switching operation for all switches in a large duty cycle range. It also owns a varying voltage gain depending on the application. A coupled inductor is employed which has reduced the number of magnetics of the circuit. The size of micro converter is relatively smaller than the reviewed topologies which makes it an attractive interface in industry with maximized harnessed efficiency. MPPT control system is also integrated with the proposed configuration when efficiency was found to be higher than 95% at various light intensities. This was determined by dividing the micro converter output power by its input power.

Table 4-5: Comparison of various step-up DC/DC Converters for PV energy applications

Converter		[21]	[29]	[33]	[35]	[40]	[41]	Proposed Micro Converter
Components	Switch	2	2	1	1	2	6	2
	Diode	2	2	2	2	2	4	2
	Capacitor	2	3	3	4	4	4	5
	Inductor	2	2	1	2	2	2	3
Operating Frequency		50kHz	50kHz	100kHz	100kHz	100kHz	1MHz	1MHz
Switching Type		Hard	Hard	Hard	Hard	Soft	Soft	Soft
Coupled Inductor		Optional	No	Yes	No	No	No	Yes
Peak Switch Voltage stress		V_o	V_o	$\frac{V_o}{1+a.D}$	$\frac{V_o}{1+D}$	$\frac{V_o}{NM}$	$\frac{V_o}{2}$	$\frac{V_o}{NM}$
Peak Output Diode Voltage		V_o	V_o	$\frac{V_o}{1+a.D}$	$\frac{V_o}{2}$	$\frac{V_o}{2}$	V_o	V_o
CCM operation of Input current without input capacitance		Yes	Yes	Yes	Yes	No	No	Yes
Efficiency		88%	85%	90%	86%	95.4%	95.5%	95%

N is the high- frequency transformer turns- ratio

a is turns- ratio of the coupled inductor

M is the gain of resonant tank

4.5 Summary

This chapter presented the simulation and experimental results of the proposed DC/DC micro converter. Simulation was carried out using PSIM software and the results is provided at different light intensities to confirm soft-switching and input CCM operations of the proposed circuit. The simulation was also done at varying light intensities with MPPT control loop included to verify the operation of MPPT system. A proof of concept prototype was designed, built and tested with several input voltages to show the merits of the proposed system. Both simulation and experimental results have confirmed that the circuit is able to achieve soft-switching operation and that it can also operate in CCM condition.

5. Summary and Conclusion

5.1 Summary

The combined global capacity of renewable energy sources has considerably increased over the past decade. Among all, PV energy has experienced a rapid growth in installed capacity which is expected to continue to increase in the near future. Since the typical PV panel output is relatively low, in order to convert panel voltage level into grid- matching voltage level and in order to extract the maximal amount of solar energy, DC/DC power electronic converters are required. These DC/DC converters can be implemented together with an MPPT control system to achieve optimal power at various sunlight intensity conditions.

Existing PV DC/DC converters, however, suffer from one or more of the following drawbacks:

1. Hard- switching operation which results in lower efficiency and higher power loss
2. Operation in discontinuous conduction mode which results in higher ripple in the input current and hence, large input filtering capacitance is required
3. Soft- switching is restricted to a limited operation range as the converter fails to achieve soft-switching at certain operating conditions
4. Utilizing a high number of magnetic components which deteriorates the circuit efficiency and increases the overall cost of the system
5. Experiencing high voltage stress over circuit elements; which results in high- cost and high- voltage- rating components

This thesis has presented a DC/DC micro- converter, which operates within Mega-Hertz frequency, and is able to step- up PV panel output voltage while maintaining CCM and soft-switching operation in an extended range of duty ratio and loading conditions. A modified MPPT control algorithm has also been designed to allow the devised PV micro converter to rapidly track the maximum power point when the sunlight intensity varies.

5.2 Contributions

The summarized contributions of this thesis have been presented below

1. Unlike the conventional boost converter, the proposed topology is able to achieve soft switching for all switches over an extended range of duty cycle and loading condition
2. Instead of using two separate inductors as the input inductor and the auxiliary inductor, a coupled inductor is employed. Accordingly, the magnetic components are reduced which may enhance the efficiency and reliability of the whole system. In addition, the primary winding of coupled inductor helps with filtering the input current waveform for high ripples in compared to soft- switching converters.
3. The proposed DC/DC converter is able to operate within MHz frequency while maintaining soft- switching operation. Hence, the overall converter size can be significantly reduced.
4. In compared to conventional boost converter, the voltage stress over switches is noticeably decreased. Thus, switches with low voltage rating and low cost can be utilized.
5. A modified variable-step MPPT algorithm has been designed to work with the proposed micro converter. The MPPT controller has shown to extract maximal amount of solar energy from the PV panel accurately with a fast response time at varying light intensities.

6. Both input boost inductor and the auxiliary inductor operate in continuous conduction mode. This alleviated the ripples and extends lifespan of the overall system.
7. Theoretical analysis of the proposed micro converter and the circuit main operating stages have been explained and provided in details.
8. The functionality of the proposed micro converter has been verified through simulation results obtained from PSIM software, as well as hardware experimental results obtained from a proof-of-concept hardware prototype.

5.3 Future work

Some of the future works associated to this thesis research are described below.

1. Replacement of Through Hole components with Surface Mount Device (SMD).

Since the proposed circuit is targeted at very high frequency operation, unwanted voltage or current oscillations were observed from the hardware results. To reduce the oscillation observed in some of the switching waveforms provided in section 4.4, most of the through hole components can be replaced with SMD counterparts. In particular, switches can be replaced with the recent technology advancement in semiconductor devices, such as Gallium Nitride (GaN) surface mount switch. The GaN switch available on the market also has very low turn-on resistance, which will be very beneficial to help reducing the conduction power loss in the switches.

2. Implementation of MPPT control unit in experimental work

In Chapter 3, the modified MPPT algorithm was introduced and the control loop was implemented and tested in simulation software PSIM. To highlight the merits of the

proposed micro converter, the developed control algorithm can be tested experimentally where the micro converter will be connected to a solar emulator which provides varying atmospheric conditions.

5.4 Conclusions

In conclusion, a MHz, step-up micro converter with extended soft- switching operation and CCM input using coupled magnetics has been presented for PV energy systems. Through the use of coupled inductor, the proposed micro converter is able to achieve soft- switching over an extended range of duty ratio or loading condition while at the same time, provide continuous input current with minimal number of magnetic components needed. As a result, very high frequency operation in the range of MHz is utilized in the proposed topology so that the physical sizes of the required passive components are reduced. Finally, PSIM simulation and experimental results have been presented to verify the performance of the proposed topology.

6. Bibliography

- [1] Renewable energy policy network (2018). *REN “2018 Highlights” report*. Retrieved from:
<http://www.ren21.net/status-of-renewables/global-status-report>
- [2] Annual Global Carbon Emissions report. Retrieved from:
https://www.greencarreports.com/news/1120348_report-global-co2-emissions-at-record-levels-in-2018
- [3] Global Carbon Project. Retrieved from: <https://www.wri.org/blog/2018/12/new-global-co2-emissions-numbers-are-they-re-not-good>
- [4] World Economic Forum. Retrieved from : <https://www.weforum.org/agenda/2019/06/chart-of-the-day-these-countries-create-most-of-the-world-s-co2-emissions/>
- [5] Each countries share of CO₂ emission. Retrieved from: <https://www.ucsusa.org/global-warming/science-and-impacts/science/each-countrys-share-of-co2.html>
- [6] Ecotricity (2017). The end of fossil fuels Retrieved from: <https://www.ecotricity.co.uk/our-green-energy/energy-independence/the-end-of-fossil-fuels>
- [7] REN “2018 Global Status” report. Retrieved from: <http://www.ren21.net/gsr-2018/>
- [8] National Resource Canada (2018). *Canadian Renewable Energy*. Retrieved from:
<https://www.nrcan.gc.ca/energy/facts/renewable-energy/20069>
- [9] Canadian Nuclear Society (2019). *Ontario Electricity Generation*. Retrieved from:
<https://cns-snc.ca/media/ontarioelectricity/ontarioelectricity.html>

- [10] E. Romero-Cadaval, G. Spagnuolo, L. G. Franquelo, C. A. Ramos-Paja, T. Suntio and W. M. Xiao, "Grid-Connected Photovoltaic Generation Plants: Components and Operation," in *IEEE Industrial Electronics Magazine*, vol. 7, no. 3, pp. 6-20, Sept. 2013.
- [11] L. Huber and M. M. Jovanovic, "A design approach for server power supplies for networking," in *Proc. of the 2000 IEEE Applied Power Electronics Conference and Exposition (APEC)*, vol. 2, pp. 1163-1169.
- [12] M. Adly and K. Strunz, "Irradiance-Adaptive PV Module Integrated Converter for High Efficiency and Power Quality in Standalone and DC Microgrid Applications," in *IEEE Transactions on Industrial Electronics*, vol. 65, no. 1, pp. 436-446, Jan. 2018.
- [13] L. Zhang, K. Sun, Y. Xing, L. Feng, and H. Ge, "A modular grid-connected photovoltaic generation system based on DC bus," in *IEEE Transactions on Power Electronics*, vol. 26, no. 2, pp. 523-531, 2011.
- [14] W. Li and X. He, "An Interleaved Winding-Coupled Boost Converter With Passive Lossless Clamp Circuits," in *IEEE Transactions on Power Electronics*, vol. 22, no. 4, pp. 1499-1507, July 2007.
- [15] HK-PolyU "Zero Current Switching Quasi-Resonant Converters"
ftp://ftp.ee.polyu.edu.hk/echeng/Power_Elect_EE4211/ZCS_Note.pdf
- [16] Texas Instrument (2016). "Fundamental of On-Resistance min Load Switches"
<http://www.ti.com/lit/an/slva771/slva771.pdf>
- [17] N. Mohan, *Power Electronics: Converters, Applications, and Design*. Wiley, 1989
- [18] R. L. Steigerwald, "A comparison of half-bridge resonant converter topologies," in *IEEE Transactions on Power Electronics*, vol. 3, no. 2, pp. 174-182, April 1988.

- [18] P. K. Jain, A. St-Martin and G. Edwards, "Asymmetrical pulse-width-modulated resonant DC/DC converter topologies," in *IEEE Transactions on Power Electronics*, vol. 11, no. 3, pp. 413-422, May 1996.
- [19] D. J. Tschirhart and P. K. Jain, "A CLL Resonant Asymmetrical Pulsewidth-Modulated Converter With Improved Efficiency," in *IEEE Transactions on Industrial Electronics*, vol. 55, no. 1, pp. 114-122, Jan. 2008.
- [20] N. C. D. Pont, D. G. Bandeira, T. B. Lazzarin and I. Barbi, "A ZVS APWM Half-Bridge Parallel Resonant DC–DC Converter With Capacitive Output," in *IEEE Transactions on Industrial Electronics*, vol. 66, no. 7, pp. 5231-5241, July 2019.
- [21] W. Li, Y. Zhao, Y. Deng and X. He, "Interleaved Converter With Voltage Multiplier Cell for High Step-Up and High-Efficiency Conversion," in *IEEE Transactions on Power Electronics*, vol. 25, no. 9, pp. 2397-2408, April 2010.
- [22] K. I. Hwu and Y. T. Yau, "An Interleaved AC–DC Converter Based on Current Tracking," in *IEEE Transactions on Industrial Electronics*, vol. 56, no. 5, pp. 1456-1463, May 2009.
- [23] G. Franceschini, E. Lorenzani, M. Cavatorta and A. Bellini, "3boost: A High-Power Three-Phase Step-Up Full-Bridge Converter for Automotive Applications," in *IEEE Transactions on Industrial Electronics*, vol. 55, no. 1, pp. 173-183, Jan. 2008.
- [24] P. W. Lee, Y. S. Lee, D. K. Cheng, and X. C. Liu, "Steady-state analysis of an interleaved boost converter with coupled inductors," in *IEEE Transactions on Industrial Electronics*, vol. 47, no. 4, pp. 787–795, Aug. 2000.
- [25] X. Huang, X. Wang, T. Nergaard, J. S. Lai, X. Xu, and L. Zhu, "Parasitic ringing and design issues of digitally controlled high power interleaved boost converters," in *IEEE Transactions on Industrial Electronics*, vol. 19, no. 5, pp. 1341– 1352, Sep. 2004.

- [26] G. Spiazzi and S. Buso, "Analysis of the Interleaved Isolated Boost Converter With Coupled Inductors," in *IEEE Transactions on Industrial Electronics*, vol. 62, no. 7, pp. 4481-4491, October 2014
- [27] Bor-Ren Lin and Hsin-Hung Lu, "Single-phase three-level PWM rectifier," Proceedings of the IEEE 1999 International Conference on Power Electronics and Drive Systems. PEDS'99 (Cat. No.99TH8475), Hong Kong, 1999, pp. 63-68 vol.1.
- [28] M. T. Zhang, Yimin Jiang, F. C. Lee and M. M. Jovanovic, "Single-phase three-level boost power factor correction converter," Proceedings of 1995 IEEE Applied Power Electronics Conference and Exposition - APEC'95, Dallas, TX, USA, 1995, pp. 434-439 vol.1.
- [29] L. Huber and M. M. Jovanovic, "A design approach for server power supplies for networking applications," APEC 2000. Fifteenth Annual IEEE Applied Power Electronics Conference and Exposition (Cat. No.00CH37058), New Orleans, LA, USA, 2000, pp. 1163-1169 vol.2.
- [30] B. R. Lin and J. J. Chen, "Analysis and implementation of a soft switching converter with high-voltage conversion ratio," in *IET Power Electronics*, vol. 1, no. 3, pp. 386-394, September 2008.
- [31] S. -. Tseng, S. -. Tseng and J. G. Huang, "High step-up converter with partial energy processing for livestock stunning applications," Twenty-First Annual IEEE Applied Power Electronics Conference and Exposition, 2006. APEC '06., Dallas, TX, 2006, pp. 7 pp.-.
- [32] S. -. Tseng, S. -. Tseng and J. -. Shiang, "High Step-up Converter Associated with Soft-Switching Circuit with Partial Energy Processing for Livestock Stunning Applications," 2006 CES/IEEE 5th International Power Electronics and Motion Control Conference, Shanghai, 2006, pp. 1-5.

- [33] K. C. Tseng and T. J. Liang, "Novel high-efficiency step-up converter," in *IEE Proceedings - Electric Power Applications*, vol. 151, no. 2, pp. 182-190, 9 March 2004.
- [34] T. J. Liang and K. C. Tseng, "Analysis of integrated boost-flyback step-up converter," in *IEE Proceedings - Electric Power Applications*, vol. 152, no. 2, pp. 217-225, 4 March 2005.
- [35] B. Axelrod, Y. Berkovich and A. Ioinovici, "Transformerless DC-DC converters with a very high DC line-to-load voltage ratio," *Proceedings of the 2003 International Symposium on Circuits and Systems, 2003. ISCAS '03.*, Bangkok, 2003, pp. III-III.
- [36] E. H. Ismail, M. A. Al-Saffar and A. J. Sabzali, "High Conversion Ratio DC-DC Converters With Reduced Switch Stress," in *IEEE Transactions on Circuits and Systems I: Regular Papers*, vol. 55, no. 7, pp. 2139-2151, Aug. 2008.
- [37] Y. Jang and M. M. Jovanovic, "New two-inductor boost converter with auxiliary transformer," in *IEEE Transactions on Power Electronics*, vol. 19, no. 1, pp. 169-175, Jan. 2004.
- [38] H. Gui, Y. Zhang, Z. Zhang and Y. Liu, "An optimized efficiency-based control strategy for islanded paralleled PV micro-converters," *2015 IEEE Applied Power Electronics Conference and Exposition (APEC)*, Charlotte, NC, 2015, pp. 229-234.
- [39] S. Jain, B. S. Satish and J. J. Lai, "High gain resonant boost converter for PV micro-converter system," *2016 IEEE Energy Conversion Congress and Exposition (ECCE)*, Milwaukee, WI, 2016, pp. 1-6.
- [40] H. Gui, Z. Zhang, X. He and Y. Liu, "A high voltage-gain LLC micro-converter with high efficiency in wide input range for PV applications," *2014 IEEE Applied Power Electronics Conference and Exposition - APEC 2014*, Fort Worth, TX, 2014, pp. 637-642.

- [41] Y. Shen, H. Wang, Z. Shen, Y. Yang and F. Blaabjerg, "A 1-MHz Series Resonant DC–DC Converter with a Dual-Mode Rectifier for PV Microinverters," in *IEEE Transactions on Power Electronics*, vol. 34, no. 7, pp. 6544-6564, July 2019.
- [42] D. Sera, L. Mathe, T. Kerekes, S. V. Spataru and R. Teodorescu, "On the Perturb-and-Observe and Incremental Conductance MPPT Methods for PV Systems," in *IEEE Journal of Photovoltaics*, vol. 3, no. 3, pp. 1070-1078, July 2013.
- [43] N. Femia, G. Petrone, G. Spagnuolo and M. Vitelli, "Optimization of perturb and observe maximum power point tracking method," in *IEEE Transactions on Power Electronics*, vol. 20, no. 4, pp. 963-973, July 2005.
- [44] A. K. Abdelsalam, A. M. Massoud, S. Ahmed and P. N. Enjeti, "High-Performance Adaptive Perturb and Observe MPPT Technique for Photovoltaic-Based Microgrids," in *IEEE Transactions on Power Electronics*, vol. 26, no. 4, pp. 1010-1021, April 2011.
- [45] M. A. Elgendy, B. Zahawi and D. J. Atkinson, "Assessment of Perturb and Observe MPPT Algorithm Implementation Techniques for PV Pumping Applications," in *IEEE Transactions on Sustainable Energy*, vol. 3, no. 1, pp. 21-33, Jan. 2012.
- [46] N. Femia, D. Granozio, G. Petrone, G. Spagnuolo and M. Vitelli, "Predictive & Adaptive MPPT Perturb and Observe Method," in *IEEE Transactions on Aerospace and Electronic Systems*, vol. 43, no. 3, pp. 934-950, July 2007.
- [47] K. L. Lian, J. H. Jhang and I. S. Tian, "A Maximum Power Point Tracking Method Based on Perturb-and-Observe Combined With Particle Swarm Optimization," in *IEEE Journal of Photovoltaics*, vol. 4, no. 2, pp. 626-633, March 2014.

- [48] M. A. G. de Brito, L. Galotto, L. P. Sampaio, G. d. A. e Melo and C. A. Canesin, "Evaluation of the Main MPPT Techniques for Photovoltaic Applications," in *IEEE Transactions on Industrial Electronics*, vol. 60, no. 3, pp. 1156-1167, March 2013
- [49] S. S. Satapathy and N. Kumar, "Modulated Perturb and Observe Maximum Power Point Tracking Algorithm for Solar PV Energy Conversion System," 2019 3rd International Conference on Recent Developments in Control, Automation & Power Engineering (RDCAPE), NOIDA, India, 2019, pp. 345-350.
- [50] A. Mohapatra, B. Nayak and C. Saiprakash, "Adaptive Perturb & Observe MPPT for PV System with Experimental Validation," 2019 IEEE International Conference on Sustainable Energy Technologies and Systems (ICSETS), Bhubaneswar, India, 2019, pp. 257-261.
- [51] G. A. Raiker, L. Umanand and B. Subba Reddy, "Perturb and Observe with Momentum Term applied to Current Referenced Boost Converter for PV Interface," 2018 IEEE International Conference on Power Electronics, Drives and Energy Systems (PEDES), Chennai, India, 2018, pp. 1-6.
- [52] K. Sundareswaran, V. V. Kumar, S. P. Simon and P. S. R. Nayak, "Cascaded simulated annealing/perturb and observe method for MPPT in PV systems," 2016 IEEE International Conference on Power Electronics, Drives and Energy Systems (PEDES), Trivandrum, 2016, pp. 1-5.
- [53] T. Eswam and P. L. Chapman, "Comparison of Photovoltaic Array Maximum Power Point Tracking Techniques," in *IEEE Transactions on Energy Conversion*, vol. 22, no. 2, June 2007, pp. 439-449.
- [54] Suwannatrai, P.; Liutanakul, P.; Wipasuramonton, P., "Maximum power point tracking by incremental conductance method for photovoltaic systems with phase shifted full-bridge dc-dc

converter," Electrical Engineering/Electronics, Computer, Telecommunications and Information Technology (ECTI-CON), 2011 8th International Conference on , vol., no., pp.637,640, 17-19 May 2011

[55] S. K. Ji, H. Y. Kim, S. S. Hong, Y. W. Kim and S. K. Han, "Non-oscillation Maximum Power Point Tracking algorithm for Photovoltaic applications," in Proc. of the 2014 Power Electronics and ECCE Asia (ICPE & ECCE), Jeju, pp. 380-385.

[56] G. Hsieh, S. Chen and C. Tsai, "Interleaved smart burp PV charger for lead acid batteries with incremental conductance MPPT," 2011 IEEE Energy Conversion Congress and Exposition, Phoenix, AZ, 2011, pp. 3248-3255.

[57] M. H. Anowar and P. Roy, "A Modified Incremental Conductance Based Photovoltaic MPPT Charge Controller," 2019 International Conference on Electrical, Computer and Communication Engineering (ECCE), Cox'sBazar, Bangladesh, 2019, pp. 1-5.

[58] Z. Xuesong, S. Daichun, M. Youjie and C. Deshu, "The simulation and design for MPPT of PV system Based on Incremental Conductance Method," 2010 WASE International Conference on Information Engineering, Beidaihe, Hebei, 2010, pp. 314-317.

[59] E. M. Ahmed and M. Shoyama, "Stability study of variable step size incremental conductance/impedance MPPT for PV systems," 8th International Conference on Power Electronics - ECCE Asia, Jeju, 2011, pp. 386-392.

[60] H. Mahamudul, M. Islam, A. Shameem, J. Rana and H. Metselaar, "Modelling of PV module with incremental conductance MPPT controlled buck-boost converter," 2013 2nd International Conference on Advances in Electrical Engineering (ICAEE), Dhaka, 2013, pp. 197-202.

- [61] T. Nahak and Y. Pal, "Comparison between conventional, and advance maximum power point tracking techniques for photovoltaic power system," 2016 IEEE 7th Power India International Conference (PIICON), Bikaner, 2016, pp. 1-5.
- [62] W. Xiao, A. Elnosh, V. Khadkikar and H. Zeineldin, "Overview of maximum power point tracking technologies for photovoltaic power systems," in Proc. of the 2011 Annual Conference on IEEE Industrial Electronics Society, Melbourne, VIC, pp. 3900-3905.
- [63] S. Khadidja, M. Mountassar and B. M'hamed, "Comparative study of incremental conductance and perturb & observe MPPT methods for photovoltaic system," 2017 International Conference on Green Energy Conversion Systems (GECS), Hammamet, 2017, pp. 1-6.
- [64] A. Gupta, P. Kumar, R. K. Pachauri and Y. K. Chauhan, "Performance analysis of neural network and fuzzy logic based MPPT techniques for solar PV systems," 2014 6th IEEE Power India International Conference (PIICON), Delhi, 2014, pp. 1-6.
- [65] R. S. Sreelekshmi, A. Ashok and M. G. Nair, "A fuzzy logic controller for energy management in a PV — battery based microgrid system," 2017 International Conference on Technological Advancements in Power and Energy (TAP Energy), Kollam, 2017, pp. 1-6.
- [66] S. Miqoi, A. E. Ougli, B. Tidhaf and A. Rabhi, "Application of fuzzy logic on a PV water pumping system," 3rd International Symposium on Environmental Friendly Energies and Applications (EFEA), St. Ouen, 2014, pp. 1-6.
- [67] Y. Y. Ghadi, M. G. Rasul, and M. M. K. Khan, "Design and development of advanced fuzzy logic controllers in smart buildings for institutional buildings in subtropical Queensland," *Renew. Sustain. Energy Rev.*, vol. 54, pp. 738–744, Feb. 2016

- [68] M. A. Hannan, Z. A. Ghani, A. Mohamed, and M. N. Uddin, "Real-time testing of a fuzzy-logic-controller-based grid-connected photovoltaic inverter system," in *IEEE Transactions on Industry Applications.*, vol. 51, no. 6, pp. 4775–4784, Nov./Dec. 2015
- [69] S. K. Saha and Jaipal, "Optimization Technique Based Fuzzy Logic Controller for MPPT of Solar PV System," 2018 International Conference on Emerging Trends and Innovations In Engineering And Technological Research (ICETIETR), Ernakulam, 2018, pp. 1-5
- [70] K. H. Kapumpa and D. Chouhan, "A fuzzy logic based MPPT for 1MW standalone solar power plant," 2017 Recent Developments in Control, Automation & Power Engineering (RDCAPE), Noida, 2017, pp. 153-159.
- [71] D. Reddy and S. Ramasamy, "A fuzzy logic MPPT controller based three phase grid-tied solar PV system with improved CPI voltage," 2017 Innovations in Power and Advanced Computing Technologies (i-PACT), Vellore, 2017, pp. 1-6.
- [72] R. Sankar, S. Velladurai, R. Rajarajan and J. A. Thulasi, "II. PV system description: Maximum power extraction in PV system using fuzzy logic and dual MPPT control," 2017 International Conference on Energy, Communication, Data Analytics and Soft Computing (ICECDS), Chennai, 2017, pp. 3764-3769.
- [73] Panasonic (2019). "Aluminim Electrolytic Capacitors (Surface Mount Type)" <https://industrial.panasonic.com/cdbs/www-data/pdf/RDE0000/ABA0000C1187.pdf>
- [74] Nichicon (2015) "Aluminum electrolytic capacitors" <https://www.nichicon.co.jp/english/products/pdfs/e-uvz.pdf>
- [75] Panasonic (2019). "Aluminim Electrolytic Capacitors" <https://industrial.panasonic.com/cdbs/www-data/pdf/RDE0000/ABA0000C1202.pdf>

- [76] TDK Electronics (2018). "Metallized Polyester Film Capacitors" https://www.tdk-electronics.tdk.com/inf/20/20/db/fc_2009/B32520_529.pdf
- [77] KEMET (2020). "General Purpose Metallized Polyester Film Capacitors" https://content.kemet.com/datasheets/KEM_F3103_R60.pdf
- [78] Panasonic (2017). "Metallized Polyester Film Capacitor" <https://industrial.panasonic.com/cdbs/ww-data/pdf/RDI0000/ABD0000C179.pdf>
- [79] E. Koutroulis and K. Kalaitzakis, "Design of a maximum power tracking system for wind-energy-conversion applications," in *IEEE Transactions on Industrial Electronics*, vol. 53, no. 2, pp. 486-494, April 2006.
- [80] Simmi Mangat, Mei Qiu and P. Jain, "A modified asymmetrical pulse-width-Modulated resonant DC/DC converter topology," in *IEEE Transactions on Power Electronics*, vol. 19, no. 1, pp. 104-111, Jan. 2004.
- [81] B. Hauke, "Basic Calculation of a Boost Converter's Power Stage", July 2010.

APPENDIX

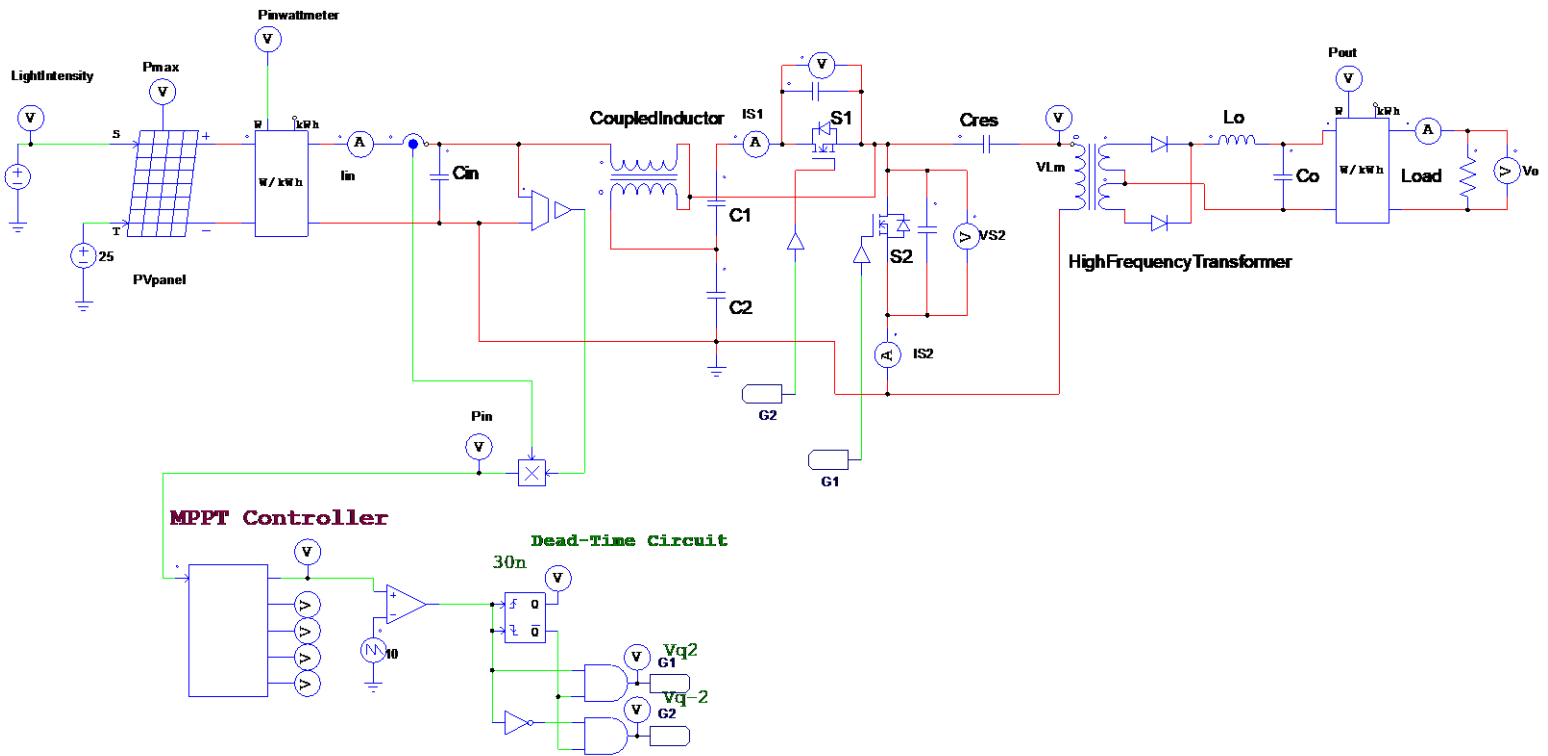


Fig. A-1: PSIM schematic

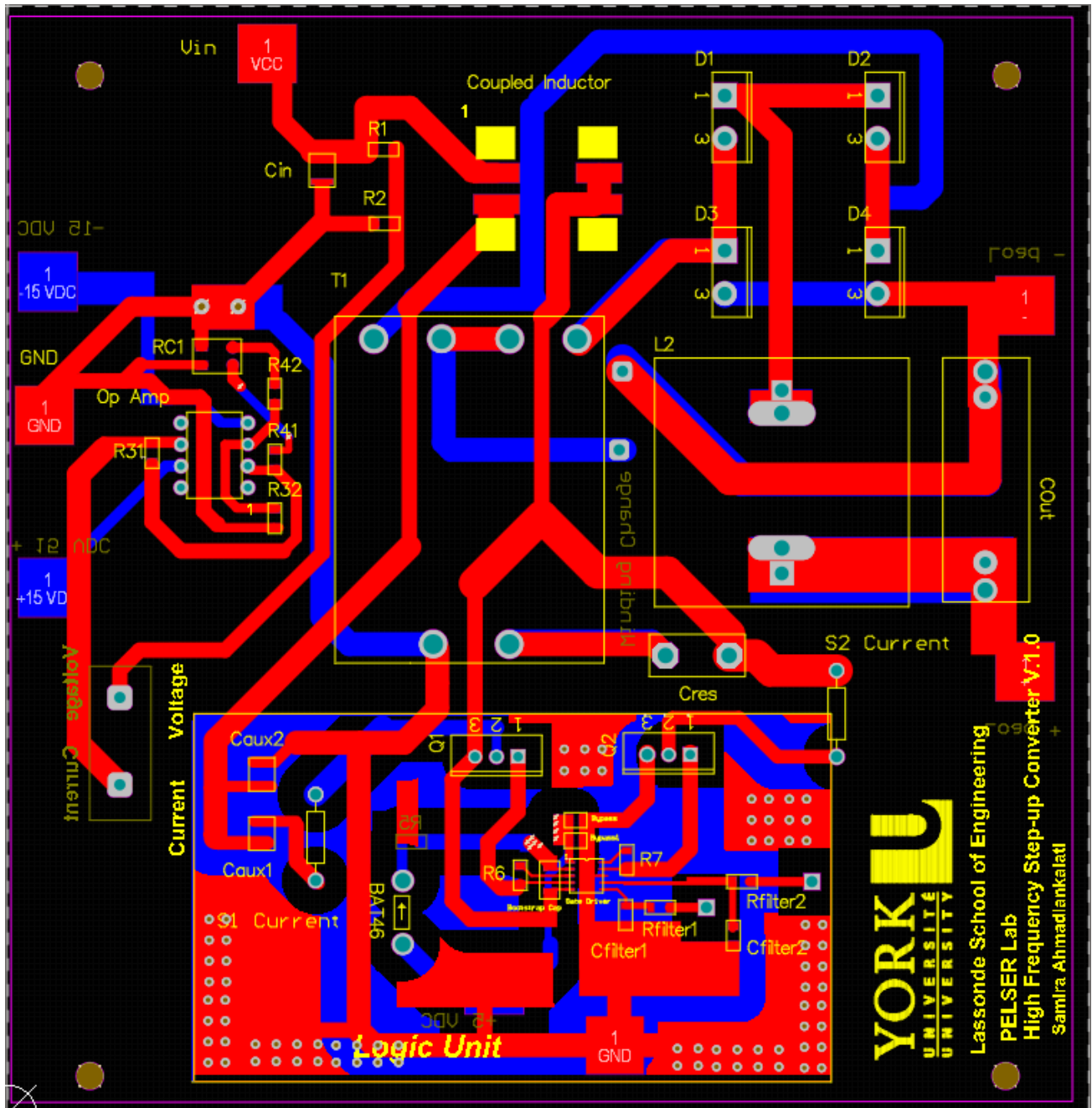


Fig. A-3: ALTIUM PCB Layout

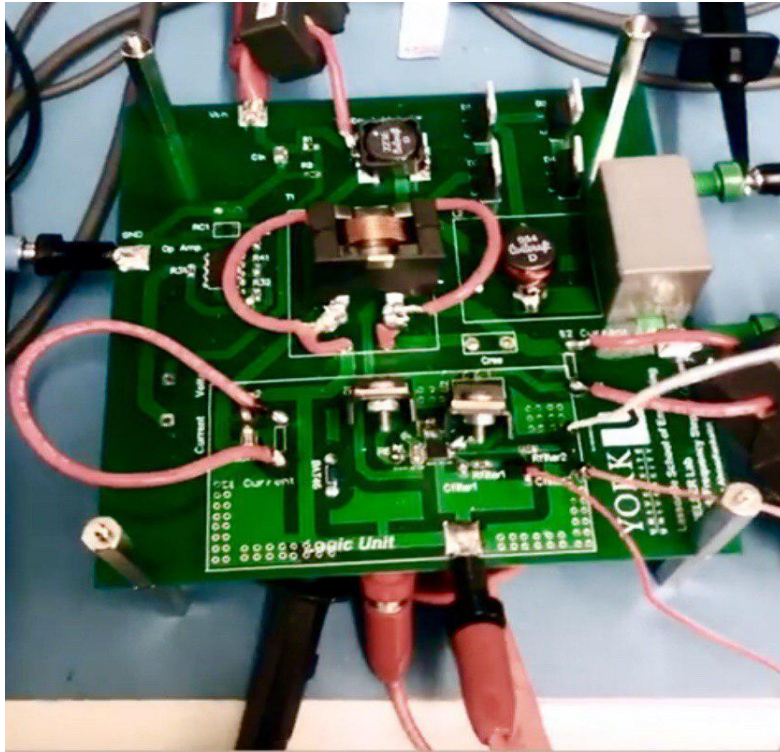


Fig. A-5: Proof of concept hardware prototype

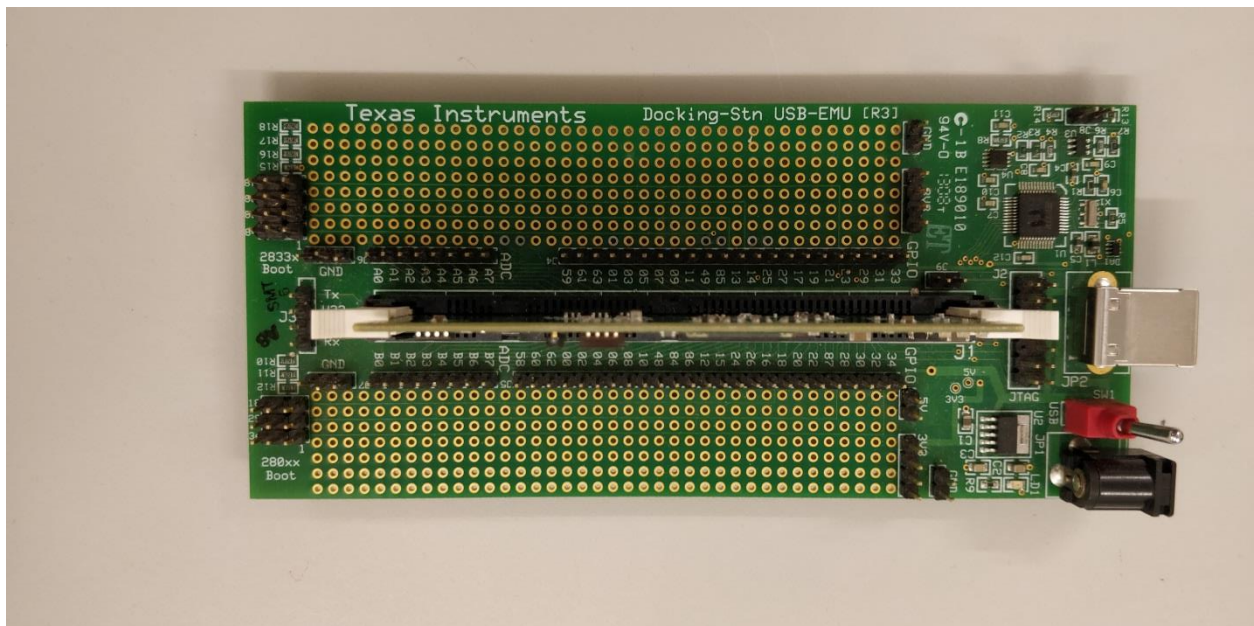


Fig. A-6: Digital Signal Evaluation board TMS320 F28335

MPPT Code

```
{

// PLACE GLOBAL VARIABLES OR USER FUNCTIONS HERE...

double DE; // Initial duty cycle value
double dp; // change in power
double p;
double counter;
double dD1; // previous step duty cycle change
double oldp; // previous step power point
double dD2; // next step duty cycle change

{
if (counter >= 600000)
{
p = in[0]; // Read in the input power of the converter
dp= p- oldp;// Calculate the change in input power

if ( dp >0.5 && dD1 > 0 )
{
dD2= (0.027)*dp;// Keep increasing duty cycle to achieve optimal power point
out[0]= DE+ dD2; // Next step duty cycle value
dD1= dD2;// Update previous step duty cycle
out[4]=1;// Loop indicator
}
else if ( dp >0.5 && dD1 <0 )
{
dD2 = (-0.04) * dp;// Decrease duty cycle value
out[0]= DE+ dD2;
dD1= dD2;
out [4]=2;
}
else if (dp <-0.5 && dD1 >0)
{
dD2= (0.04) * dp;
out[0]= DE+ dD2;
dD1= dD2;
out[4]=3;
}
else if (dp <-0.5 && dD1 <0)
{
dD2= (-0.027) * dp;
out[0]= DE+ dD2;
```

```

dD1= dD2;
out[4]=4;
}
else if(-0.5<=dp && dp<=0.5 )
{
out[0]= DE;
out[4]=5;
}
DE= out [0];
counter=1;
}

else if (counter==1)
{
oldp=in[0];
out[0]=DE;
DE=out[0];
counter=counter+1;

}

else if (counter>=1 || counter <600000)
{
out[0]=DE;
DE=out[0];
counter=counter+1;
}
out[1]=counter;
out[2]= dD1;
out[3]= dp;
}
{
//INITIALIZATION CODE
DE =5;
dD1=0.2;
counter=1;// Reset counter

}

```